Design of Gas Diffusion Electrode Fuel Cell Type Electrochemical Device for CO_2 Reduction

by

Yucheng Wang

A thesis submitted for the degree of

Doctor of Philosophy

Faculty of Engineering and Environment

Northumbria University, UK

November 2020

Abstract

Using the electrochemical catalytic method, CO_2 reduction reaction (CO_2RR) has become practicable process with a low energy consumption. The products generated from the CO_2RR are normally low carbon containing compounds, which can be directly used as fuels or feedstock for chemical industry. This is considered as a clean and sustainable cycle. However, low activity, poor selectivity and durability of electrocatalysts, limitation of CO_2 mass transfer, and competing hydrogen evolution reaction (HER) in the aqueous media cause significantly reduced Faradaic efficiency (FE) towards electrochemical reduction reaction (eCO_2RR). To make such technology become industrially viable, suppression of HER, good selectivity and high reaction efficiency towards desired products are under high demands.

The main achievement of this work is about the cells design for eCO_2RR. Here we researched on novel, high performance and low-cost catalysts, in order to enhance the selectivity and activity of targeted products. We conducted the reactor renovation, and made a new electrochemical cell design, which was adopted advanced gas diffusion electrode (GDE) technology using carbon paper. These have enhanced the CO_2 mass transfer therefore increased the FE values. We also developed a new strategy of using a porous Bi-layer GDE, and achieved dramatically increased reaction efficiency, enhanced selectivity and system durability. Several advanced nano-structured catalysts have been involved for eCO_2RR, including Cu_2O nano-cube, Graphene supported Cu oxides, indium metal–organic framework, commercial antinomy tin oxide and indium tin oxide. CO production using the synthesized Cu_2O catalyst reached an FE value of 84.20% and a current density of 83.4 $mA \bullet cm^{-2}$ at -0.8 V vs. reversible hydrogen electrode (RHE). Formate production using ATO catalyst reached an FE value of 84.54% and a current density of 97.2 $mA \bullet cm^{-2}$ at -1.2 V vs. RHE. These new catalysts, processes and strategies has contributed significantly on future development of eCO_2RR.

Acknowledgement

First of all, I would like to express my sincere gratitude to my supervisors, Dr Terence Liu and Prof. Richard Fu, for their consistent support, guidance and encouragement at every stage of the research project. I would like to thank them for constructive criticism of the paper manuscripts, reports and thesis. Throughout my PhD study, I have met so many challenges and difficulties, and they are the persons who can help me to solve those problems.

Secondly, I would like to thank Northumbria University and the Engineering and Physical Science Research Council for the financial supports. I gratefully acknowledge all physical and mechanical technicians for technical help: especially Dr Pietro Maiello for helping me with SEM and XRD operation; Mr Adam Cosheril for the 3D printing and laser cutting of my designed cells; and Mr Simon Neville for his help in mechanical lab.

Thirdly, I would like to express my gratitude and appreciation for Prof. Ben Bin Xu. He organized group meetings every Friday, where I could have the opportunities to do the oral presentation and discuss about the literature and project progress. I always obtain useful feedback from his insightful comments and suggestions. Meanwhile, he is very professional on research methodology and paper writing, where I have learnt a lot from him.

Fourthly, I am deeply grateful to Prof. Eileen Yu and Ms Hang Xiang from Newcastle University for bringing me the GDE concept for eCO_2RR and helping the operation of gas chromatography and ion chromatography. They gave me many academic supports and valuable inputs in my PhD study.

At last, I would like to extend my sincere thanks to my friends in Newcastle for academic help. I would like to thank Mr Ansu Sun for helping me in 3D printing of my cells; Mr Hanhui Lei for simulation of my designed cells; Ms Yanan Wu for the assistance of electrochemical test; Dr Da Li, Dr Ding Wang, Dr Cong Wang and Mr Sreepathy Sridhar for their academic help.

The first few days I came to this unfamiliar city, Newcastle, I feel helpless and lonely, I was doubt if I could finish my PhD study at that time. Now I feel grateful that I have got so many adorable friends in Newcastle, who give me the courage and strength to overcome the difficulties, hurdles and make me unbreakable.

In the end, I am deeply grateful to my parents, although the distance between you and me is more than 9000 km, you always give me spiritual encouragement and support.

Table of Contents

List of Figures

List of Tables

List of Publications and Conferences

Publications:

A High-Performance Direct Methanol Fuel Cell Technology Enabled by Mediating High-Concentration Methanol through Graphene Aerogel
X. Liu, J. Xi, BB. Xu, B. Fang, Y. Wang, M. Bayati, K. Scott, C. Gao, 16 Oct 2018, In: Small Methods. 2, 10, 1800138.

Half-Sphere Shell Supported Pt Catalyst for Electrochemical Methanol Oxidation
B. Ren, J. Lu, Y. Wang, X. Gu, BB. Xu, Y. Fu, K. Luo, M. Bayati, TX. Liu, 6 May 2020, In: Journal of The Electrochemical Society, Volume 167, Number 8.

Nickel Oxide Immobilized on the Carbonized Eggshell Membrane for Electrochemical Detection of Urea
S. Lu, Z. Gu, M. Hummel, Y. Zhou, K. Wang, BB. Xu, Y. Wang, Y. Li, X. Qi, TX. Liu, 22 June 2020, In: Journal of The Electrochemical Society, Volume 167, Number 10.

A Ga-Sn Liquid Metal Mediated Structural Cathode for Li-O_2 Batteries
Z. Luo, C. Ji, L. Guo, G. Zhu, B. Xu, Y. Wang, X. Liu, K. Luo. Materials Today Energy, 2020.

Guided Gas Diffusion on the Catalyst Bed for Enhanced CO_2 Electrochemical Reduction
Y. Wang, H. Lei, H. Xiang, BB. Xu, Y. Fu, C. Xu, G. Hinds, EH. Yu, TX. Liu, 2020 (In preparation)

Oral and Poster Presentations:

CuO/Graphene Nano-Flower Catalyst for CO_2 Electro-chemical Reaction (poster)
Y. Wang, R. Fu, TX. Liu, The Engineering & Environment PGR Conference 2018, Newcastle upon Tyne, 21 June 2018.

Catalysts and Electrochemical Device for CO_2 Reduction (poster)
Y. Wang, X. Liu, Y. Fu, 2019 Scotland and North of England Electrochemistry Symposium (Butler Meeting), Edinburgh, 9 April 2019.

Catalysts and Electrochemical Device for CO_2 Reduction (poster)
Y. Wang, H. Xiang, EH. Yu, Y. Fu, X. Liu, SCI Electrochemistry Postgraduate Conference 2019, Newcastle upon Tyne, 31 May 2019.

Cu-based Catalysts of Electrochemical Reduction using Graphene aerogel Gas Diffusion Electrode Type Device (poster)
Y. Wang, H. Xiang, EH. Yu, Y. Fu, X. Liu, SCI Electrochemistry Postgraduate Conference 2019, Newcastle upon Tyne, 31 May 2019.

Cu-based Catalysts for Electrochemical Reduction of CO_2 using Graphene aerogel Gas Diffusion Electrode Type Device (poster)
Y. Wang, H. Xiang, E. Yu, Y. Fu, TX. Liu. Electrochem 2019, Glasgow, 26 - 28 August 2019.

Mass Transfer Effect to CO_2 Electrochemical Reduction Reaction through Different Das Diffusion Mechanism (oral & 3MT)
Y. Wang, T. Liu, H2FC Supergen Hydrogen Research Conference 2020, Nottingham, 17 - 18 February 2020.

Effect of Mass Transfer on Gas Diffusion Electrode Cell for Evaluation of CO_2 Electrochemical Reduction Reaction (oral-flash presentation, & poster**)**
Y. Wang, H. Xiang, H. Lei, EH. Yu, and TX. Liu, Reforming Multi-disciplinary Engineering Innovation for the New Normal, Online Webinar, 28 August 2020.

Mass Transfer Effect to CO_2 Electrochemical Reduction Reaction through Different Gas Diffusion Mechanism (best poster, **SCI poster presentation award**)
Y. Wang, H. Lei, H. Xiang, EH. Yu, TX, Liu, 27th CSCST SCI Annual Conference: Sustainable Energy and Manufacturing the Future, Online Webinar, 11 - 12 September 2020.

Symbols and Abbreviations

Symbols:

A	Peak area of GC
C	CO_2 concentration
C_O	Oxidised species expression
C_R	Reduced species expression
d	d-spacing
D_a	Molecular diffusion coefficient in air
E	Potential
E_{ARE}	Potential vs. RE-61AP reference electrode
E^0	Standard potential
$E_{Ag/AgCl}$	Potential vs. Ag/AgCl
E_c	Activation energy
$E_{eq,ref}(T)$	Reference equilibrium potential
E_i	Initial potential
E_{RHE}	Potential vs. reversible hydrogen electrode
E_s	Chosen potential
F	Faraday's constant
f	Correction factor
I	Current
$i_{0,ref}(T)$	Reference exchange current density
i_v	Coupled reaction from the porous electrode reaction
j	Current density
M	Surface metal active sites

$M_{\omega CO2}$	CO_2 molar mass
$M_{\omega HCOOH}$	HCOOH molar mass
n (X-ray)	Diffraction order
n (Faradic efficiency)	Molar mass of the product
P	Pressure
Q	Applied charge
R	Ideal gas constant, 8.314
t	Time
T	Kelvin temperature
u	Gas inlet velocity
V	Volume
v	Flow rate
v_j	Stoichiometric coefficient
x	Distance along the axis of flow
α	Number of transferred electrons per mole of reactant
Δm	Mass increase
θ	Incident angle
λ	Incident X-ray wavelength

Abbreviations:

4p-cell	4-part H-type cell
AM	Additive manufacturing
ARE	RE-61AP reference electrode
ATO	Antimony tin oxide
b-Cu_xO_y/Graphene	nano-bundles shaped Cu_xO_y/Graphene
BID	Barrier discharge ionization
CA	Chronoamperometry
CB	Conduction band
CCS	Carbon Capture and Storage
CCU	CO_2 capture and utilization
CE	Counter electrode
CEM	Cation exchange membrane
Comm. Cu_2O	Commercial Cu_2O powders
CP	Carbon paper
CP-cell	Carbon paper gas diffusion electrode cell
Cu_xO_y/graphene	Graphene supported Cu oxides
CV	Cyclic voltammetry
DEMS	Differential electrochemical mass spectrometry
DI	Deionized
DMF	Dimethylformamide
DMFC	Direct methanol fuel cell
DSA	Drop shape analysis
eCO_2RR	Electrochemical CO2 reduction reaction
EDS	Energy Dispersive Spectroscopy

EGR	Enhanced gas recovery
EGS	Enhanced geothermal systems
EOR	Enhanced oil recovery
FCC	Face centred cubic
f-Cu_xO_y/Graphene	Nano-flower shaped Cu_xO_y/Graphene
FE	Faradaic efficiency
FID	Flame ionization detector
GA	Graphene aerogel
GA-cell	Graphene aerogel gas diffusion electrode cell
GACP-cell	Hybrid graphene aerogel carbon paper gas diffusion electrode cell
GC	Gas chromatography
GDE	Gas diffusion electrode
GDL	Gas diffusion layer
H-cell	H-type cell
HER	Hydrogen evolution reaction
IC	Ion chromatography
IEM	Ion exchange membrane
In-MOF	Indium metal-organic framework
IPCC	Intergovernmental Panel on Climate Change
ITO	Indium tin oxide
LDH	Layered double hydroxide
m-Cu_xO_y/Graphene	Melted Cu_xO_y/Graphene
MEA	Membrane electrode assembly
MFC	Microfluidic flow cell

MOF	Metal-organic framework
n-Cu_xO_y/Graphene	Nano-needle shaped Cu_xO_y/Graphene
OP	Overpotential
PEM	Proton exchange membrane
PEM-cell	Polymer electrolyte membrane compact flow cells
PEMFC	Proton exchange membrane - fuel cell
PTFE	Polytetrafluoroethylene
RE	Reference electrode
RHE	Reversible hydrogen electrode
RWGS	Reversed water-gas shift reaction
SCD	Secondary current distribution
SCE	Saturated calomel electrode
SDS	Sodium dodecyl sulfate
SEM	Scanning electron microscope
SHE	Standard hydrogen electrode
SOEC	Solid oxide electrolyser cell
Syn. Cu_2O	Synthesized Cu_2O nano particles
TCD	Thermal conductivity detector
TOCS	Transfer of concentrated species
VB	Valence band
WE	Working electrode
XRD	X-ray diffraction
ZIF	Zinc imidazolate metal-organic framework

Chapter 1 Introduction

1.1 Background and Motivation

The increasing demand of energy has induced high consumption of fossil fuels and drastic increase in green gas emission. It has been reported that CO_2 emission has been increased from 118.93 million metric tons in 1840s to 36.57 billion metric tons in 2018[1]. It is believed that the combustion of fuels process combines carbon in fuel and oxygen in air, and then produce carbonaceous waste, released into the atmosphere. Carbon dioxide (CO_2) is now regarded as a key pollutant for the greenhouse problem[2]. It is undeniable that, modern civilization is established based on the cost of a large amount of non-renewable resources, which will cause environmental and energy issues for a long term. It is reported that, based on the current rate of energy consumption, the approximate lifetimes of the world's petroleum, natural gas, and coal reserves are 50 years, 52.8 years, and 153 years, respectively[3], therefore, the energy problem has always been the most prominent problem in the 21st century[4].

From the chemical industry aspect, the most promising solutions are to capture and reuse the CO_2 emission to produce value added energy carrier fuels. In ambient temperature, CO_2 has a stable triatomic molecule which consists of one carbon and two oxygen atoms. The carbon is bonded with oxygen by one σ and π bond, forming two C=O bonds with 116.3 pm bond length and 750 $kJ \cdot mol^{-1}$ bonding energy, which is higher than the bonding energies of C=C, C-O and C-H. Meanwhile, CO_2 molecule has asymmetric stretching and bending vibrational modes, which allow it to absorb and emit infrared radiation at wavelengths of 4.26 and 14.99 μm, and could capture the reflection energy from the earth[5]. Moreover, CO_2 can be dissolved into the ocean forming carbonic acids which cause ocean acidification, thus decreasing the pH value of sea water and affecting the life cycles of marine organisms and the subsequent food chains[6].

It is reported that the CO_2 emissions have been increased by 90% from 1970s to 2011 and the fossil fuel combustion and industrial activities contribute 78% of the emissions[7]. The data published from NASA reported that the concentration of CO_2 in atmosphere has been increased from 378.21 ppm in Jan. 2005 to 413.25 in Feb. 2020[8]. This has induced the global warming as a consequence, and led to the melting of glacier in polar regions and the rising of sea levels. Fig. 1.1 shows the global climate change, and it is obvious that the global average temperatures have been increased by about 1°C since the industrial revolution.[10]

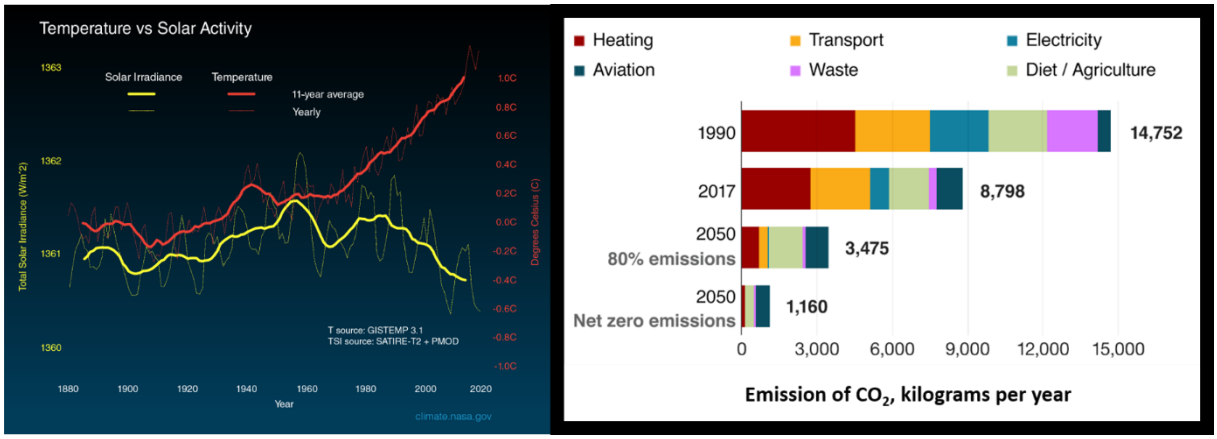

Figure 1.1 a) Global surface temperature changes (red line) and the Sun's energy that Earth receives (yellow line) in watts (units of energy) per square meter since 1880. The lighter/thinner lines show the yearly levels while the heavier/thicker lines show the 11-year average trends[9] b) Household emissions in UK in 1990, 2017 and 2050, Source: Climate Change Committee/BEIS, 2019[10]

Due to the severe situation, it has drawn much attention for the environmental problems, and more governments policies have been announced towards strict control of CO_2 emission. In 2015, the Paris Agreement was passed and announced to combat climate change and adapt to its effects, and its aim is to keep a global temperature rise below 2 °C above pre-industrial levels in this century [11]. Governments are taking actions for the targets, and UK government has announced that the greenhouse gas emissions in the UK will be cut down to almost zero by 2050[12].

In order to solve the energy crisis and greenhouse effect, research on CO_2 capture and utilization (CCU) has become a popular topic. Fig. 1.2 shows a circular economy which can be established to convert waste CO_2 into carbon source in replacement of fossil feedstock[13].

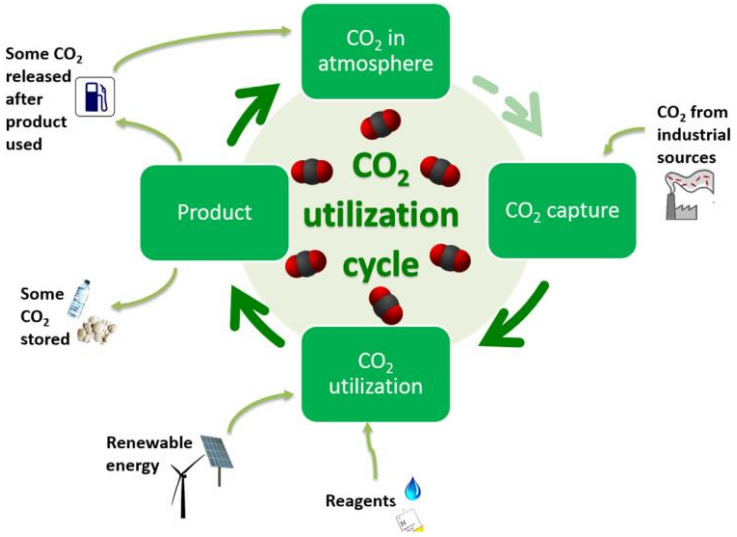

Figure 1.2 Schematic representation of a carbon dioxide capture and utilisation process[13]

During this cycle, CO_2 is separated and captured from industrial or household tail gases. Then the collected CO_2 will be partly used for CO_2 gas storage (for soft drink or fire extinguisher etc.), or converted to high value-added fuels of utilization primary energy from renewable energy resources[14] (e.g. solar, wind etc.). The CO_2 will be emitted to atmosphere after utilization and will be captured for CO_2 utilization cycle.

The most challenging step among this cycle is CO_2 utilisation for commercialization (e.g., to convert value added renewable products). While based on the development of science and technology, the bottleneck of CO_2 reduction such as energy efficiency, reaction activity will be overcome. In the flowing sections, we will discuss about the methods applied for CO_2 utilization so far.

1.2 CO_2 Capture, and Utilization Methods

1.2.1 CO_2 Capture

Several measures have been implemented to reduce the CO_2 concentration into atmosphere. An agreement held by Intergovernmental Panel on Climate Change (IPCC) in 2005 gives the definition of Carbon Capture and Storage (CCS), where CCS consists of three basic stages: separation of CO_2, transportation and storage[15].

Post-combustion is one of the key technology options for CO_2 capture[16]. It presents the advantages as the existing combustion methods can be used without radical changes[17]. Many separation methods could be employed with post-combustion capture methods. These include: a) Adsorption, which is a physical process that CO_2 was attached onto the adsorbents, such as activated carbon, alumina, metallic oxides and zeolites[18]; b) Physical absorption, which is basically the physical absorption of CO_2 into the solvent without chemical reaction, the typical solvents such as Selexol (dimethyl ethers of polyethylene glycol) and Rectisol (methanol)[19]; c) Chemical absorption, where the solvent reacts with CO_2 to from weakly bonded intermediates[17] (in which CO_2 can be regenerated with the help of heat); d) Cryogenics separation, which separates the CO_2 from flue mixture gases by condensation (CO_2 condenses at -56.6°C), normally under high CO_2 concentration circumstance due to the concern of cost[20]; e) Membrane absorption, where a membrane separates the flue gas and liquid solvent. The membrane may or may not provide an additional selectivity, and avoid the flooding, entrainment, channelling or foaming problem[21].

Transportation methods for CO_2 can be pipelines, marine tankers, road and rail tankers, and then the CO_2 can be either stored or directly converted to value added chemicals. Physical

storage strategies such as deep ocean sequestration[22] or geological storage[23] can transfer CO_2 from atmosphere to underground, which cannot resolve the problem permanently.

1.2.2 CO_2 Utilization

The treatment of CO_2 (Fig. 1.3) can be a physical isolation, such as deep ocean sequestration, geological storage and reduce the usage of CO_2, where these methods cannot fundamentally solve the problem. Another way is the utilization of CO_2, which is 'turning waste into treasure'. It can be classified into two categories including CO_2 direct usage (physical utilization) and CO_2 conversion[24]. For physical utilization, direct uses of CO_2 include soft drinks, fire extinguisher, dry ice and refrigerant etc., while these applications are limited in small scale and have little effects for CO_2 abatement[25]. In industries, CO_2 can be used to enhance the processes in enhanced oil recovery (EOR), enhanced gas recovery (EGR) and enhanced geothermal systems (EGS)[26]. Compared with the direct use, CO_2 conversion is regarded as a promising solution which can consume CO_2 while producing renewable fuels. Recently, CO_2 conversion can be realised using chemical methods[2, 14, 27], photocatalytic[28-32] and electrocatalytic approach[33].

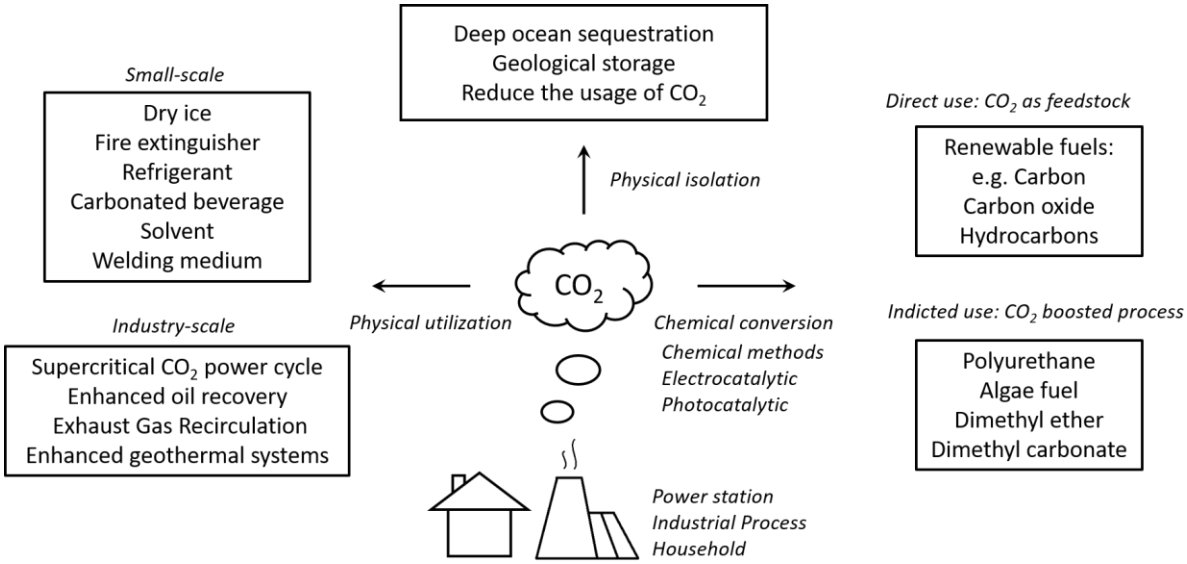

Figure 1.3 Three pathways of CO_2 treatment[2, 14, 26, 33]. Physical utilization, where CO_2 be directly used as resource of products. Physically isolation, where CO_2 is isolated geologically. Chemical conversion, where CO_2 is chemically converted to useful products.

- Chemical Method

Thermochemical CO_2 hydrogenation is one of the commonly used methods to produce carbon fuels. CO is primarily formed by reversed water-gas shift reaction[34] (RWGS), present in Eq. 1.1.

$$CO_2 + H_2 = CO + H_2O, \Delta H_{298K} = 41.2\ kJ/mol \qquad \text{Eq. 1.1}$$

Then the CO_2 can be further reduced into methanol (Eq. 1.2)

$$CO_2 + 3H_2 = CH_3OH + H_2O, \Delta H_{298K} = -49.5\ kJ/mol \qquad \text{Eq. 1.2}$$

From a thermodynamic aspect, Eq. 1.1 is endothermic, which requires both a high reaction temperature (500 -750 $^{\circ}$C) and a low pressure (0-5 bar), e.g., stringent reaction conditions[35].

The Eq. 1.2 is an exothermic reaction, in which more hydrogen gases are required for reactant, but this brings more challenges of this method. Due to the high energy consumption during

chemical reactions and the rapid degradation of the instruments, this reaction is not economically variable to be widely applied for industrial level applications.

Apart from the above methods, photocatalytic electrochemical reduction and electrochemical reduction of CO_2 are reported to be more efficient methods, which are discussed as below.

- Photocatalytic Reduction of CO_2

In nature, photosynthesis processes of plants can absorb and convert CO_2 into CO, CH_4 and other organic molecules to sustain the energy for life (Fig. 1.4a). A bionics concept of CO_2 photocatalytic reaction is believed to have the potential by utilization of solar energy, where it mimics the natural photosynthetic cycle in the agriculture plants[29, 31]. It can simply convert CO_2 into hydrocarbon fuels, according to the following process[28, 36] (Fig. 1.4b).

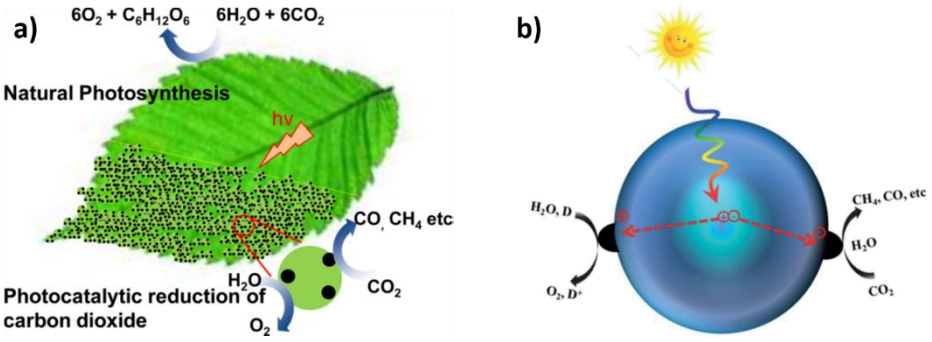

Figure 1.4 a) Photosynthesis of nature leaves[37] and b) schematic illustration of the photocatalytic of CO_2 reduction reaction

For semiconductor photocatalysts, their band structures determine their capabilities to absorb light, and also their redox reactions on the surface (Fig. 1.4b). Therefore, the research on band structure is regarded as a possible strategy to enhance the visible light activity of photocatalysts[36]. Typical photocatalysts can be classified into six groups, including:

- **Metal oxide**, which is the most common type of photocatalyst materials, consists of transition metal cations (e.g. TiO_2[38], ZrO_2[39])
- **Metal sulphide** (e.g. CdS[40], ZnS[41])
- **Metal nitride** (e.g. Ta_3N_5[42], GaN[43])
- **Layered double hydroxide (LDH)**, where the general formula is $[M^{2+}_{1-x}M^{3+}_{x}(OH)_2][An^{-}_{x/n}\cdot mH_2O]$ (M^{2+}, M^{3+}, and An^{-} are divalent cation, trivalent cation, and interlayer anion, respectively). It is layered materials with positively charged metal hydroxide layers and balanced-charged anions between each layer[36]. (e.g. Ti-based LDHs[44-46])
- **Metal-organic framework (MOF)**, MOFs emerge as novel materials which have high porosity and their single-metal site dispersion with open structures consists of metal ions or clusters coordinated with organic ligands[47]. (e.g. MIL-125-NH_2[48])
- **Metal-free material** (e.g. graphitic carbon nitride g-C_3N_4[49])

The mechanism of photocatalytic reduction of CO_2 is that the electrons are excited from the valence band (VB, the highest energy band occupied by electrons[30]) to the conduction band (CB, the lowest energy band with no electron at the ground state[30]) by absorbing photons which contain higher energy than the semiconductor's band gap. The same number of holes are generated in the CB simultaneously. Then the electron–hole pairs are separated and transported to trigger the surface catalytic redox reaction. In the photocatalytic CO_2 reduction system, both CO_2 photo-reduction and water (or sacrificial agent) photo-oxidation happens simultaneously, thus reducing CO_2 into CO, CH_3OH and CH_4[28, 30]. However, the low conversion rate and efficiency are far from industrial applications. For the photocatalytic designing strategies, the research is focused on enhancing the visible light activity of photocatalysts as mentions previously, using strategies such as cation doping[50], anion doping[51], nano-structural design[52] and heterostructure design[53], to obtain lower CB and higher VB.

- Electrocatalytic reduction of CO_2

Electrocatalytic reduction of CO_2 is regarded as the most promising CO_2 utilization method because of its mild reaction conditions and the desired products can be easily obtained from controlling the reaction conditions, e.g. CO, CH_4, C_2H_4, HCOOH[54]. It can be realized in a simple fuel cell type device which is called CO_2-electrolyzer[54, 55], and the electricity applied for the eCO_2RR can be generated from renewable sources such as wind or solar[56, 57]. For the basic electrochemical reaction, CO_2 is reduced on cathode, and the only consumption is water. The eCO_2RR on cathode has the chemical reaction as follows:

$$CO_2 + xe^- + xH^+ \rightarrow CO, HCOOH, CH_4 \qquad \text{Eq. 1.3}$$

where CO_2 can be reduced through two, four, six and eight electrons' transfer to carbon monoxide (CO), formate or formic acid ($HCOO^-$, HCOOH), methane (CH_4), methanol (CH_3OH), ethylene (CH_2CH_2), ethanol (C_2H_5OH) etc.[33], by applying different reaction conditions. Although it has moderate reaction conditions and variable products, the low efficiency of system, low activity and selectivity of products, poor mass transfer problems are the main concerns which prohibit its successful commercialization. Therefore, development of advanced catalysts, enhancement of mass transfer and carefully controlled reaction conditions are required for better performance of eCO_2RR.

1.3 Aim and Objectives

In current stage of CO_2 utilization using the electrochemical method, the bottleneck is the energy efficiency problem, which prohibits its commercial application. To facilitate this concept to become a reality, development of high quality electrocatalysts and good reaction electrolysers are the key issues. In my PhD study, electrochemical catalysts will be developed

and evaluated, and electrolysers special for eCO_2RR will be designed and manufactured. My study also tries to shed a light on improving CO_2RR from engineering design point of view. By combining with advanced catalysts, a low energy consumption, robust, and industrialisation possible CO_2 to fuel conversion system will be explored.

The **aim** of this research is to establish a complete eCO_2RR system and reduce CO_2 to renewable fuels. To achieve this concept, the first part will aim to develop a high-performance catalyst and specific process including nanoscale catalyst synthesis, physical characterization and electrochemical evaluation. The second part will aim to design and manufacture an advanced reactor with elevated mass transport which will improve the performance of overall reaction.

The **Objectives** of this thesis include:

- Development of Electrocatalyst

Electrocatalyst plays an important role on products' selectivity and energy efficiency, while a low performance of catalysts prohibits its development. Hence a high-performance and cost-effective catalyst will be designed, synthesized, and optimized. In this work, controlling of particle size and morphology of electrocatalysts are the key points for enhancement of catalyst properties.

- Design of electrolyser

Mass transfer of reactants, especially CO_2 is important for high reaction activity and efficiency. However, the low solubility of CO_2 in electrolyte reduces the reaction efficiency. Therefore, high-quality cells with good mass transfer of reactants will be studied to reduce the internal resistance. In this work, advanced-structured GDE cells are designed for eCO_2RR, to overcome the CO_2 mass transfer limitation.

- Investigation of influenced parameters

Selection of electrolyte, applied potential, assembly of working electrode have impacts on overall reaction mechanism, efficiency and products selectivity, while the effects are not clear so far. This study will optimize the reaction system by investigating the effects of these parameters.

1.4 Outlines of Thesis

This thesis is presented as a series of eight chapters.

Chapter 1- "Introduction" introduces the background of CO_2 problems, ways to utilize CO_2 and the aims and objectives of this thesis. Chapter 2- "Literature survey" provides the detailed literature review of electrocatalyst, electrochemical cell and electrode. Chapter 3- "Methodology" provides the detailed information about chemicals, catalyst synthesis technology, electrode fabrication, cell design technology, electrochemical methods used to test the catalyst, and characterization techniques. In Chapter 4- "Cu-contained catalysts for eCO_2RR", commercial and home-made Cu and Cu oxides have been used as electrocatalysts, and H-cell and CP-cell have been used for formation of CO. In Chapter 5- "ATO, ITO and In-MOF as catalysts for eCO_2RR", the ATO, ITO and In-MOF have been used as electrolytes. I will also demonstrate the influence of CO_2 mass transfer, concentration of electrolyte, pH of electrolyte, and achieve a high conversion efficiency of formate production. In Chapter 6- "Graphene Aerogel - Gas Diffusion Layer Exploration", I will synthesize the graphene aerogel (GA) and study GA's morphology and conductivity. In Chapter 7- "Hybrid Gas Diffusion Electrode Allows Directional Gas onto the Catalyst Bed for Enhanced CO_2 Electrochemical Reduction", I will report that bi-layer GDL configuration dramatically enhances the CO_2 mass transfer in eCO_2RR, and improve its durability as a result of electrolyte permeation prevention, and also study the FE of eCO_2RR products and compare with that of conventional H-cell. In Chapter 8- "Conclusions and Future Work" of my PhD thesis.

Chapter 2 Literature Survey

2.1 Overview of CO_2 eCO_2RR

Research towards eCO_2RR has been carried out to improve the reaction performance using novel catalysts with a high catalytic activity and low cost. New types of electrodes have been used to improve mass transfer, and alternative reactor design and fabrication have been explored to realize high efficiency and high selectivity of eCO_2RR. Fig. 2.1a shows the main research pathways, which include catalyst synthesis and characterization, renewable energy for eCO_2RR, electrochemical evaluation, and product analysis.

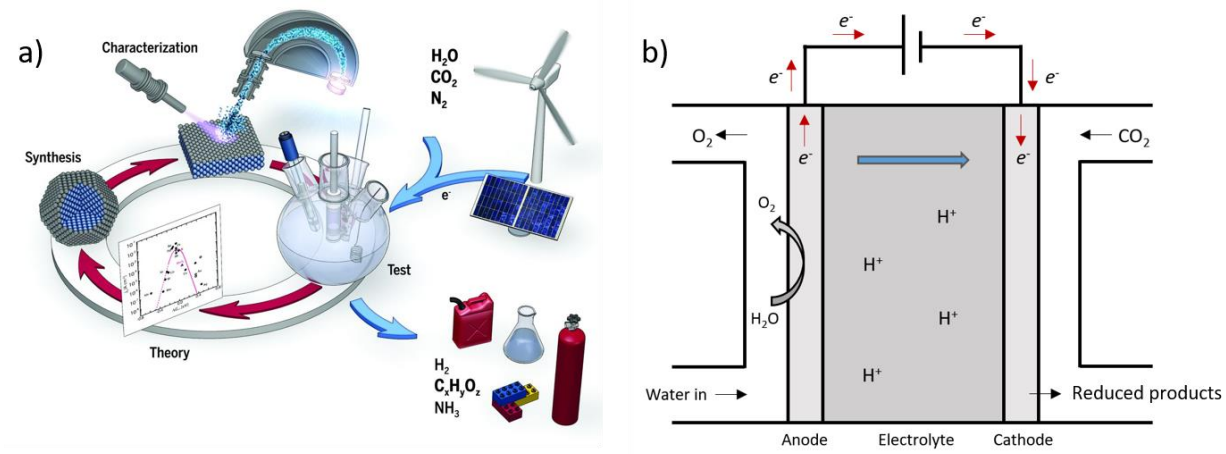

Figure 2.1 a) eCO_2RR research cycle[58] b) sketch of electrochemical reaction principle

The fundamental principle of eCO_2RR is schematically illustrated in Fig. 2.1b. The input current is supplied from external power sources, and the electrons are transferred from anode to cathode.

$$H_2O - 2e^- \rightarrow 2H^+ + O_2 \qquad \text{Eq. 2.1}$$

As the above equation indicated, the reaction happened on the anode side is the oxidation of water, where one H_2O molecule lost two electrons and release two protons and an oxygen.

Then the released protons are transferred onto cathodic side through the electrolyte. CO_2 is constantly supplied to cathode, then meets with protons and electrons. Finally, CO_2 is reduced to the renewable products (Eq. 1.3).

However, the actual circumstance is much more complicated than the ideal model of Fig. 2.1b. As the main final product of carbon-containing fuel, CO_2 molecules are inert and stable. From the thermodynamic aspect, Table 2.1 compares half-cell electrochemical reactions (cathodic) and their standard potentials (potential vs. standard hydrogen electrode, PH=7, 25 °C, 1 atm.). Some of the reactions (e.g. those with CH_4, C_2H_4) seem more favourable than HER. The actual process is much more difficult because of the formation of intermediate CO_2^{*-} anion radical, which can be initiated at -1.90 V with large kinetic barriers[36, 59, 60].

Table 2.1 eCO_2RR standard potentials in aqueous system, potential vs. standard hydrogen electrode (SHE)

Reaction equation	**E^o[V] vs. SHE at PH 7**
$CO_2 + e^- \rightarrow CO^-$	-1.90 V
$CO_2 + 2H^+ + 2e^- \rightarrow HCOOH$	-0.61 V
$CO_2 + 2H^+ + 2e^- \rightarrow CO + H_2O$	-0.52 V
$2CO_2 + 12H^+ + 12e^- \rightarrow C_2H_4 + 4H_2O$	-0.34 V
$CO_2 + 4H^+ + 4e^- \rightarrow HCHO + H_2O$	-0.24 V
$CO_2 + 6H^+ + 6e^- \rightarrow CH_3OH + H_2O$	-0.38 V
$CO_2 + 8H^+ + 8e^- \rightarrow CH_4 + 2H_2O$	-0.24 V
$2H^+ + 2e^- \rightarrow H_2$ (HER, side reaction)	-0.42 V

Formation of CO_2^{*-} imposes a significant overpotential to the reaction, which requires more energy input and is believed as the rate determine step[61]. Moreover, reduction products of CO_2

could be numerous. From commercialization aspect, one or two main products in different phases are desirable, which means the selectivity of products should be considered.

A proper electrocatalyst is required to reduce the energy barrier and enhance the electrochemical process. Catalysts with high activity, high selectivity and long lifetime need to be developed. Moreover, design of eCO_2RR reaction cell is an indispensable aspect which will influence the mass transfer of the reactants, conductivity, and stability of the system. It determines the current density and FE of the overall reaction[62]. Based on these concerns, an eCO_2RR research system can be described as shown in Fig. 2.2[58, 63]. To achieve a high efficiency reaction system, we should focus on catalyst development, reaction cell design and electrochemical evaluation.

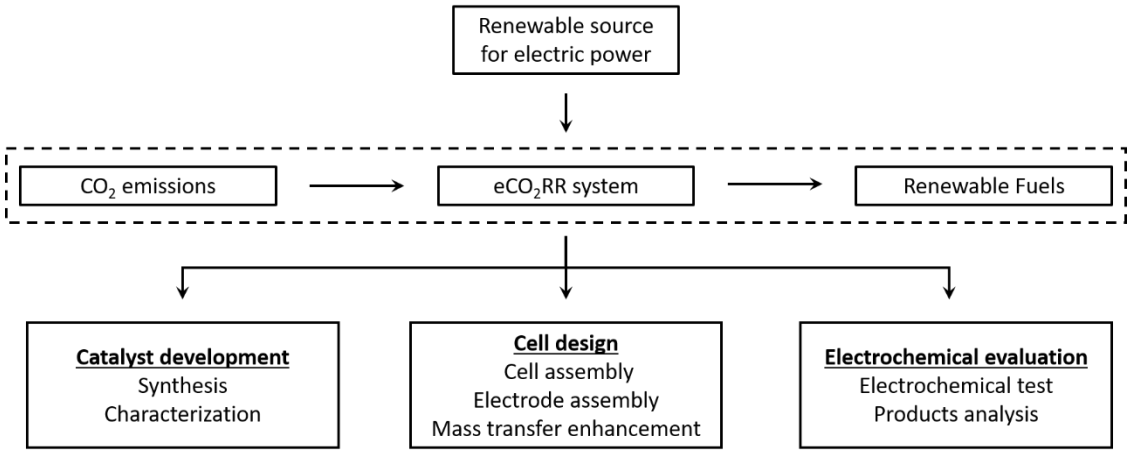

Figure 2.2 eCO_2RR research system

2.2 Electrocatalyst

Catalysts are usually used to reduce the activation energy (E_c) during chemical reactions, and enhance the reaction rate[64]. For electrochemistry, a good electrocatalyst needs to exhibit both high energy efficiency and high current density of the electrochemical reaction[65, 66]. These will reduce the overpotential with an enhanced reaction rate (corresponding to high current density

and high activity), enhanced selectivity and efficiency of aimed products. As shown in Fig. 2.3, the solid line indicates the reaction without the catalyst, where the energy difference between CO_2 and CO_2^{*-} indicates the activation energy throughout the reaction, reflects a relevantly high overpotential during electrochemical evaluation. While the dashed line shows the reaction where catalyst participates in a reaction, the existence of catalyst reduces the activation energy presents much lower overpotential.

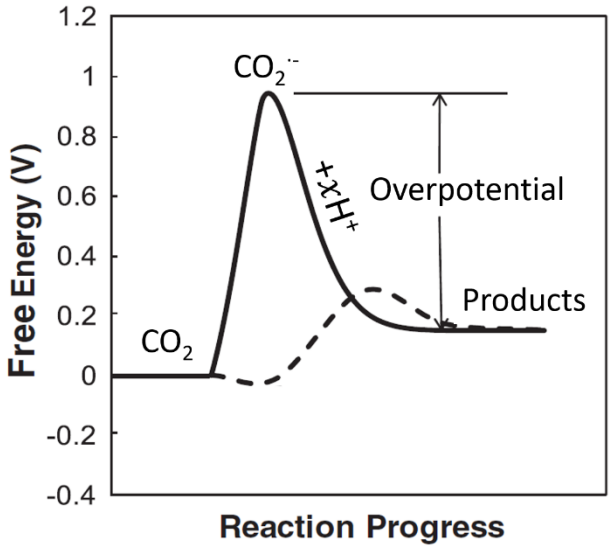

Figure 2.3 Schematic of eCO_2RR activation energy in presence of catalyst (dash line) and absence of catalyst (solid line), more activation energy (overpotential) is required without catalyst, adapt from ref[66]. An ideal electrocatalyst presents lower overpotential in eCO_2RR.

Much research effort has been devoted on designing novel catalysts, by introducing different metals, various morphology[67], controlled crystallization[68] and particle size[69] for the purpose of catalysis property enhancement.

2.2.1 Metallic Catalysts

Elemental metals are the earliest and most investigated electrocatalyst for eCO_2RR. Based on the reduction products, the metals can be divided to three groups from the reaction-route

aspect[70]. The main products including CO, $HCOO^-$, hydrocarbons, alcohols etc. are shown in Fig. 2.4.

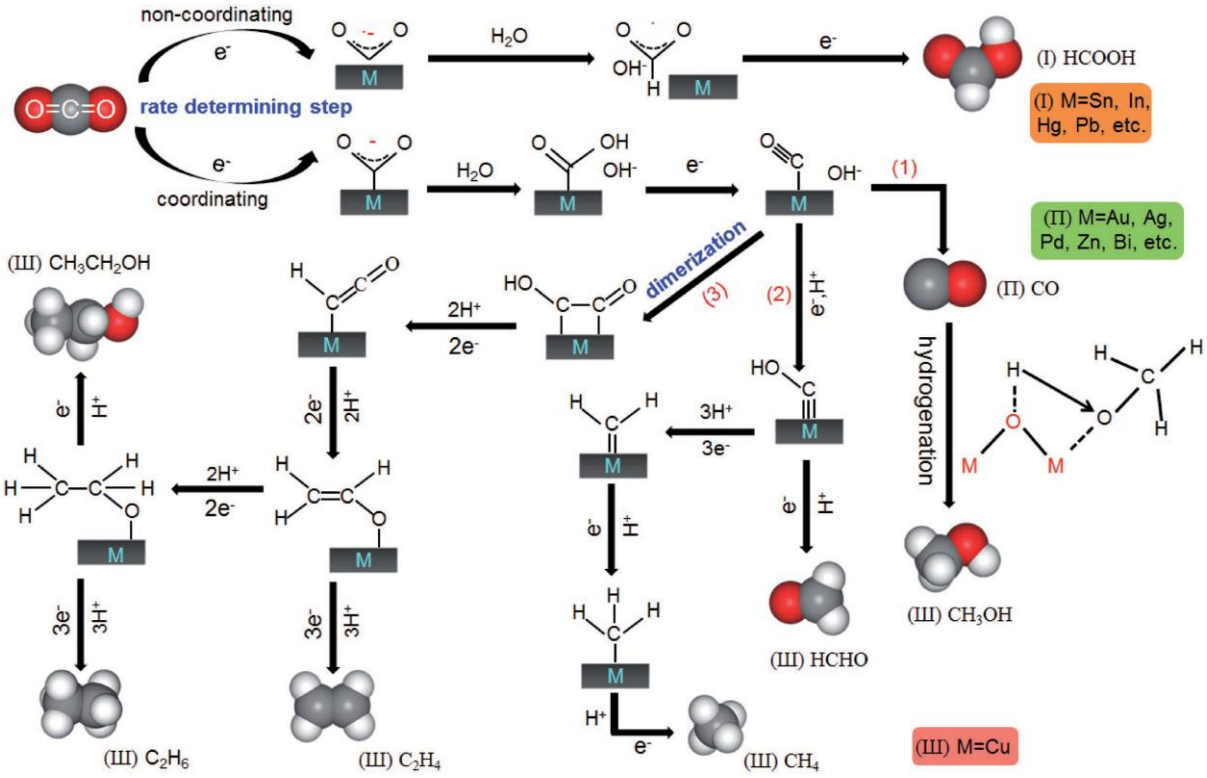

Figure 2.4 Reaction pathways for eCO_2RR on metals[36, 71]

- *Sn, In, Hg, Pb, Sb etc.*

This group of post-transition metals or metalloid are classified to mainly produce $HCOO^-$ or HCOOH, due to their weak bonding with CO_2^{*-} intermediate[72]. As shown in the following equations, the CO_2^{*-} intermediate can hardly be absorbed and it tends to be protonated at the carbon atom, thus forming $HCOO^*$ (Eq. 2.2). The intermediate receives one electron and ultimately transforms into formate or formic acid as the major reduction product (Eq. 2.3).

$$CO_2^{*-} + H^+ \rightarrow HCOO^* \qquad \text{Eq.2.2}$$

$$HCOO^* + H^+ + e^- \rightarrow HCOOH \qquad \text{Eq.2.3}$$

A typical catalyst such as Tin (Sn), presents a high FE towards formate but a low efficiency (current density) due to its rapid oxidation upon exposure to air. The surface oxide layer would greatly influence the electrochemical process. Hori *et al.*[73] reported to use Sn in eCO_2RR application, where they tested Sn bulk metal in 1 M $KHCO_3$ -1.4 V vs. SHE with 65.5% - 79.5% FE of formate, while the current density is 5.5 $mA \cdot cm^{-2}$. It shows a relevantly low activity of electrocatalysis due to low active sites of bulk metal and surface oxidation behaviour. To enhance the properties of Sn catalyst, Zhang *et al.*[74] used tin oxide nanocrystals loaded on carbon black and graphene to obtain more active site for eCO_2RR, and achieved an enhanced FE of formate to 93% in 0.1 M $NaHCO_3$ at -1.8V vs. saturated calomel electrode (SCE), where the current density is about 9 $mA \cdot cm^{-2}$. Zhao *et al.*[75] used an electro-deposited method to enhance the properties of Sn catalyst, and achieved 91% FE of formate and a current density of 15 $mA \cdot cm^{-2}$ tested in 0.1 M $KHCO_3$ at -1.4V vs. SCE. However, the low activity of Sn-based catalyst has still not been fully resolved.

Indium (In) is another potential catalyst for formate production, it is low toxic and environmental-friendly. However, In has not been fully developed in eCO_2RR due to its low stability and low current density. Xia *et al.*[76] reported a dendritic In foams in 0.5 M $KHCO_3$ (pH=7.2) at -0.86 V vs. RHE, and yielded a considerable FE of formate up to 86%, where the current density is 5.8 $mA \cdot cm^{-2}$. In-based catalysts present a low current density and require restricted reaction conditions which limits its application, thus more advanced-structured catalysts are required.

- *Au, Ag, Pd, Zn, Bi etc.*

The second group of metals including Au, Ag, Pd, Zn and Bi. These metals can tightly bind with $HCOO^*$ intermediate (Eq. 2.4). Once the $HCOO^*$ receives a proton from the electrolyte,

CO intermediate will be generated from the catalyst surface, then the CO will be produced as the predominant product (Eq. 2.5)[77].

$$CO_2^{*-} + H^+ \rightarrow HCOO[M] \quad \text{Eq. 2.4}$$

$$HCOO[M] + e^- \rightarrow CO + [M] + OH^- \quad \text{Eq. 2.5}$$

This type of catalysts has been proved to have high FEs of CO in eCO_2RR. Noble metals such as Ag and Au show considerable catalytic activities in 0.1 M $KHCO_3$ at an ambient condition. The FEs for CO production are 64.7% (Ag, 99.98%) and 81.5% (Au, 99.95%) at -1.6 V vs Ag/AgCl[78]. In a recent study, Cheng *et al.*[79] employed highly porous gold films supported on silver foil in 0.1 M $KHCO_3$ electrolyte. They have achieved increased surface area of catalyst and obtained the 90.5% FE for CO with a current density of 8.3 mA•cm^{-2}, at -0.5 V vs. SCE. However, the cost of noble metal is high, thus alternative catalysts with lower cost are required for commercialization concerns.

Comparing with noble metals, a low cost and earth-abundant metal such as zinc (Zn), is regarded as a promising electrocatalyst with high selectivity towards CO production. However, its stability and activity are the hurdles to overcome. Hattori *et al.*[80, 81] explored to use bulk Zn and obtained 70% FE of CO at -1.4 V vs. Ag/AgCl with a current density of 2 mA•cm^{-2}, while the rapid oxidation of bulk Zn surface reduced the reaction efficiency. Therefore, nanosized Zn, such as the electrodeposited dendrites were developed to enhance the FE[82]. However, the low stability of Zn caused the inevitable oxidation during electrolysis, and the morphology of catalyst such as particle size, shape, crystallinity etc. should be controlled.

- *Cu*

Copper is the only metal which is capable of converting CO_2 into high value added carbonaceous and alcohol[83-85]. It is capable of binding *CO intermediates and converting them into alcohols or other hydrocarbons from *COH or *CHO intermediates via dimerization pathways[86], based on the following reactions.

$$* CO + 4H^+ + 4e^- \rightarrow CH_3OH \quad \text{Eq. 2.6}$$

$$* CO + H^+ + e^- \rightarrow * COH \; \boldsymbol{or} \; * CHO \quad \text{Eq. 2.7}$$

$$* COH \; \boldsymbol{or} \; * CHO + xH^+ + xe^- \rightarrow HCHO, CH_4, C_2H_4, C_2H_6, etc. \quad \text{Eq. 2.8}$$

The C_1 (one-carbon molecules) products such as methanol (CH_3OH) can be produced through hydrogenation pathway. For example, Jaramillo *et al.*[87] demonstrated the formation of CH_3OH pathway through *COH or *CHO intermediates. Methane (CH_4) and methanal (HCHO) were generated via formation of *COH or *CHO. C_2 (two-carbon molecules), C_3 (three-carbon molecules) products were proceeded via dimerization of *CO intermediates.

Higher energy density of C_1, C_2 and C_3 products made them become more favourable for industrial production. However, its low selectivity, activity degradation, and relevantly large overpotential (nearly 1 V) are the hurdles for practical applications[88, 89]. Hori *et al.*[73] employed a 20 mm × 20 mm Cu sheet in 1 M $KHCO_3$ at -1.39 V vs. SHE and obtained mixed results with reduced products of formate (FE: 15.4 -16.5%), CO (FE: 1.5 – 3.1%), CH_4 (FE: 37.1 – 40.0%). Jaramillo *et al.*[90] demonstrated 16 different CO_2 reduction products on copper surfaces across a range of potentials. However, great efforts should be made in order to enhance the selectivity, stability, and reduce the overpotential.

2.2.2 Catalyst Design Strategies

Based on the metallic catalysts discussed above, several design strategies are identified to enhance the catalytic performance.

- Nanoparticles

As the most common and popular approaching method, nano-structuring is believed to promote the performance of catalysts[91-93]. By reducing the catalysis particle size to nanoscale, the active sites are dramatically increased by its considerable surface area. The minimized catalytic thickness can reduce the transfer barrier of reactants to active sites, which can achieve a lower overpotential[94]. Moreover, precisely controlling of catalysis morphology at an atomic scale with various nanostructures such as nanotubes, nanosheets, nanowires etc., is believed to enhance the catalyst property in eCO_2RR. These nanostructured catalysts bring structural defects such as vacancies or grain boundaries, which are served as active sites for eCO_2RR[36]. For example, Dai *et al*.[95] reported an ultra-stable Cu/$Ni(OH)_2$ nanosheets, and achieved a low overpotential reaction by using hybrid catalytic structure, and obtained a high FE for CO (92%) at an overpotential of 0.39 V vs. SCE with a current density of 4.3 $mA \cdot cm^{-2}$, in 0.5 M $NaHCO_3$. Ma *et al*.[96] introduced a Cu nanowire for eCO_2RR, by increasing the length of the catalyst, and the selection of C_2 products was enhanced. When the length of Cu nanowires was above 2.4 ± 0.56 mm, n-propanol was detected with CO, HCOOH and C_2H_4. Whereas when the length of nanowire is above 7.3 ± 1.3 mm, C_2H_6 formation was observed along with ethanol[94].

- Doping or Alloying

Employing foreign atoms by doping or alloying method is an effective way to adjust the binding energy of CO_2 intermediates, thus the activity and selectivity of eCO_2RR can be modulated[97]. Stronger CO_2^{*-} binding elements (e.g. Ni, Co and Pt based catalysts) prefer formatting CO product, while weaker CO_2^{*-} binding elements (e.g. Sn, Hg and Pb based

catalysts) promotes the formation of fromate[98]. By combining these two types of elements, an intermediate CO_2^{*-} catalyst interaction can be achieved that promotes the formation of higher-value reduction products.

- Metal-carbon Hybridization

Electron transfer is one of the key aspects in eCO_2RR, where electricity drives the catalytic reactions. Therefore, a large surface area and conductive carbon substrate (e.g. graphene[99], carbon nanoparticles[100], carbon nanotubes[101], carbon fibres[102]) can greatly benefit the electron transfer to/from electrocatalysts and serve as the supporting material for a better metallic dispersion. Moreover, the interactions between electrocatalyst and substrate may also supply strong activity and selectivity enhancement. However, the involved carbon materials could promote the HER reactions. This competitive reaction will consume the reactants of eCO_2RR (protons and electrons) and reduce the CO_2 conversion efficiency. Therefore, the balance of benefit and side-reaction problem should be concerned.

- Metal-organic Framework

MOF has its novelty due to its ordered structure, high porosity and single metal site dispersion. It allows for free permeation of protons and dissolving of CO_2 into the MOF, where MOF shows a great potential for eCO_2RR applications[103, 104]. Moreover, the high crystallinity of the MOF can be employed as a platform to investigate the active sites and reaction pathway, which can be developed into high-efficient electrocatalysts. Hod *et al.*[105] reported a Fe-porphyrin-based MOF films and achieved 50% FE for CO at -1.3 vs. SHE. in organic solution (1M tetrabutylammonium hexafluorophosphate or $TBAPF_6$ in dimethylformamide or DMF). As one of the common MOF, zinc imidazolate MOF (ZIF-8) presents good activity and selectivity of

CO, and 65% FE for CO has been achieved at -1.8 V vs. SCE in 0.5 M NaCl, reported by Wang *et al*.

2.2.3 Development of Catalyst in this Project

There are different types of electrochemical catalysts as introduced so far. However, a high-performance catalyst is required for eCO_2RR. In order to achieve this, firstly, nano-sized catalysts can be introduced, aiming to increase the active sites on catalyst surface and enhance the catalysis activity. Secondly, the formate and C_2, C_3 favoured metals can be selected as the key metals during catalyst synthesis, because these products have a higher energy density compared with CO. Thirdly, the catalyst structure should be designed in order to achieve its best property.

Based on this, copper-contained catalysts including commercial Cu and Cu_2O, self-synthesised Cu_2O and graphene supported Cu oxides were employed in my research, aiming to obtain high value-added products with good reaction activity and selectivity of determined products. The performance of Cu-based catalyst is dependent on catalyst morphology, crystallinity and coordination number etc.[106, 107], which are carefully concerned in this study.

Antimony tin oxide (ATO): Antimony oxide and tin oxide are reported to have good activity on generating formate[108,109], while ATO has not been reported in eCO_2RR. This bi-metal oxide catalyst can also adjust the binding energy of CO_2 intermediates which benefit the selectivity and reaction activity. Therefore, nano-sized ATO was used in this study, and GDE cells were also introduced to enhance the mass transfer. The aim is to assess its activity and efficiency of formate.

Indium tin oxide (ITO): Indium is a non-noble metal which has emerged as a CO_2RR catalyst for selective formation of formate with high FE (≥75%), and tin oxide has its potential on formation of formate. However, the activity of indium is usually low. In this study, we used nano-sized ITO in GDE cell, and the aim is to achieve high efficiency and high activity reaction system for eCO_2RR from mass transfer aspect.

Indium MOF: Indium is believed to have high selectivity of formate with a low activity. MOFs are porous coordinating polymers or networks, made up with a metallic component, pore space and the organic linker. This advanced structure can enhance the CO_2 capture and provide more active point for CO_2 reduction, which can help to develop the overall reaction efficiency[110]. In this study, we introduced an indium MOF (this catalyst was synthesized by Inorganic Chemistry Group from Manchester University) and then used the GDE cell for electrochemical evaluation. The aim is to achieve a high efficiency and high activity reaction system with a low energy consumption.

2.3 Electrochemical Cell

Design of electrochemical cell is an essential aspect for the eCO_2RR process. A new design of gas flow channel/chamber, and improved gas diffusion electrode could dramatically influence the FE and stability of the chemical reactions[62]. A typical CO_2 electrochemical reaction in electrolytic cell normally consists of four components: e.g., a cathode with catalyst for eCO_2RR, an anode for oxygen evolution reaction, an electrolyte providing the path for reactants and/or products mass transfer, and a polymer membrane to separate catholyte and anolyte with ion selectivity[62]. During the eCO_2RR, ions are transferred across the membrane, and electrons are driven by an external power source. Meanwhile, a reference electrode (normally inserted in catholyte) is used for potential measurement. From the cell design aspect, selection of

membrane and electrolyte, reaction condition, cell structure presents great influences on the reaction process. The reduction reaction results can be varied due to the differences in mass transfer of reactants and reaction mechanism, even though the same catalyst is used.

2.3.1 Types of Cells for eCO_2RR

Many cells for eCO_2RR have been designed and reported in literature, including H-type cell, gas diffusion electrode cell, polymer electrolyte membrane flow cell, microfluidic flow cell etc. Different cells present the unique properties for eCO_2RR.

- Conventional H-type cell (H-cell)

H-cell is one of the most commonly used lab-scale reactors for eCO_2RR. Within the cell, the working electrode and counter electrode are assembled in cathodic chamber and anodic chamber, respectively. These two chambers are separated by an ion-exchange membrane to separate the products. Electricity is supplied by external power sources for the reaction. The overall assembly shows a typical 'H' shape, as illustrated in Fig. 2.5. The working electrode can be chosen from metal sheet, foil, mesh, or powder catalyst supported on a conductive substrate (e.g. carbon paper). During the electrochemical tests, CO_2 gas is constantly supplied into cathode chamber and dissolved in the catholyte. Then the CO_2 diffuses to the catalyst surface and is reduced into the final products. The gas products are collected from gas outlet, and liquid products are collected form electrolyte after electrochemical process for further analysis.

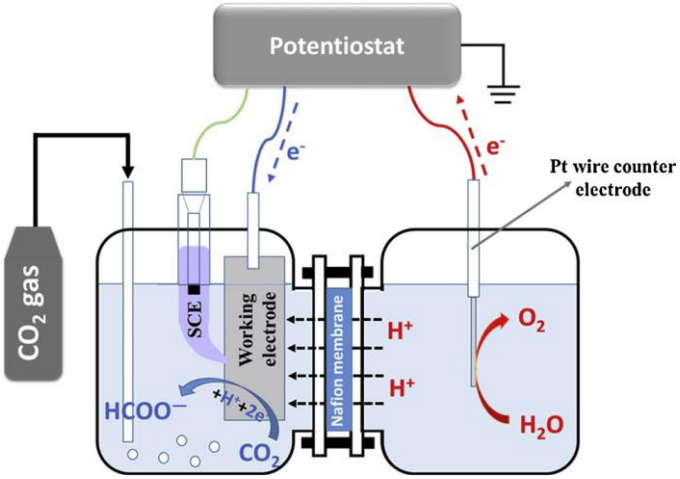

Figure 2.5 A schematic of the conventional H-type cell, Zhao *et al.*[75]

However, HER is a competitive reaction which also happens in the H-cell[111]. The low solubility of CO_2 in the aqueous system will cause a CO_2 mass transfer, and result in the HER and will reduce the FE for the eCO_2RR. Moreover, a long distance between working electrode and counter electrode will result in a relevant high electrolyte resistance and also a higher overpotential.

To solve these problems, Kuhl *et al.*[90] designed and fabricated a compact electrochemical cell (Fig. 2.6) with a large working electrode and small electrolyte volume. Low overpotential and enhanced current density have been achieved owning to large surface area of electrodes to electrolyte volume ratio, narrowed distance between working electrode and counter electrode. The concentrations of liquid products were also increased due to the low chamber volume, and the minor products could be detected.

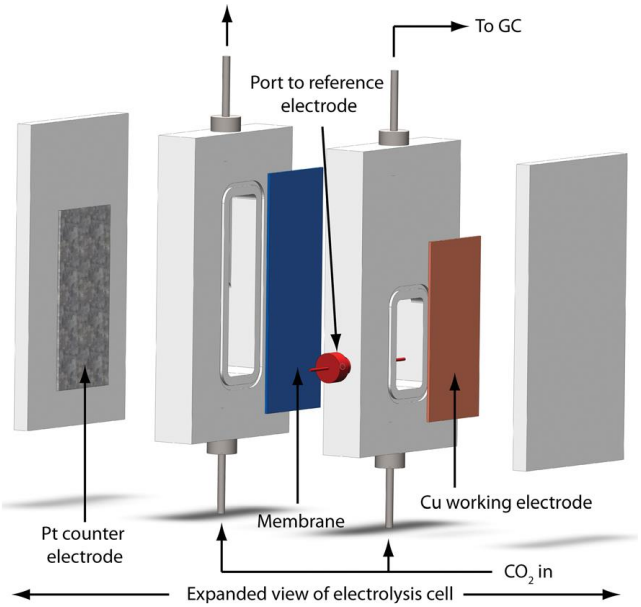

Figure 2.6 Schematic of the compact electrochemical cell designed by Kuhl *et al.* [90]

- Gas Diffusion Electrode type cell (GDE-cell)

The GDE electrode is typically used for the flow cell within eCO_2RR reactors. It has a porous structure and the GDE is usually prepared by depositing electrocatalyst onto a gas diffusion layer (GDL). In this configuration, the gas reactant could reach to the interior of electrode with catalyst layer and contact with electrolyte to form three-phase interface: 'gas (CO_2) - liquid (electrolyte) - solid (catalyst)'. This configuration significantly enhances the mass transfer of CO_2. GDE-cell (Fig. 2.7) is a combination of GDE and H-cell, where its cell configuration is similar with H-cell, combined with cathode half-cell and anode half-cell. The cathode half-cell consists of a gas chamber and a catholyte chamber. A catalyst coated GDL is introduced to separate these two chambers as working electrode, and CO_2 is constantly suppled from the gas chamber. The CO_2 then diffuses across GDL then reaches the catalyst layer. An ion exchange membrane is placed between catholyte and anolyte. The reference electrode is placed in catholyte. The counter electrode can be platinum wire or plate, which is immersed inside the anolyte.

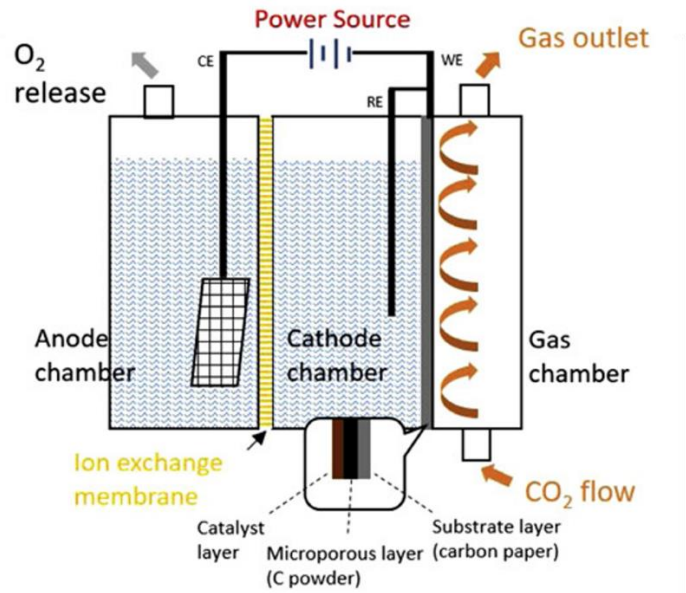

Figure 2.7 Schematic diagrams of GDE-cell in aqueous eCO_2RR system[111]

- Polymer Electrolyte Membrane Flow Cell (PEMFC)

The concept of this cell construction is originated from proton exchange membrane - fuel cell. This configuration has its potential for eCO_2RR mass transfer enhancement, which could significantly enhance the current density to over than 100 $mA \cdot cm^{-2}$. Comparing to the H-cell, the flow cell can overcome the mass transfer problems through a continuous circulation of electrolyte. Its large electrode surface area vs. electrolyte volume could reduce the transfer distance of reactants which helps to reduce the internal resistance. Besides, the higher CO_2 concentration at the catalyst surface and the lower liquid products in catholyte will promote the eCO_2RR[62, 90]. The structure of GDE flow cell (Fig. 2.8, reported by Narayanan *et al.*[112]) is similar to the PEMFC, where a membrane is sandwiched between cathode and anode. This construction is called membrane electrode assembly (MEA). Adjacent to the electrodes are the current collectors and flow field plates.

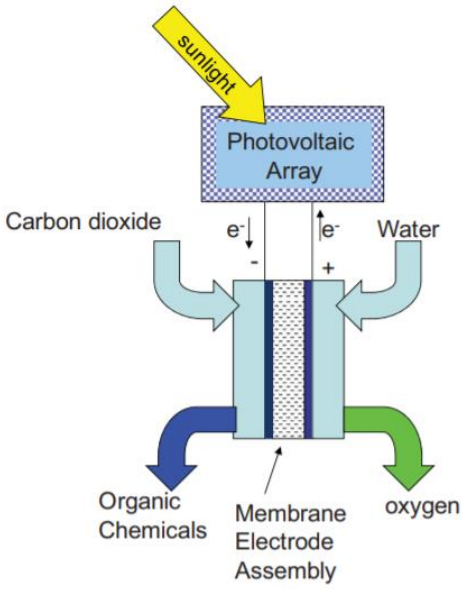

Figure 2.8 Schematic of polymer membrane electrochemical cell[112]

Although the polymer electrode membrane enhances the mass transfer of reactants to a certain extent, the low CO_2 molar concentration still causes the problem such as a low solubility of the reactant. In order to solve this problem, a GDE configuration has been introduced in flow cell (Fig. 2.9), and the PEM, cathode GDE and anode GDE are formed as an MEA. The material of GDL is a conductive and porous structure composed of carbon paper or carbon cloth. It is hydrophobic which allows gas to crossover and prohibit the liquid. Based on this construction, CO_2 could directly reach to the catalyst surface without dissolving into the solution and also contact with the bulk electrolyte to form a three-phase interface. By solving the mass transfer problem of CO_2, the reaction of hydrogen evolution is limited and the FE of eCO_2RR process is enhanced.

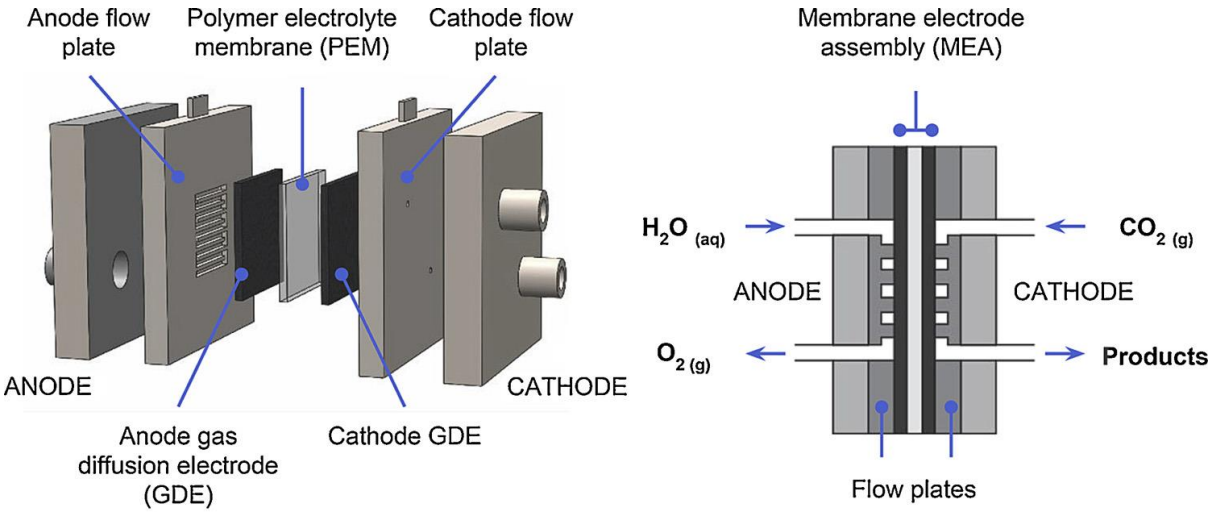

Figure 2.9 Schematic of gas diffusion electrode type polymer electrolyte membrane flow cell[113]

- Microfluidic flow cell (MFC)

The configuration based on an MFC consists of a very thin (< 1 mm) flow electrolyte channel with a 0.5 × 2 cm window placed between two GDEs, which separates the anode and cathode without any membrane. In this configuration, gaseous CO_2 is supplied into cathode side then diffuses through a porous GDL and finally reacts at the catalyst/electrolyte interface. The products can be diverted out of the cell with an electrolyte stream. Compared with other reactors containing with PEMs, this cell effectively separates the reduction and oxidation products through diffusion of products. The reference electrode is normally assembled in the outlet of the electrolyte stream or inserted in the electrolyte stream[113]. A schematic drawing of MFC cell is shown in Fig. 2.10.

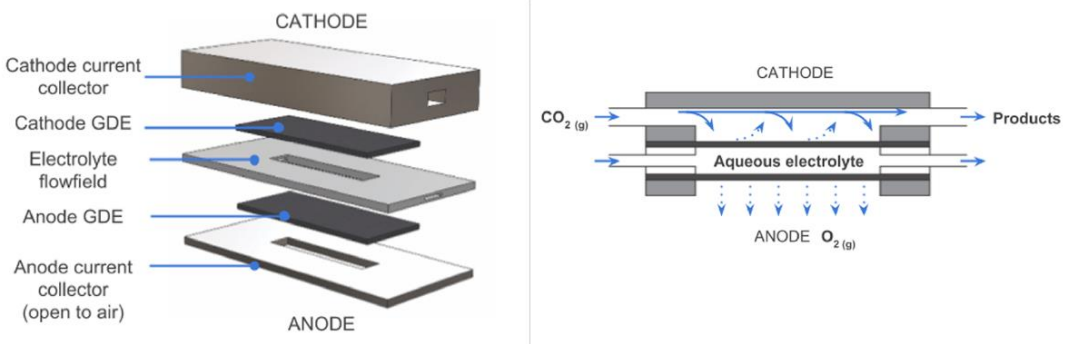

Figure 2.10 Schematic of microfluidic reactor, CO_2 is supplied into cathode then it diffuses to the catalyst-electrolyte interface. oxygen evolution reaction take place at the anode and is vented to air[113]

- Other type of cells

Apart from the cells discussed above, some other types of cells were developed by the researchers. One of them is solid oxide electrolyser cell (SOEC), which is operated at a high temperature (> 873 K) rather than ambient condition[114]. Differential electrochemical mass spectrometry (DEMS) cell is specially designed for analytical technique, which utilizes pervaporation to continuously separate and collect electrochemical reaction products efficiently in real time and analyse products in approximately one second[115].

2.3.2 Concept for Electrochemical Cell Design

The Table 2.2 shows the applied conditions for eCO_2RR.

Table 2.2 Different substrate for electrodes, CO_2 feeding types, membrane types and operation temperature for various classes of cell in CO_2 electro-reduction processes[62].

Cells type	**Substrate**	**CO_2 feeding type**	**Membrane type**	**Operation temperature**
H-cell	Glassy carbon[116], carbon paper[117], Metal foil[118]	CO_2 saturated solution[116-118]	CEM[116, 117], AEM[118]	Ambient condition
GDE-cell	Carbon paper[111], Graphene aerogel[119]	Gas feed[111, 119]	CEM[111, 119]	Ambient condition
PEMFC	Carbon paper[112], GDL[120, 121]	CO_2 saturated solution[112], Gas feed[120, 121]	Nafion[112], AEM[112, 121], CEM[120]	Ambient condition
MFC	GDL[66, 122]	Solution + gas feed[66, 122]	Nafion[66], AEM[122]	Ambient condition
SOEC	The electrolyte tube[123]	Air + CO_2 gas[123]	N/A	800 °C

Among the electrolysers introduced above, GDE-cell is a promising type with promising CO_2 mass transfer mechanism, ambient reaction condition and easiest cell construction. In my PhD thesis, an eCO_2RR electrolyser was designed and manufactured based on the GDE cell configuration. Then the property of designed cells was evaluated. The simulation technology

was also applied to analysis the CO_2 mass transfer, overpotential, current density to maximize the efficiency. Design of cells was done using the SOLIDWORKS® and the 3D-printing technique was employed for cell manufacture.

2.4 Electrode Design for eCO_2RR

In the eCO_2RR process, the working electrode forms the function of catalyst substrate and conductor, and supplies the place for the reduction reaction. Design of electrode can greatly influence the mass transfer of reactants, surface area towards the electrolyte and internal resistance of cell[124]. Therefore, design of a high-performance working electrode should be explored. Several types of electrodes are concluded in the following sections, such as metal sheet electrode, metal mesh electrode, GDE etc.

2.4.1 Type of Electrodes

- Metal Sheet Electrode

Metal sheet electrode is one formation of electrode for eCO_2RR. It is normally immersed in electrolyte where its 2D surface provides large surface areas for eCO_2RR. It is commonly reported in H-cell and GDE-cell. Metal sheet electrodes can be classified into pure foil, porous foil and nanoparticles supported foil. The process treatment of electrodes causes the foil with different surface areas.

Pure metal foil electrode was reported in early stage research. For example, Hori *et al.*[73, 125] discovered that methane and ethylene can be produced at Cu electrode in 0.5 M $KHCO_3$. The current density was obtained to be 5 mA•cm^{-2}, with a FE of CH_4 about 65% at 0 °C, and C_2H_4 with 20% at 40 °C. Kim. *et al.*[126] reported the reduction of CO_2 to CH_4 on Cu foils at room

temperature using Cu foil as electrode. They prepared Cu polycrystalline sheets in 0.5 M $KHCO_3$ at -0.50 V vs. SCE under the ambient condition, achieving the transition of CO_2 to CH_4 with a current density of 17 $mA•cm^{-2}$.

Researchers have also found that the eCO_2RR is limited by lacking mass transport, and they found a larger surface area could provide more active sites which can contribute larger current. Seddon *et al.*[127] employed gold thin film spun onto polymer sheets with thickness of 1 and 4 μm as shown in Fig. 2.11. By enhancing diffusional transport to a finite electrode surface under microscopic size, the current has been significantly increased.

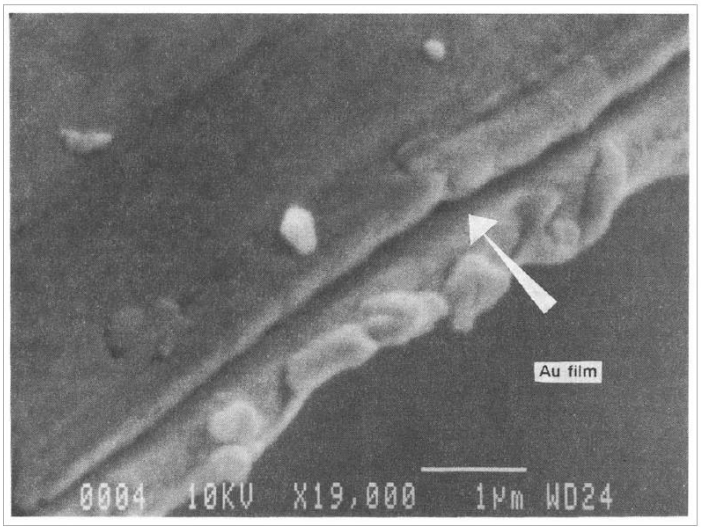

Figure 2.11 SEM of the thin layer photoresist edge of a polymide/gold/photoresist image with 1 μm thickness of gold film[127].

Oxidation treatment of metal sheet is another method for electrodes preparation. Metal oxides provides good chemical functionality, which can stabilize the incipient negative charge on CO_2 and mediating the electron transfer[128]. For example, Le *et al.*[129] reported that cuprous oxide thin films have obtained 43% FE of CH_3OH with 43 $μmol•cm^{-2}•h^{-1}$. The morphology of this catalyst is shown in Fig. 2.12. When the HCO species forms, carbon atom contributes protons

and electron transfer reactions will result in the formation of H_3CO^*. Following this pathway, the last proton transfer to the H_3CO^* species adsorbates for CH_4 formation. In the case by the presence of cuprous oxide, it will benefit the ability of H^+ species coordinated with surface bound oxygen to form CH_3OH.

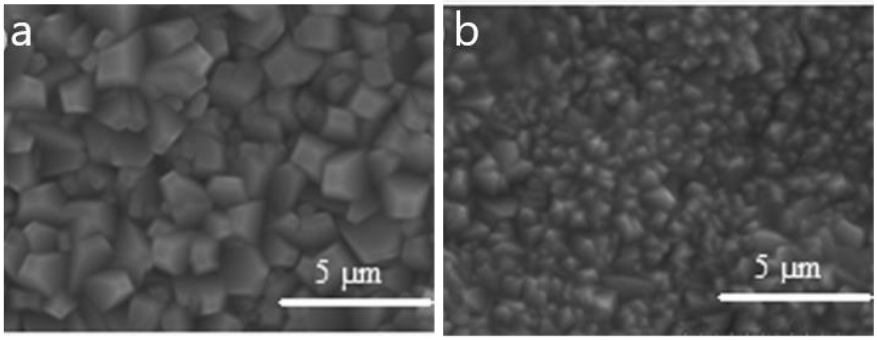

Figure 2.12 Electrodeposited cuprous oxide film a) before reaction and b) after reaction[129]

Porous structured metal sheet electrode was reported by Jia *et al.*[130], and they showed an alloy/de-alloy method can manufacture nano-porous film in order to get high surface material. They used an electrodeposition method to obtain several types of nano-porous metal films. The process introduced electrodeposition of Zn on metal film including Cu, Ag and Au, then these surfaces were then thermo-treated and immersed into the etching solution to get nano-porous patterns. In this case, porous structure provides a large surface area, thus enhancing the number of active sites and mass transfer of electrons. Chen *et al.*[131] developed a porous Au structure on Ag film, which obtain a large surface area and promote the ion transfer **(**Fig. 2.13).

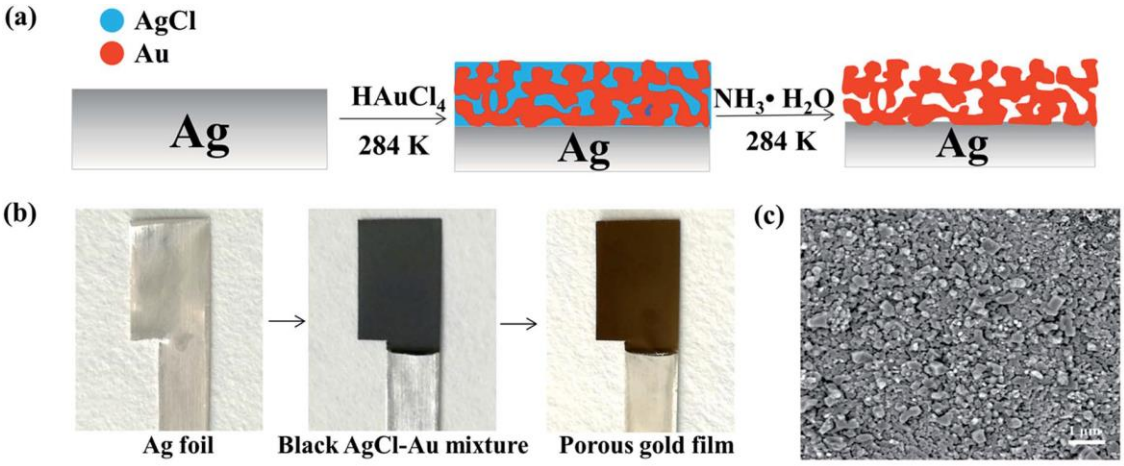

Figure 2.13 Fabrication and characterization of porous gold films. a) Schematic illustration of the key steps in fabricating porous gold films. b) Optical images of the polycrystalline Ag foil (left), black AgCl-Au precursor 4 and porous gold film lying on the Ag foil (right). c) SEM image of the porous AgCl-Au precursor[131].

- Metal Mesh Electrodes

Metal mesh electrodes with a microporous structure allow the gas to across over and form gas (CO_2)-liquid (electrolyte)-solid (catalyst layer) three-phase interface (Fig. 2.14)[132, 133]. Ogura *et al.* [132, 134] developed a three-phased design assisted with a mesh structure. They established a vertical assembled cell and performed the CO_2 reduction at its three-phase interface. CO_2 was recycled constantly in the device which enriched the CO_2 concentrations on the interface, therefore enhancing the performance of eCO_2RR. In their study, a CuBr-mediated Cu-mesh was applied as the working electrode, and the result indicates 90% of CO_2 conversion rate with 75% selectivity for C_2H_4.

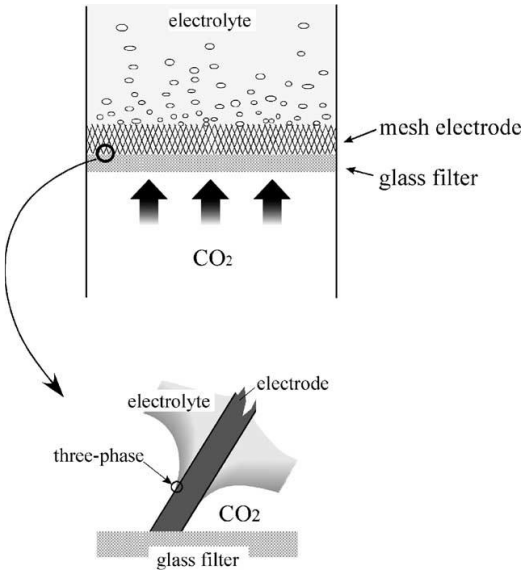

Figure 2.14 Schematic representation of three-phase (gas/liquid/solution) interface[132].

- Gas Diffusion Electrodes

Gas diffusion electrodes (GDEs) have been firstly proposed in fuel cell application since 1967[135]. GDL are normally involved in GDE type cells for eCO_2RR[136], and the material are normally carbon paper, carbon cloth or metal foam. This concept is inspired from PEMFC design, and GDL are involved in eCO_2RR application aims to enhance the CO_2 mass transfer [111, 137]. In recent studies, Higgins *et al.* [138, 139] indicated that GDEs present excellent mass transport properties compared with conventional aqueous-phase CO_2 reaction, therefore, the poor solubility problems of CO_2 in the aqueous electrodes can be solved. They supplied CO_2 to cathode through gas phase rather than aqueous phase (Fig. 2.15), which is a solution for resolving the performance and solubility challenges. It also provides a robust support for catalysts, gas permeability, which prevent the electrode being flooded by electrolyte and provides electron transfer pathway.[140]

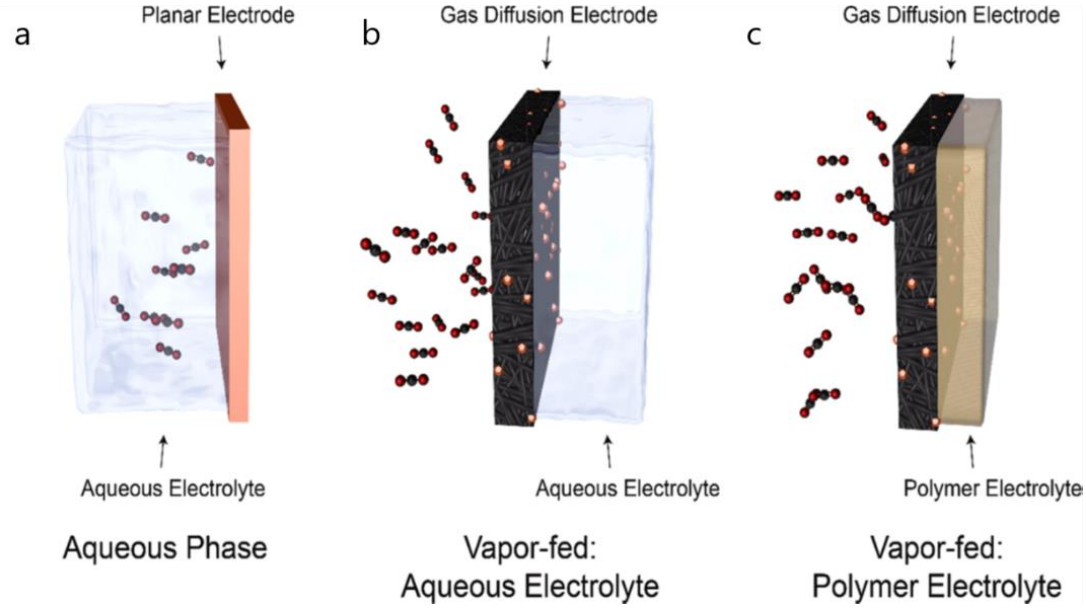

Figure 2.15 Different eCO_2RR reactor schemes. a) Aqueous phase eCO_2RR, where CO_2 is first solubilized in an aqueous electrolyte and then reduced at a catalyst surface. Vapor-fed eCO_2RR employing an b) aqueous or c) polymer electrolyte[138].

Carbon paper is a commonly used material as GDL in GDE assembly. It is typically hydrophobic. In practical use, 2D structured carbon paper is permeated after long-term reaction. The surface and pores are blocked by electrolyte which impedes the gas mass transport to catalyst layer[141]. Therefore, a new material should be explored for better performance of durability.

2.4.2 Carbon for Electrode Assembly

Carbon based materials are commonly used for electrode assembly, aiming to maximize the surface area and enhance the conductivity, to facilitate mass transfer of reactants and therefore promote the eCO_2RR. Here we introduce three carbon materials employed in my study.

- Carbon Black

Carbon blacks have been widely applied into the various fields of electrochemistry due to their high mesoporous distribution, good electrical properties, low cost, and high availability[142]. They are widely used in eCO_2RR, aiming to facilitate the mass transfer of CO_2 and promote

the reduction reaction. Kusama *et al.*[143] studied the eCO_2RR in an aqueous media with crystalline Cu phthalocyanine supported on carbon black, and achieved highly selective and reactive eCO_2RR to C_2H_4 with FE of 25%.

- Graphene

Graphene is regarded as a promising 2D material with excellent electronic conductivity, good optical transmittance, large specific surface area, and superior chemical stability[144]. Therefore, fabrication of graphene based electrocatalyst has the potential to achieve high-property catalyst. Zhang *et al.* reported a Tin oxide nanoparticle supported on graphene in aqueous $NaHCO_3$ solutions and achieved the FE for formate production of >93% with high stability and current densities of >10 $mA \cdot cm^{-2}$.

- Graphene aerogel

Graphene aerogel, as a metamaterial, is suitable to be used as electrodes for electrochemical devices [145, 146]. GA's high conductivity [147] (Fig. 2.16a) and high porosity [148] (Fig. 2.16b and 2.16c) enable its applications for GDL, current collector and catalyst support. It can be made into any shape and highly compressible [149] (Fig. 2.16d). Therefore, it could be used as a simplified electrode host as the 'dry' electrode and improve the mass transport of eCO_2RR. GA has an excellent organic solvent absorbency [145-149]. Liu *et al.*[150] reported the feasibility of using GA in direct methanol fuel cells, because its high organic solvent absorbency allows the electrode to act as a 'fuel container', thus reducing methanol crossover effect while using high concentration methanol. In the eCO_2RR, GA can be inserted in the chamber, which allows CO_2 to diffuse within high porous GA rather than passing through the gas chamber. The high porosity from GA offers a large surface area and a considerably good conductivity ($\approx$10 S cm^{-1})[151], which make it a suitable alternative material as a catalyst substrate.

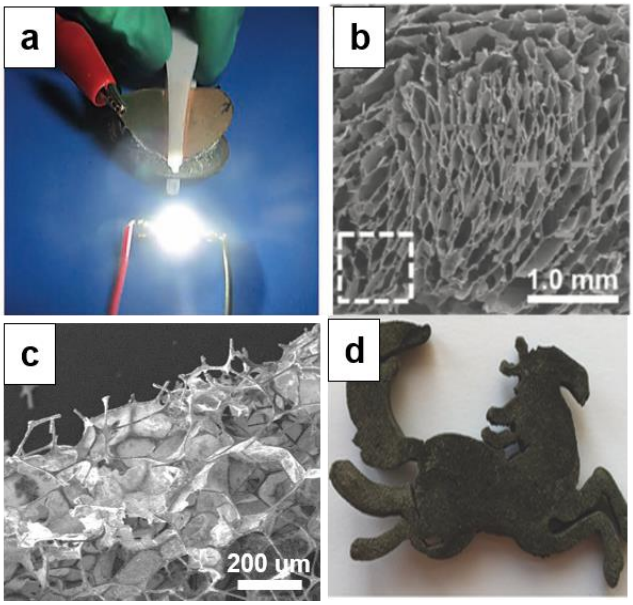

Figure 2.16 GA's a) electric conductivity; and SEM images of b) GA prepared using self-assembly method[152]; c) GAFC electrode prepared using melamine form template and d) super lightweight GA[153].

Chapter 3 Experimental

This chapter presents the detailed information about chemicals, catalyst synthesis technology, electrode fabrication, cell design technology, electrochemical methods used to test the catalyst, and characterization techniques.

3.1 Materials and Reagents

All materials and reagents involved this study, along with their suppliers are listed below in Table 3.1. Most of these were used in as-received forms, unless specially mentioned.

Table 3.1 List of the materials and reagents

Type	Chemical reagents / materials	Supplier
Gas	N_2	BOC
	CO_2	BOC
	H_2	Air Products
	CO	Air Products
	CH_4	Air Products
Organic solvents	Ethanol, absolute	Fisher Scientific
	Isopropanol	Fisher Scientific
	Acetone	Fisher Scientific
	Ethylene glycol	Fisher Scientific
	Nafion® 117 containing solution	Sigma-Aldrich
	Formic acid, formate	Liquid products
Metal precursor	Copper sulfate pentahydrate, 98%	Sigma-Aldrich
	Copper acetate, 98%	Sigma-Aldrich
	Pt on carbon black, nano-powder	Fisher Scientific
Carbon	Carbon black, Vulcan® XC72R	CABOT
	Graphene oxide, suspension	Goodfellow
	Graphene oxide, powder	Sigma-Aldrich
Reducing agent	L-ascorbic acid, 99%	Alfa Aesar
	Glucose, powder	Sigma-Aldrich
	Polyvinylpyrrolidone, wt. 10000, powder	Sigma-Aldrich
	Sodium hydroxide, pellets	Sigma-Aldrich
Surfactant	Sodium dodecyl sulfate (SDS)	Sigma-Aldrich

Electrolyte	Potassium hydroxide, 90%, flakes	Sigma-Aldrich
	Potassium hydrogen carbonate	Alfa Aesar
Commercial catalyst	Antimony tin oxide, nanoparticles	Sigma-Aldrich
	17-28 nm Indium tin oxide, nano powder	NanoTek
	Dendritic Cu powder	Sigma-Aldrich
	Cu_2O powder, 100nm	EPRUI Nanoparticles & Microspheres Co. Ltd.
Materials	Stainless steel	RS Components
	Silicone rubber sheet	Silex Ltd.
	Silicone tubing	Silex Ltd.
	Carbon paper, H23C6	Freudenberg
	Graphene aerogel	Gaoxi Technology Co., Ltd.
	Clear resin, FLGPCL04	Formlabs
	White resin, VeroWhite Plus fullcure 835	OBJET
Electrodes	Pt counter electrode	ALS Co. Ltd.
	Ag/AgCl reference electrode, RS-5B	BASI
	Reference electrode for alkaline electrode, RE-61AP	BASI
	Glassy carbon electrode	ALS Co. Ltd.
Proton exchange Membranes	Cation exchange membrane, FAB-PK-130	FuMA-Tech
	Nafion membrane 117	Chemours

3.2 Apparatus

3.2.1 Hot Plate and Heating Mantle

Hot plate and heating mantle are the apparatus for Cu based catalysts synthesis under an air/N_2 atmosphere, as schematically shown in Fig. 3.1, where the chemical reactions will occur.

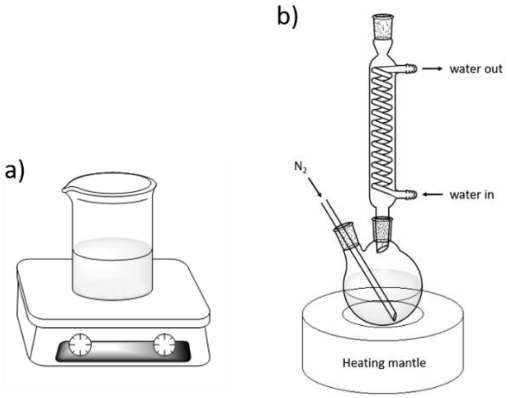

Figure 3.1 Schematic diagram of apparatus used for catalyst synthesis, a) open air reaction b) nitrogen purged reaction

3.2.2 Ultrasonic Bath

Ultrasonic bath is an effective method for the dispersion of solids and emulsification into liquids. The mixing of the reagents and the catalyst can generate fine particles/droplets in a very short time. By reducing the particle size, the total surface area of phases increases. For many materials, ultrasonic treatment can produce fine particles and droplets - often significantly below 100 nm, which is a practical method for nano-catalyst preparation[154].

3.2.3 Freeze Dryer

Freeze drying is a solvent removal process. It works by freezing (-90 $^{\circ}$C) the material and then leave it under vacuum, which allows the frozen solvent sublimated from the material and has advantages for structural integrity. The freeze drying occurs in three steps, including freezing, sublimation and adsorption[155]. In the freezing step, temperature is dropped below materials' triple point to ensure that sublimation rather than melting, where the sublimation will preserve its physical form. The second step is sublimation, in which the pressure is lowered, and heat is applied for sublimation of the sample. It is a slow process and about 95% of water in the sample is removed. In the final adsorption step, the temperature is increased above the second step, where ionically bounded water molecules are removed by breaking the bonds between the

material and the water molecules. After this process, the freeze-dried materials retain a porous structure, with 1-5% residual moisture. In my PhD study, a freeze dryer (Alpha 2-4 LDplus) was utilized for synthesis of porous graphene aerogel from graphene oxide.

3.2.4 Centrifuge

Centrifuge is a laboratory process that is commonly used for the separation of solid, liquid or gas, based on the density difference of components. It works by using the principle of sedimentation, where substances are separated according to the density difference under the influence of gravitational force. In my PhD study, it is applied for separation of the synthesized catalyst from the aqueous suspension.

3.2.5 Oven

Laboratory oven (drying oven) was applied for drying of materials under a fixed temperature in my PhD study.

3.3 Chemical Synthesis

3.3.1 Synthesis of Cu_2O Nanocrystal Electrocatalyst

As discussed in Chapter 2, Cu is a promising element with a potential to convert CO_2 to high value-added products. Cu_2O is one of the commonly used catalysts for eCO_2RR with good electrocatalytic properties and a simple synthesis method. Therefore, Cu_2O was chosen as one of the catalysts evaluated in my PhD study, and CO and formate were the target products.

Cu_2O nanoparticle catalyst was prepared using a hydrothermal method based on the following steps[156]. 200 mg of copper acetate (Sigma-Aldrich, 98%), 50 mg polyvinylpyrrolidone (Sigma-

Aldrich, wt. 10000) and 100 mL deionized water were added into a 250 mL beaker. Then the mixture was stirred and dissolved at a stirring rate of 400 rpm under the ambient condition. 200 mg NaOH (Sigma-Aldrich, 98%, in 20 mL deionized water) solution was added drop wisely into the mixture while stirring. A dark blue suspension was formed. Next, 150 mg L-ascorbic acid (Alfa Aesar, 99%, in 15 mL deionized water) solution was added into the beaker precisely. After 30 min, an orange colour suspension was obtained and the sample was collected using centrifuge. The sample was washed using ethanol (Fisher Scientific) and centrifuged again to remove any residual solvent. Then the sample was dried in laboratory oven before transferred into a glass vail.

3.3.2 Synthesis of Graphene Supported Cu oxide Electrocatalyst

Graphene supported Cu oxide (Cu_xO_y/Graphene) is another Cu based catalyst developed for eCO_2RR in this study. Cu_xO_y/Graphene is generally synthesized using polyol method in a reducing environment, where the polyol with metal precursors is suspended in a glycol solvent as surfactant, and the suspension is subsequently heated to a refluxing temperature (80 $^{\circ}$C-100 $^{\circ}$C). As shown in Fig. 3.1b, a condenser is attached on the top neck of flask, and the vapour is continuously cooled and produced back into liquid form in the condenser, which prevents the reagents from escaping. This technique is commonly used to synthesize metallic, oxide, and semiconductor nanoparticles[157].

In this study, the specific synthesis steps are listed as follows. 40 mg of graphene oxide powder (Sigma-Aldrich), 3 mL 0.1 g•mL^{-1} L-ascorbic acid (Alfa Aesar) and 10 mL ethanol (Fisher Scientific) were added into a 20 mL vial and sonicated under 75 $^{\circ}$C for 2 h. Then the suspension was moved into 250 mL three neck flask and 75 mL of ethylene glycol was added. 0.078 g (mol ratio C:Cu 2:1) $CuSO_4 \cdot 5H_2O$ (Sigma-Aldrich) was dissolved into 10 mL deionized water

and then added into the mixture drop wisely. The mixture was stirred at a speed of 400 rpm, under 70 - 95 °C for 2 h in N_2 (BOC). After reaction, the mixture was washed and centrifuged with ethanol to remove any residual solvent. Then the sample was dried in laboratory oven before transferred into a glass vail. Cu_xO_y/Graphene catalysts with various Cu contents were obtained based on the above processes.

3.3.3 Synthesis of Graphene Aerogel

Graphene aerogel was synthesized following a typical procedure[158]. 0.72 g L-ascorbic acid (Alfa Aesar) was added into a 200 mL beaker containing 60 mL of 4.0 mg•mL^{-1} graphene oxide aqueous solution (Goodfellow) within an ultrasonic bath for 2 hours under the ambient condition. Then the mixture was placed in oven at 40 °C and left for two days to form graphene hydrogel. The graphene hydrogel was taken out from the beaker and purified in distilled water for one week (replace new distilled water per day) and freeze dried at -65 °C for one day to remove the water. Then a graphene aerogel was obtained.

3.4 Techniques for Characterization

The techniques involved in this thesis are listed in Table 3.2.

Table 3.2 Techniques and applications in this thesis

Techniques	Applications
X-ray diffraction	Crystallographic structure and valence analysis of catalysts, crystalline structure and the metallic valence of catalyst can greatly affect the selectivity of reduced product
Scanning Electron Microscope	Analysis of the microstructure morphology and particle size of catalysts, the surface/volume ratio is corresponding to catalysis active sites
Energy Dispersive Spectroscopy	Qualitative analysis of the elements in the materials, to determine the identity of observed particles

Drop Shape Analysis	Hydrophobicity analysis of electrodes, the hydrophobicity can affect the durability of reaction system

3.4.1 X-ray Diffraction (XRD)

XRD is one of the most important techniques in the study of catalysts and it can determine the crystal phase and the size of crystallites existed in analytes[159].

The principle of X-ray diffraction is based on the characteristic property of waves which can interfere with the other waves. This means an increased wave amplitude can be achieved when their displacements are added, which is called 'constructive interference'. Whereas a reduced amplitude is obtained when their displacements are subtracted, called 'destructive interference', as shown in Fig. 3.2a.

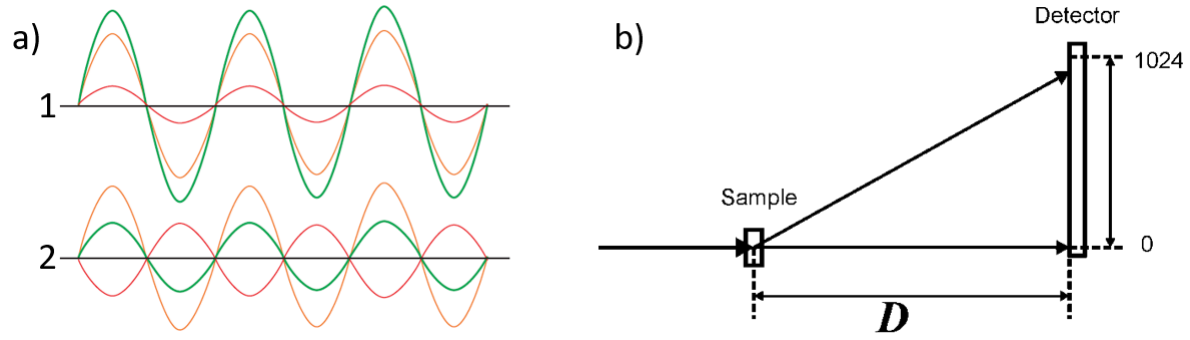

Figure 3.2 a) Interfere of two waves (red lines), line 1: constructively, enhanced amplitude, line 2: destructively, reduced amplitude[160], b) a schematic illustration of XRD

The intensity of electromagnetic radiation is proportional to the square of the amplitude of the waves, thus the region of constructive and destructive interferences presents as the region of enhanced and diminished intensities. The diffraction phenomenon is the interference caused by existing objects in the wave path, and the resulted pattern of varying intensity is called diffraction pattern. Once the diffracting objects are comparable to the radiation wavelength, the diffraction occurs[160]. X-rays are electromagnetic radiations [161, 162], and it is comparable to

bond length in molecules and the spacing atom in crystals, so it can be used to diffract the patterns.

On an X-ray diffraction instrument, sample and detector are placed with a distance of D as shown from the sketch in Fig. 3.2b. Incident X-rays pass through the sample and then refringence phenomenon happens. The propagation direction is changed, with an angle (2 theta). In this case, only if the angles of incident rays obey the Bragg's law, the diffraction phenomena could happen. Here, the Bragg Equation can be used for calculating the reflection of X-rays from two planes of atoms in crystals.

$$n\lambda = 2dsin\theta \qquad \text{Eq. 3.1}$$

where n (integer) is diffraction order, λ is incident X-ray wavelength, d is d-spacing (inter-plane distance) and θ is incident angle.

In eCO_2RR, the XRD results were captured using Siemens D5000 (Bragg–Brentano θ-2θ configuration), equipped with a Cu X-ray tube (Cu-K_α, λ=0.154) for the crystal structure. The results will be used to investigate the microstructures of the electrocatalyst. It is a functional tool for crystalline catalysts characterization. For the testing, an incident beam of X-rays filtered by a nickel filter was used, then the samples were placed on a plastic sample holder in the diffractometer. The samples were scanned from $10^o < 2\theta < 90^o$ and operated at 40 kV and 40 mA. Finally, the recorded patterns were analysed using the Jade software.

3.4.2 Scanning Electron Microscope with Energy Dispersive Spectroscopy (SEM/EDS)

The SEM is a functional instrument for analysis of the microstructure morphology and particle size of chemical compositions. The principle of the SEM is schematically illustrated in Fig. 3.3. A narrow beam of electrons is accelerated by an electron gun, and then passes through the electron lenses. It is finally brought to a focus on the surface of the specimen stage, then is scanned across the sample surface like a television raster. The generated secondary electrons by the interaction of the probe with the sample is collected, amplified and displayed on a monitor. The electron energy of the beam used in scanning electron microscopy is usually of the order of 5-30 keV[163]. EDS is commonly used for qualitative analysis of the elements in the materials. Typically, SEM is equipped with an EDS system for elemental analysis. It can detect the elements with the concentrations ranging from 1-10 wt%. This can be indicated in elemental mapping images, which is practical to determine the identity of particles observed in SEM image[164].

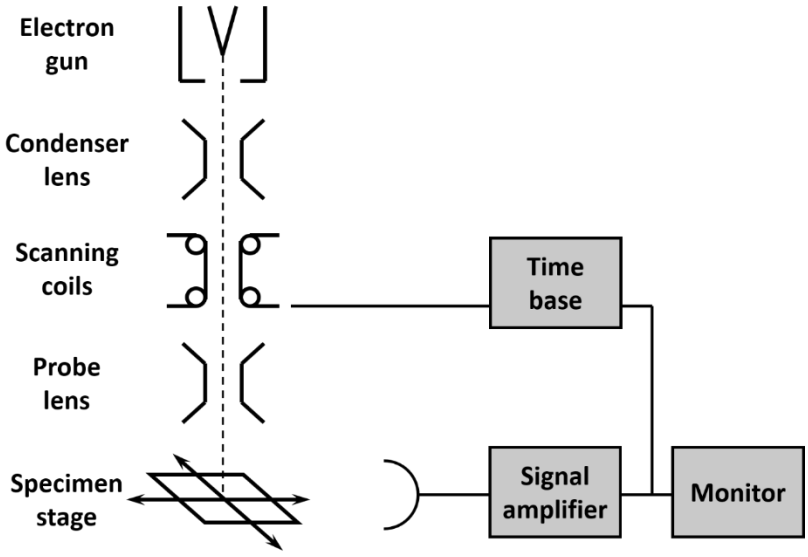

Figure 3.3 Schematic of the principle of SEM

In this study, an SEM/EDX (MIRA 3, TESCAN) was employed for the study of catalysts, gas diffusion layer (GDL) and assembled electrodes, and helped to analysis the morphology of electrocatalysts, surface and cross-section of assembled working electrodes.

3.4.3 Hydrophobicity Analysis by Drop Shape Analysis (DSA)

DSA is a powerful image-analysing method used for the characterisation of interfacial properties (contact angle, hydrophobicity) from the shape of drops[165]. Basically, the shape of a liquid drop is influenced by surface tension and gravity effects. Surface tension tends to make the drop spherical and the gravity tends to elongate a pendant drop or flatten a sessile drop. When the gravitational energy and surface tension is balanced, the surface tension can be determined from the analysis of the shape of the drop. In my PhD study, DSA was employed to measure the hydrophobic properties of self-designed gas diffusion layer by analysing the contact angle. As shown in Fig. 3.4, the contact angle is given by measuring the contact angle between calculated drop shape and sample surface. Larger contact angle means more hydrophobic properties of the sample surface.

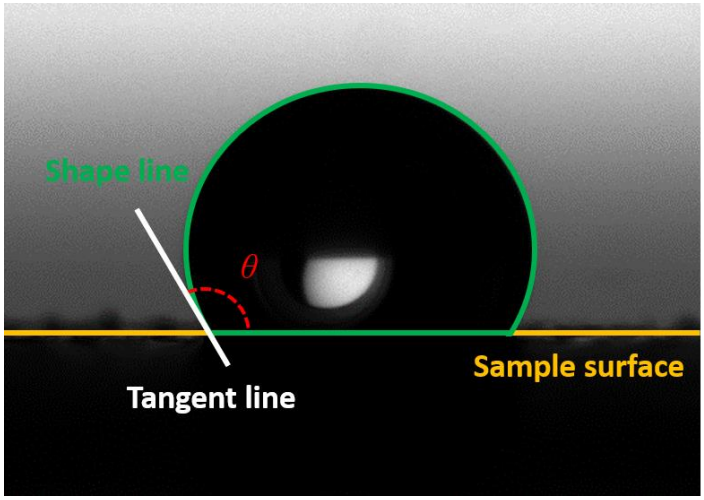

Figure 3.4 Measurement of contact angle by DSA

3.5 Techniques for Product Analysis

3.5.1 Gas Chromatography (GC)

GC is one of the most useful method for quantification of organic compounds that can be vaporized without decomposition[166]. It is commonly used for quantification of the gaseous and alcoholic liquid species[167, 168]. A gas chromatography (Shimazu Tracera GC-2010) was employed for this research.

For gaseous product analysis, a gas sampling bag is employed to collect the outlet gas for analysing the gaseous products by a GC. Then the collected outlet gases are injected into the chromatographic column and transported through the column by the flow of an inert, gaseous mobile phase (e.g. helium with Grade CP N5.0, 99.999%). The column contains a liquid or polymer stationary phase which is adsorbed onto the surface of an inert solid[166]. Then these chemical constituents pass through the column and are separated with different elution orders and retention times. At the end of column, a detector will record the process and a time – intensity plot will be obtained. For quantitative analysis, the amount of the species can be calculated by analysing the integral area of each chromatography peak. Fig. 3.5 presents a schematic illustration of GC.

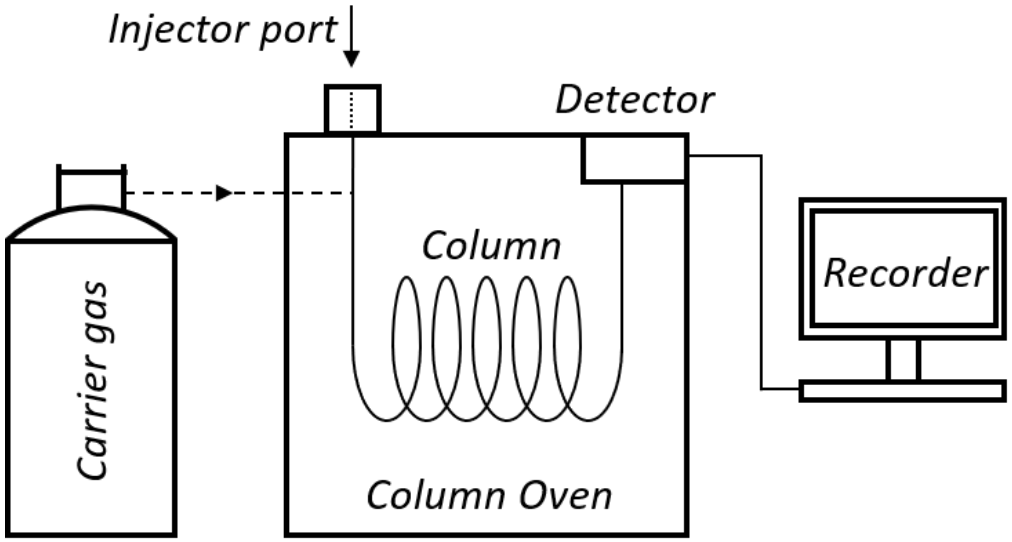

Figure 3.5 Schematic of a GC apparatus[169]

In GC apparatus, a proper detector is required for detection of eCO_2RR products. Thermal conductivity detector (TCD) and flame ionization detector (FID) are two mainly used detectors in GC. TCD can be used to detect both organic and inorganic compounds, and the detection method is based on changes of the thermal conductivity of the column effluent when another compound is present. FID is more sensitive than TCD and can be used for analysing low concentrations of CO and hydrocarbons. The sample will pass through a hydrogen flame and the produced ions will be measured by burning the sample. The shortage of each detector is obvious. The TCD is lack of a sensitivity whereas the TCD cannot detect the concentration of H_2, which is related to the side-reaction (hydrogen evolution reaction) commonly existed in eCO_2RR.

In this research, a barrier discharge ionization (BID) detector was used to analyse the gas products. For product detection, He plasma are generated by applying a high voltage to a quartz dielectric chamber, then the eluted compounds are ionized by He plasma and captured by the collection electrodes, revealing by the generation of peaks. In analysis of mixtures of inorganic

and organic compounds, the BID can detect component at the ppm level. Compared with TCD and FID, it has over 2 folds higher sensitivity than FID and over 100 folds than TCD.

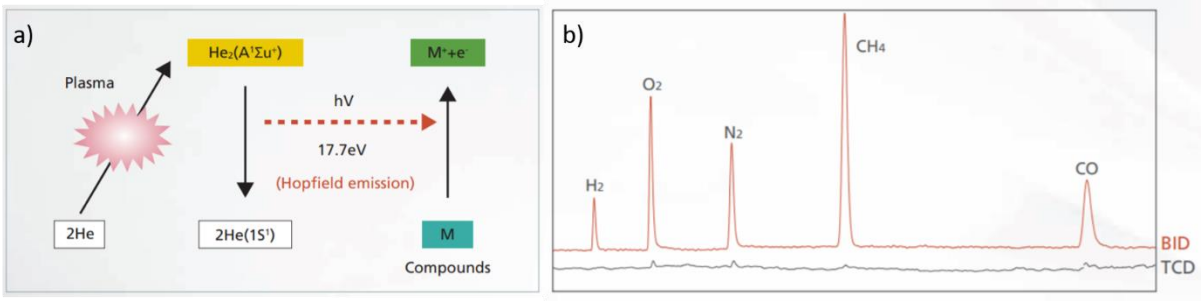

Figure 3.6 a) Principal of ionization reaction b) schematic of GC plot, 10 ppm concentration of each species in He[170]

For the column used in this research, ShinCarbon ST micropacked column 80/100 (Restek) was applied to quantitatively analyse the permanent gases and light hydrocarbon products.

The area of the detected signal depends on the product being analysed which is proportional to the gaseous concentration. For quantitively analyse, internal standard method is applied using a standard mixture gas (BOC), which contains H_2 (1.000%), CO (1.000%), CH_4 (0.500%), CO_2 (96.000%), C_2H_4 (0.500%), C_2H_6 (0.500%), and C_3H_6 (0.500%). Finally, FE for each component can be calculated using the following equation:

$$FE = \frac{\alpha \cdot n \cdot F}{Q} \qquad \text{Eq. 3.2}$$

where α is number of transferred electrons per mole of reactant (e.g., α = 2 for reduction of CO_2 to HCOOH), n is molar mass of the product, F is the Faraday's constant (96485 C mol^{-1}) and Q is the overall applied charge. The detailed calculation steps are shown in Appendix 1.

3.5.2 Ion Chromatography (IC)

IC is a type of liquid chromatography employed to separate the ions from aqueous solutions, which is based on their affinity to different types of ion exchanger. This method can be applied to analyse most of the charged molecules[124].

The schematic set-up and process of IC test are shown in Fig 3.7. The samples are injected and carried by the eluent flow to ion exchange column, and then interacted with fixed ions of opposite charges. Then the ions' flows are slowed down to an extent characteristic of each ion. Next, the ions reach to the suppressor separately, and the suppressor exchanges all the cations for hydrogen ions before they reach the detector in order to reduce background noise and increase the sensitivity for the analytes. The detector measures the electrolytic conductivity and sends signals to the data acquisition system[171].

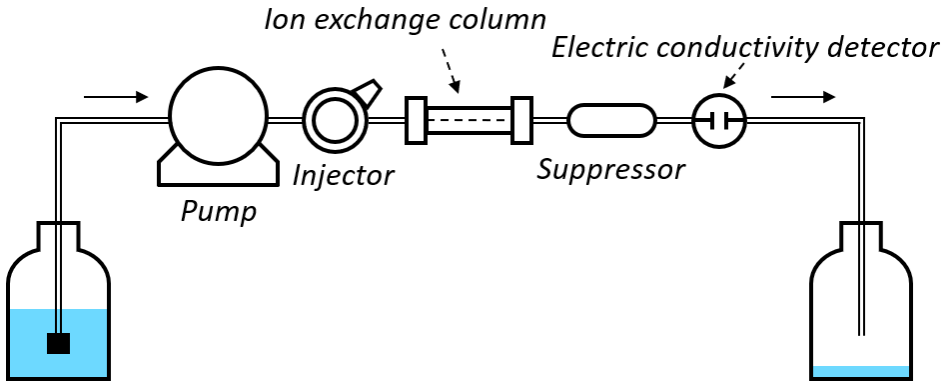

Figure 3.7 Schematic of an IC apparatus

For applications of eCO_2RR in this research, an ion chromatography (Eco IC, Metrohm) equipped with the "METROHM 6.1005.200" column was employed for quantifying of formate and formic acid.

3.6 Electrochemical Evaluation

3.6.1 Electrochemical Instruments and Apparatus

The electrochemical evaluation was performed in commercial half-cells and homemade 3D-printed cells, including H-cell and GDE type cell, which will be explained in more details in Section 3.7. All the electrochemical reactions and measurements were performed using the Autolab potentiostat/galvanostat (Metrohm Autolab PGSTAT128N). Cyclic voltammetry (CV) and chronoamperometry (CA) were carried out for electrochemical evaluations.

In this project, Ag/AgCl (RS-5B, BASI, 3M NaCl, 0.197V vs. SHE) and alkaline reference electrode (ARE, RE-61AP, BASI, 0.117V vs. SHE) were used in a three electrode system and the potential value was converted to RHE using Eq. 3.3 and 3.4. All the potentials stated in this project have been converted to RHE. KOH, $KHCO_3$ with different concentration solution were applied as catholyte, and 1 M $KHCO_3$ and 5 M KOH solutions were used for anolyte.

$$E_{RHE} = E_{Ag/AgCl} + 0.197V + 0.0591V \times pH \quad \text{Eq. 3.3}$$

$$E_{RHE} = E_{ARE} + 0.117V + 0.0591V \times pH \quad \text{Eq. 3.4}$$

Three types of ion exchange membrane (IEM) were introduced in cells assembly initially. Nafion® membrane can only allow proton transfer through the membrane, which limits the current of the overall reaction. Anion exchange membrane can allow all anions to transfer through the membrane, where the organic anions (e.g. $HCOO^-$) could transfer from cathode chamber to anode chamber, and it will influence the tests of liquid products. Among them, cation exchange membrane (CEM, FAB-PK-130, FuMA-Tech, 11.3 mS cm^{-1}) could allow cations to transfer through the membrane (including protons and metal cations of electrolyte),

and this could maximum the current of the reaction system. Therefore it was employed as ion exchange membrane (IEM) in this study.

3.6.2 Cyclic Voltammetry (CV)

CV is the most widely used electrochemical analysis methods, which is employed for initial investigation of electrocatalyst, identification of potentials, thermodynamic and kinetics of redox processes of electroactive species. Normally, the current is measured with a potential sweep from an initial potential (E_i, where have no reaction, thus it is expected that the system has not been affected) to a chosen potential (E_s, which is relevant to the sample be investigated). The potential is swept from E_i towards to a positive or negative direction (depending upon the nature of the species under examination, normally, eCO_2RR towards negative direction). It is then increased above the standard potential (E^0) of redox couples studied, finally reaches to E_s. Once E_s is reached, the sweep direction is reversed back to E_i, with reverse reaction taking place in current response. A schematic of CV is show in Fig. 3.8a.

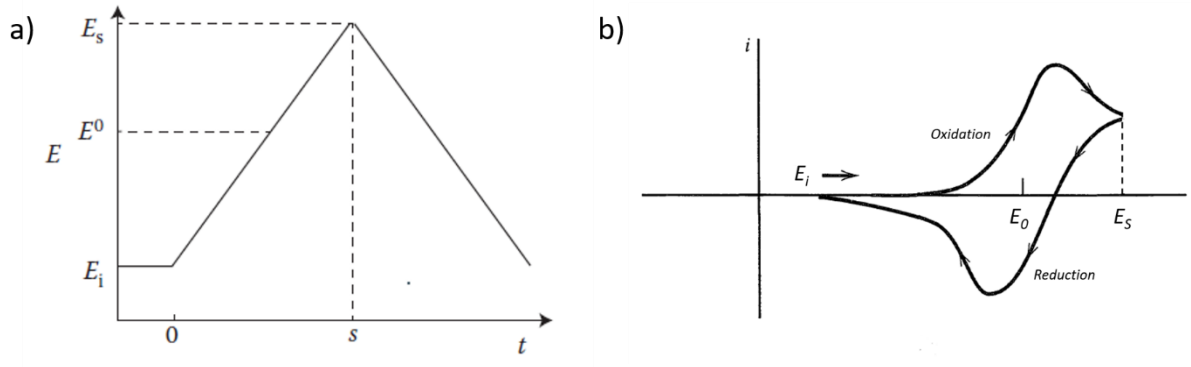

Figure 3.8 a) Potential scan vs. time for CV[124, 172], b) reversible cyclic voltammogram, where arrows indicate the potential sweep direction[172].

Fig. 3.8b shows the typical reversible cyclic voltammogram. CV is a linear-sweep voltammetry (LSV) with the scan continued in the reverse direction at the end of the first scan, and this cycle can be repeated several times. The potential is scanned linearly vs. time and it is swept from an initial potential (E_i) to the final potential (E_s) at a certain potential scan rate (generally 5-100

$mV•s^{-1}$.). Current response can be observed during the potential sweep and it is dependent on the charge transfer processes taken place at the surface of the working electrode. In eCO_2RR, this method can be applied before eCO_2RR test to confirm the reaction onset potential, and also help to determine the redox behaviour of electrocatalyst.

3.6.3 Chronoamperometry (CA)

CA is a time-dependent electrochemical technique used to examine the electrochemical activity and stability of the electrocatalysts. The constant potential is applied to the working electrode, and the current is measured as a function of time. Fig. 3.9 shows a typical CA scan plot, where an initial potential E_i is applied to minimal the current flows without any reaction. Then the potential is increased to a set potential E_s, where the electrochemical reaction happens.

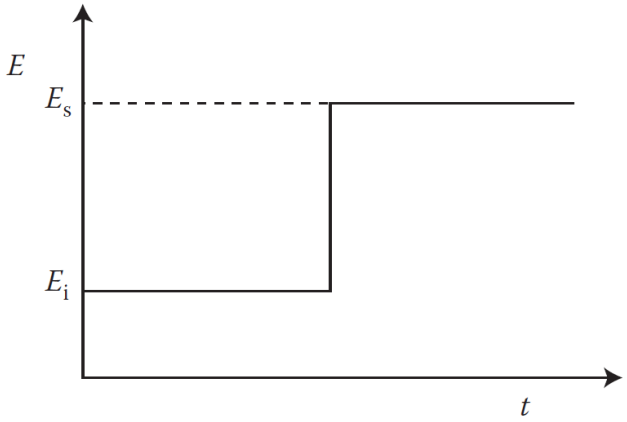

Figure 3.9 Potential scheme for CA[172]

In eCO_2RR, CA provides enough time for the charging of the double layer near electrode surface[172], and can be used for driving electrochemical reactions and collection of the products. Meanwhile, the difference between the E_s and E^0 is known as overpotential, which provides the information of extra input energy to drive the reaction. By providing the input charge and processing time of the electrochemical process in CA, the FE of the electrochemical reaction

can be obtained, if combined with the gaseous/liquid products measurement and molar mass calculation.

3.7 Electrochemical Cell Setup

In eCO_2RR, cell design is a crucial part which influences the overall efficiency of the system. The eCO_2RR is usually performed using a conventional H-cell [173-175] with a working electrode made by porous materials, e.g. carbon paper[176] and metal mesh[132]. Recent advancement in electrode design has used the GDE to enhance the mass transfer in eCO_2RR, where the GDE is widely used in proton-exchange membrane fuel cells. In the GDE configuration, the gas diffusion in porous media could lead to CO_2 retention within the electrodes with extended saturation on the catalyst bed. Therefore, this enables a desired mass transport of CO_2 to limit hydrogen evolution and improve reaction rate of eCO_2RR for higher FE and selectivity.

In this project, different types of cells were employed, including commercial cells and homemade 3D-printing cells, in order to optimize the mass transfer influence on eCO_2RR process.

- Half-Cell

A commercial three-electrode glass half-cell (CH Instruments, Inc.) was utilized in early stage, with one example shown in Fig. 3.10. The catalyst was loaded on glass carbon in a rotating disk assembled as the working electrode. Platinum wire and Ag/AgCl were used as counter electrode and reference electrode, respectively. All electrodes were injected into the glass cell for electrochemical evaluation.

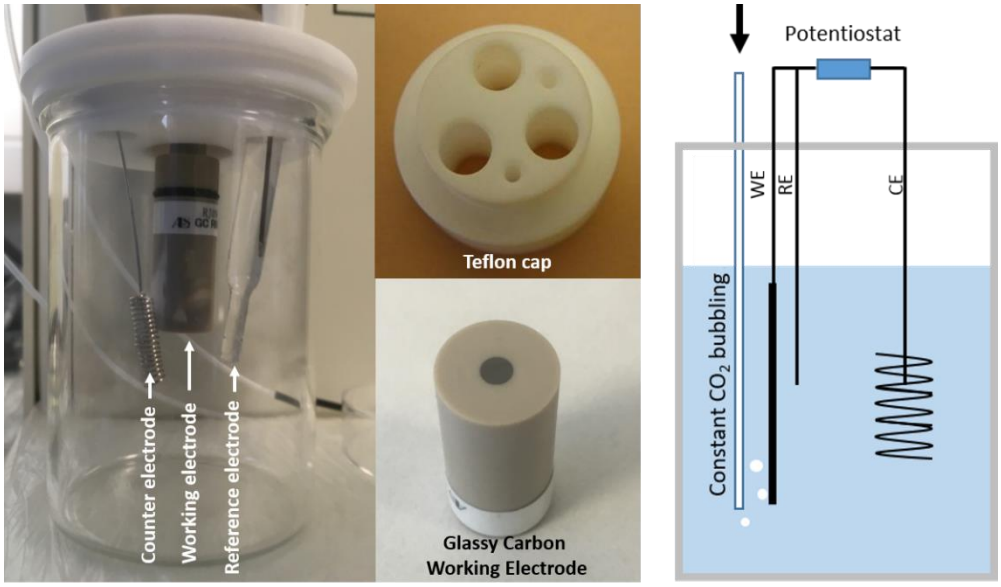

Figure 3.10 Commercial glass cell assembly, WE (working electrode), RE (reference electrode), CE (counter electrode)

- H-cell

Compact H-cell: A compact H-cell was designed by SOLIDWORKS® (details of 3D design and printing shown in Section 3.10) for eCO_2RR. Comparing with conventional H-cell[175], this compact H-cell presents an improved optimization by suppling more areas for the working electrode but less spaces between cathode and anode (ca. 1 cm), which will result in lower electrolyte resistance (causes overpotential) for electro-chemical behaviour[177]. Fig. 3.11c shows the construction of working electrode, where the catalyst is coated on gas diffusion layer, and then assembled with titanium (Ti) wire using a conductive resin. The reference electrode and counter electrode are injected in cathode chamber and anode chamber, respectively.

However, this type of gas supply will inevitably cause poor CO_2 transfer caused by the low solubility of CO_2 in electrolyte[178], while HER will also happen and reduce the CO_2 reduction efficiency[179]. Meanwhile, CO_2 supplying method based on the idea of 'bubbling into electrolyte' will be likely to occur to destabilize the system, where some CO_2 bubbles will stick on the surface of working electrode and block the pathway of proton transportation to the catalyst

surface. These will cause less electrode areas for reactions, thus leading to a significantly reduced current density.

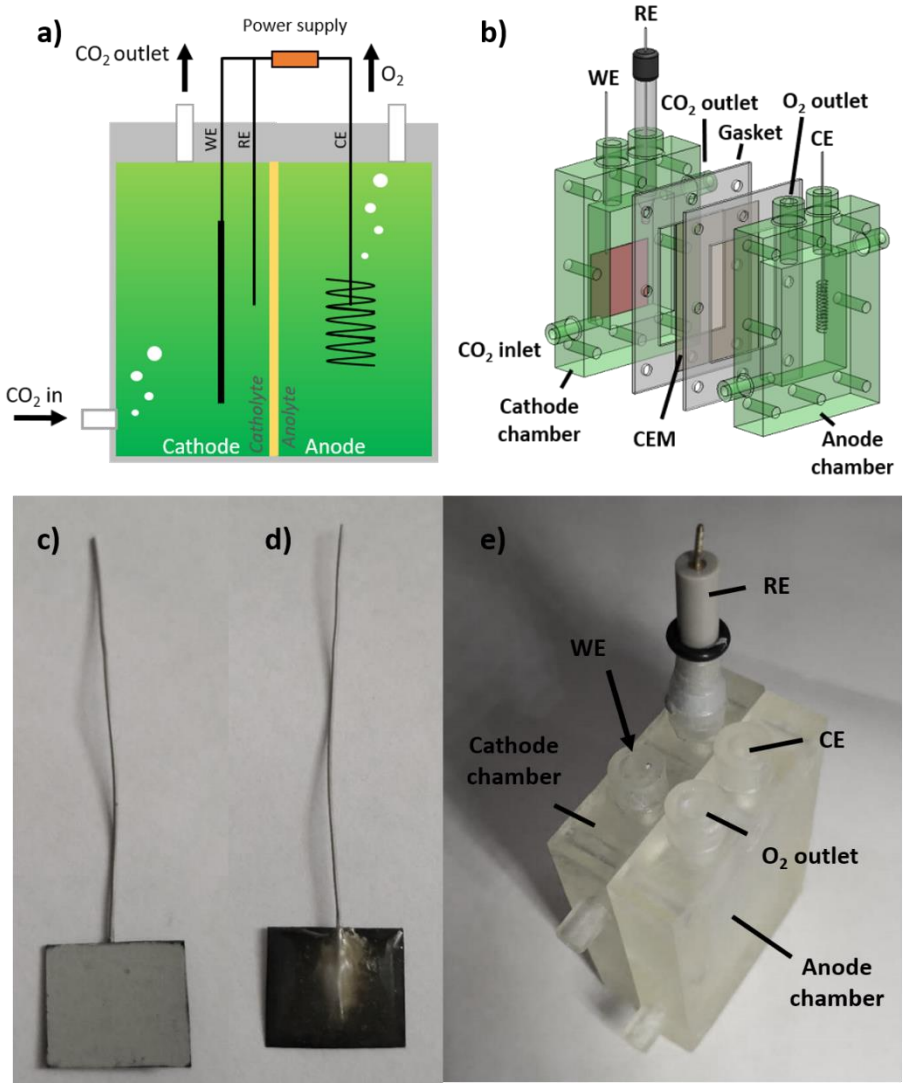

Figure 3.11 a) Schematic of H-cell, b) multi-components, working electrode c) front-view, carbon paper coated with catalyst d) back view, connect with conductive resin and epoxy resin, e) H-cell assembly

4-part H-type cell (4p-cell): 4p-cell was designed in an early stage which consists of 4 individual printed cell parts with two chambers. The catalyst coated carbon paper was compressed with current collector as the working electrode, and the reference electrode was injected in cathode chamber from the top. Pt coated carbon paper was compressed with current collector as counter electrode. A Nafion® membrane was placed between the anode and cathode chambers to allow H^+ to pass through.

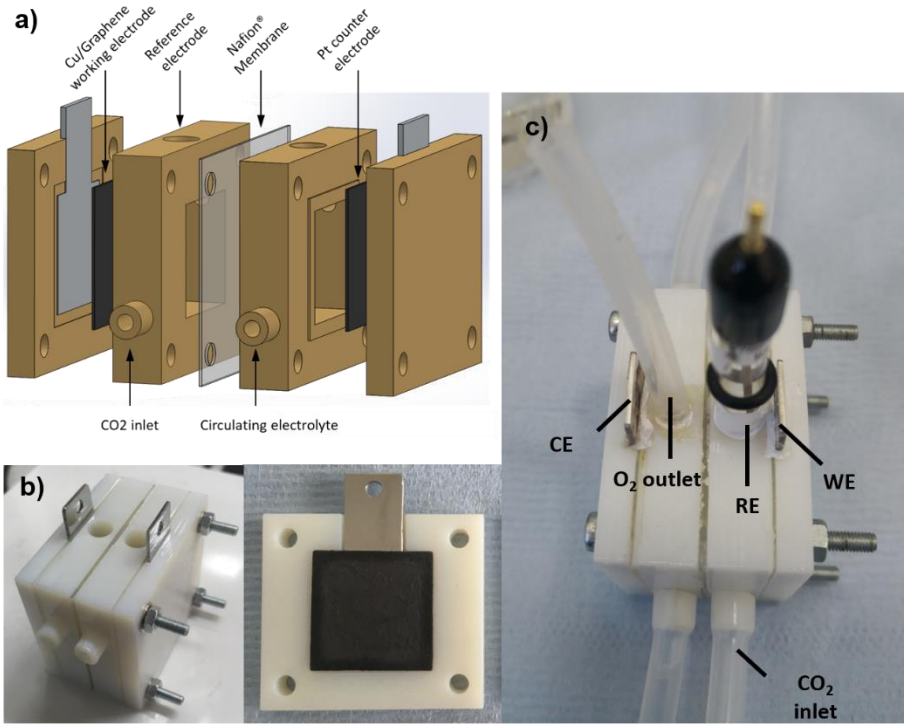

Figure 3.12 a) Multi-components of 4p-cell, b & c) 4p-cell assembly

- GDE cells

A construction concept was borrowed from PEMFC and named as GDE cell, in which CO_2 can be directly diffused from a gas phase to catalyst surface. A traditional GDE is made from porous carbon paper coated with catalyst layer as shown in Fig 3.13a. An advanced graphene aerogel assisted GDE was used in this work to study mass transfer influence on the overall cell performance. Based on these, three GDE cells with different electrode assembly were designed (Fig. 3.13).

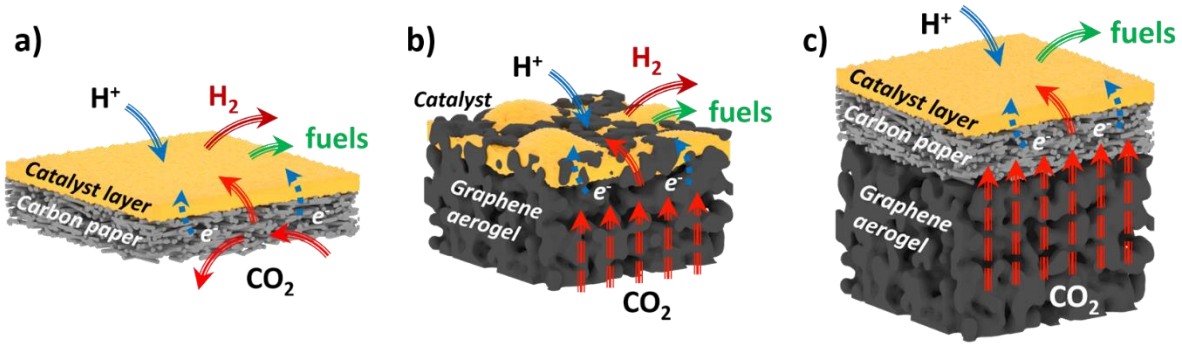

Figure 3.13 Electrodes design in GDE cells

Carbon paper GDE cell (CP-cell):

Conventional carbon paper GDL was served as the current collector and physical substrate for catalyst called CP-cell. Here the cathode chamber was divided into gas chamber and catholyte chamber. A hydrophobic carbon paper (Freudenberg H23C6) was used to separate the gas-liquid phases and served as working electrode. Reference electrode was immersed in catholyte and counter electrode in anode chamber. However, the structure of carbon paper was decayed after a long-term reaction, and the permeation of water easily happened in this type of cell to trigger HER as well as the blockage of CO_2 transport pathway. Additionally, an inhomogeneous CO_2 gas flow was often observed in carbon paper base GDE design.

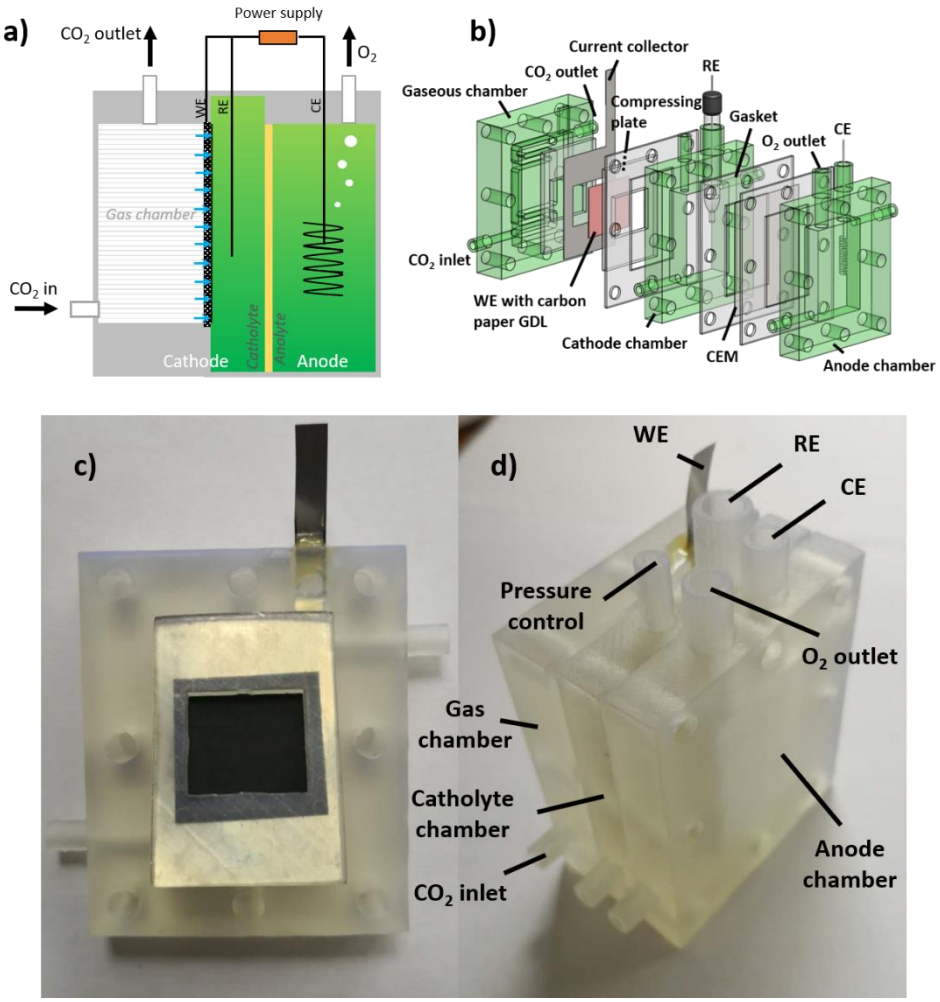

Figure 3.14 a) Schematic of CP-cell, b) multi-components, c) carbon paper based working electrode assembly, d) CP-cell assembly

Graphene aerogel GDE cell (GA-cell):

Graphene aerogel (GA, Gaoxi Technology Co., Ltd.) was inserted in the chamber and allowed CO_2 to diffuse within high porous GA rather than passing through the empty chamber. The high porosity from GA offers a large surface area and a considerably good conductivity ($\approx$10 S cm^{-1})[151], which make it a suitable alternative material as a catalyst substrate. Moreover, the 3D structure of GA could resist the permeation of electrolyte effectively. However, the high roughness on GA's surface could be problematic during the coating process for catalyst, even at a higher loading of 5 mg•cm^{-2} or after surface treatment. This leads to the formation of a coarse structure by exposing GA to the electrolyte. In this study, the GA was fully filled in the

gas chamber supported with catalyst. The working electrode and reference electrode were immersed in catholyte and counter electrode in anode chamber, respectively.

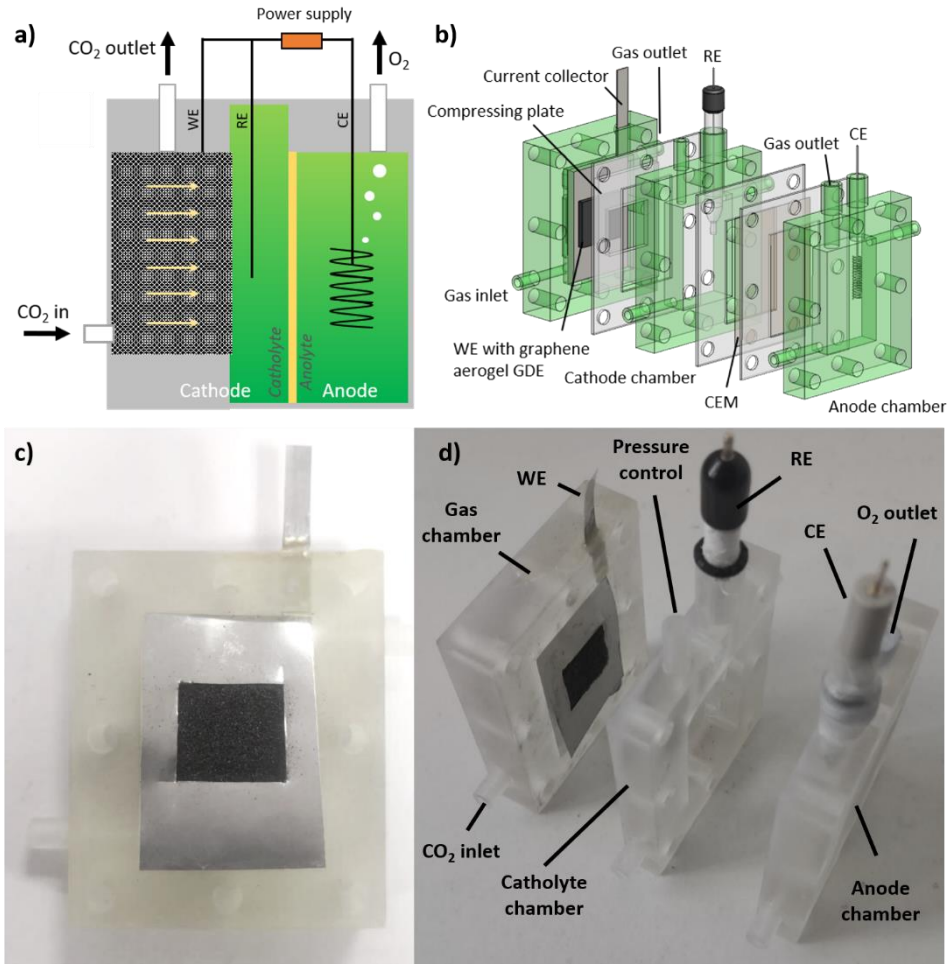

Figure 3.15 a) Schematic of GA-cell, b) multi-components, c) GA based working electrode assembly, d) GA-cell assembly

Hybrid graphene aerogel carbon paper GDE cell (GACP-cell):

The GACP cell was designed based on CP-cell and GA-cell. This design overcomes the drawbacks of those two cells. It consists of three chambers. The gas chamber in the left-hand side contains GA, where the CO_2 flows into the gas chamber and diffuses through GA and then CP, and finally reaches to the catalyst layer. The middle chamber is filled with catholyte, where the cathode coated with catalyst is exposed to the catholyte, and a reference electrode is inserted in this chamber. The right chamber is the anode chamber with anolyte and the inserted counter

electrode (Pt wire). A cation exchange membrane is placed between the anode and cathode chambers to allow the cations to pass through.

All the components with gaskets were firmly connected and sealed to ensure a good contact without any leakage**.** The whole cell was designed to reduce the electrolyte resistance.

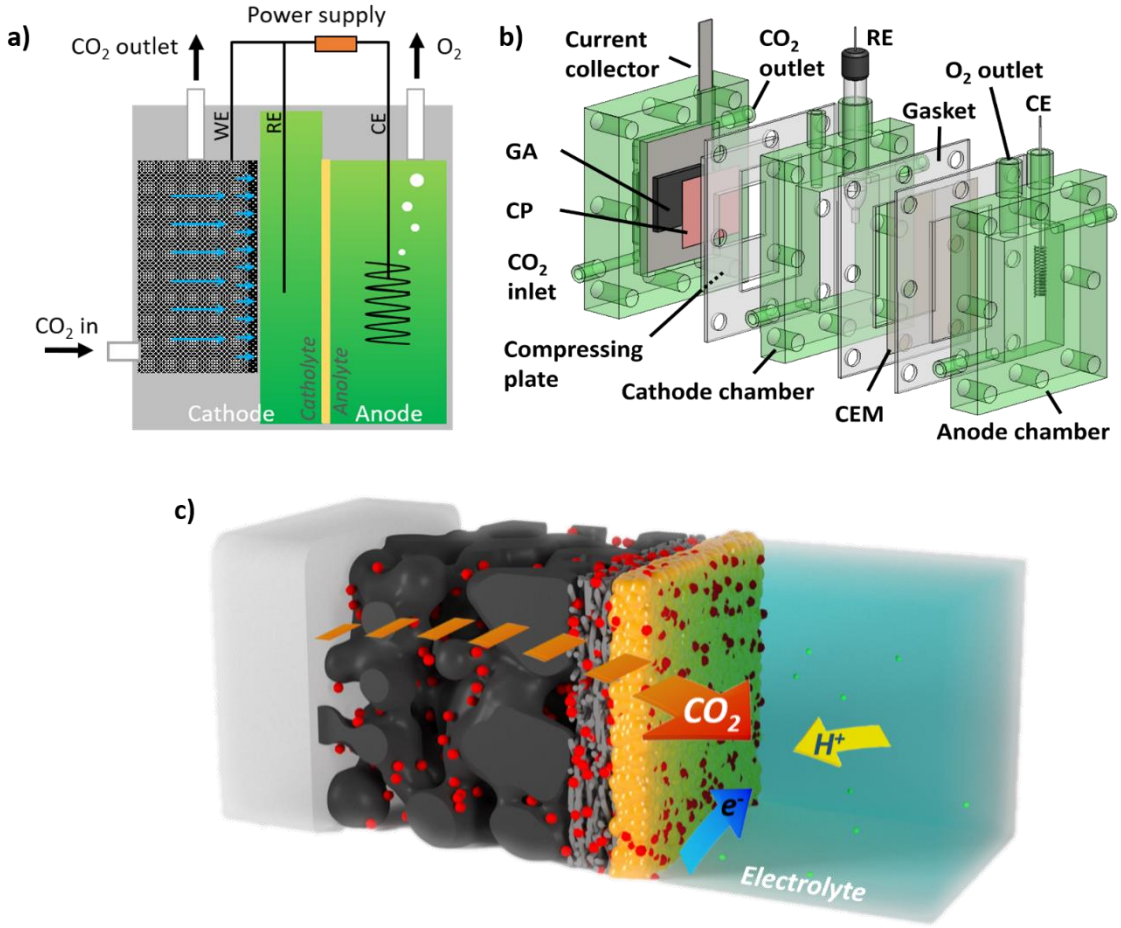

Figure 3.16 a) Schematic of GACP-cell, b) multi-components, c) CO_2 mass transfer pathway, CO_2 transfer through GA (black), CP (grey) and catalyst layer (yellow)

- Polymer electrolyte membrane compact flow cells (PEM-cell)

PEM-cell with large electrode surface area vs. electrolyte volume could reduce the transfer distance of reactants and help to reduce the internal resistance. Besides, a higher CO_2 concentration at the catalyst surface and lower liquid products in catholyte will promote the eCO_2RR[62, 90]. Fig. 3.17 shows the design and printed PEM-cells.

Compact PEM flow cell (absence of reference electrode):

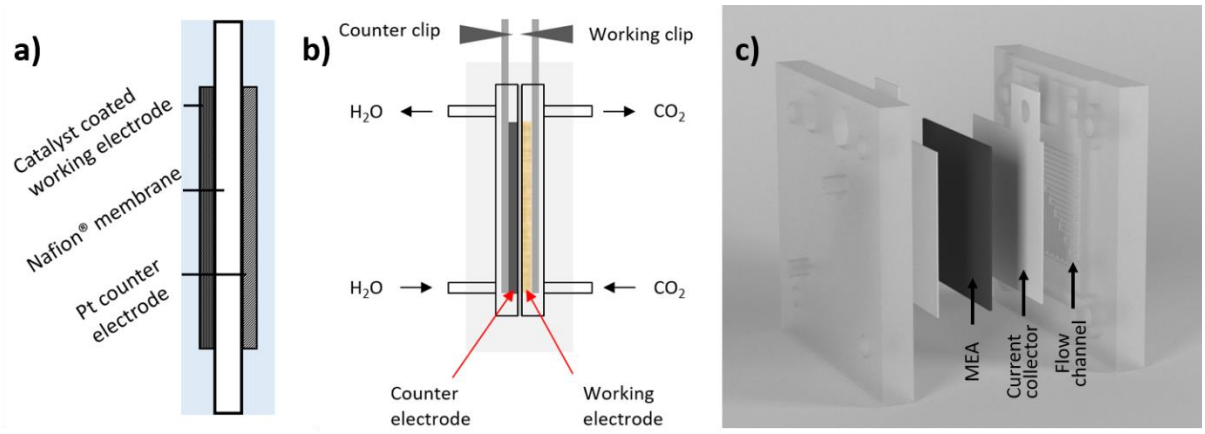

Figure 3.17 a) Schematic of membrane electrode assembly (MEA) b) structure of compact PEM flow cell c) multi-components

Compact PEM flow cell (+ reference electrode):

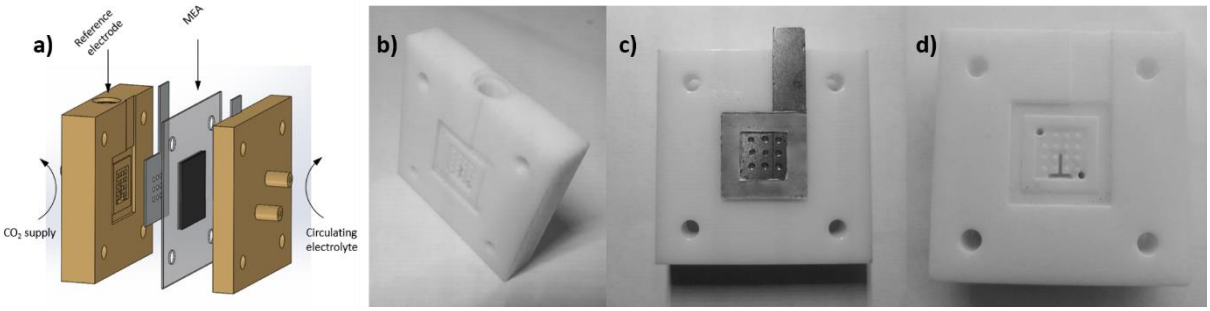

Figure 3.18 a) Multi-components of PEM flow cell (with reference electrode) b) counter half-cell c) current collector d) flow channel

3.8 Electrode Assembly

3.8.1 Catalysts Ink Preparation

- Ink for brush painting

20 mg of the specified catalyst powders were mixed with 200 µL – 1 mL ethanol/isopropanol (Fisher Scientific) in a 2 mL sample tube and then sonicated for 10 min. 40 µL Nafion® solution (5 wt.%, Sigma-Aldrich) was added into the tube and the ink was sonicated for 1 h.

- Ink for spraying and dropping

40 mg of catalyst (or 16 mg catalyst + 4 mg carbon black) was mixed with 2 mL ethanol/isopropanol (Fisher Scientific) and 1 mL deionized water into 5 mL sample tube and sonicated for 10 min. Then 80 μL Nafion® solution (5 wt.%, Sigma-Aldrich) was added into the tube and the ink was sonicated for 1 h. Typically, the ink for spraying and dropping has been diluted thoroughly than the ink for painting, because of the significant organic solvent vaporisation during spraying treatment.

3.8.2 Electrode Preparation

Loading catalysts onto the GDL as a working electrode is one of the important processes in electrode assembly. Here we used polytetrafluoroethylene (PTFE) and single-side treated carbon paper as the GDL to support the electrocatalyst.

- Electrode in half cell

In half cell testing, the catalyst was supported on a rotating disk electrode made from glassy carbon (ALS Co. Ltd.). The preparation method is explained as follows. 40 μL of as-prepared ink was dropped onto the glassy carbon, which was placed in the fume hood for 5 min under the ambient condition. Once the ink was dried, and a smooth layer was covered on the whole GC area, and then the electrode was ready to use.

- Catalyst – GDL assembly

For carbon paper based GDL electrode, the as-prepared ink (for painting) was sonicated for 30 min, then it was brush-painted onto the carbon paper (H23C6, Freudenberg) layer by layer with an effective surface area of 2 cm^2. It was dried at 50 °C for ~2 min after each layer was printed. the process was repeated until the mass increase (Δm) is 5 $mg \cdot cm^{-2}$. For GA based GDL electrode, the as-prepared ink (for spraying) was sonicated for 30 min and then transferred into the ink cup of spray gun (Evolution AL plus, Harder & Steenbeck). Then it was feed by N_2 gas at about 30 psi and sprayed onto the graphene aerogel layer by layer, within an effective surface

area of 2 cm^2. Drying (50 °C, ca. 30 s) was applied between each layer. The painting – drying processes were repeated until mass increase Δm is about 5 $mg•cm^{-2}$.

- Electrode – Current collector assembly for traditional H-cell

In H-cell, the working electrode was immersed in catholyte, which was consisted of a carbon paper supported catalyst layer clumped on a conductive wire (titanium wire), as demonstrated in Fig 3.19. Fig. 3.19a shows a schematic illustration of the working electrode, where the as-prepared ink was painted on a carbon paper (catalyst layer surface area = 2 cm^2, Fig 3.19c) to reach a loading rate of 5 $mg•cm^{-2}$, then a titanium wire was attached to the back of the carbon paper using conductive epoxy resin. Finally, epoxy resin was fully covered the conductive resin to insulate the back of the electrode from the catholyte (Fig. 3.19b). The electrode assembled in a cell is shown in Figs. 3.19d and 3.19e.

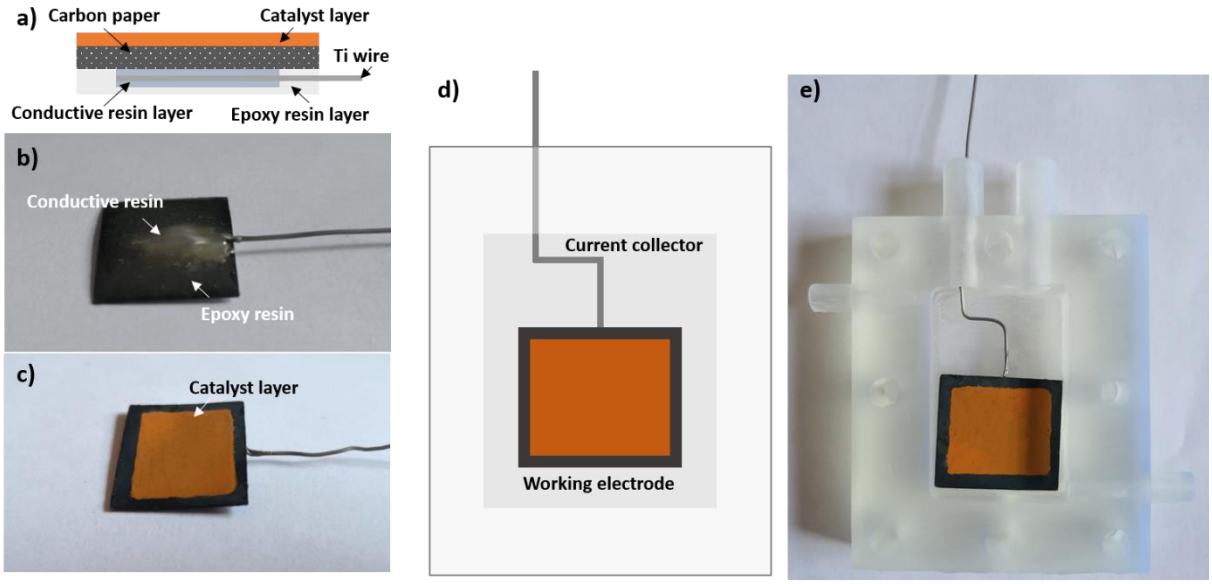

Figure 3.19 a) Schematic of working electrode assembly in H-cell. b) Back-view of electrode c) Top-view of electrode; d) and e) schematic and 3D printed electrode assembly of H-cell

- Electrode – current collector assembly for GDE-type cell

In GDE-type cell, carbon paper supported catalyst was simply compressed with a current collector as the working electrode as shown in Fig. 3.20. The carbon paper was cut into 2 × 2.3

cm^2 and placed in the middle of current collector. The catalysts were painted with a loading rate of 5 mg•cm^{-2} onto the centre of the GDL (1.8 × 2.1 cm^2), and one piece of thin gasket was used to cover the exposed carbon at the edge of the carbon paper.

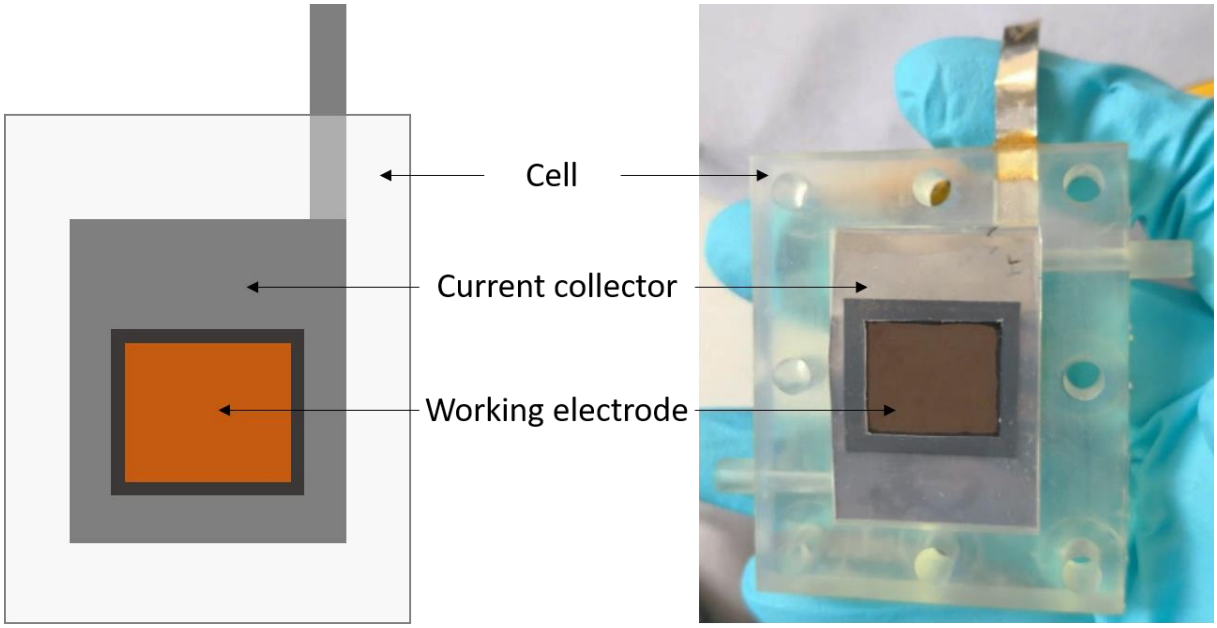

Figure 3.20 Electrode assembly in GDE-cell

Two different methods (painting and spraying) were applied to load the as-prepared catalyst ink onto the carbon paper as shown in Fig. 3.21. We also did the surface characterization and compared the surface morphology differences between the painting and spraying method, the detailed analysis results will be discussed in Section 4.2.4.

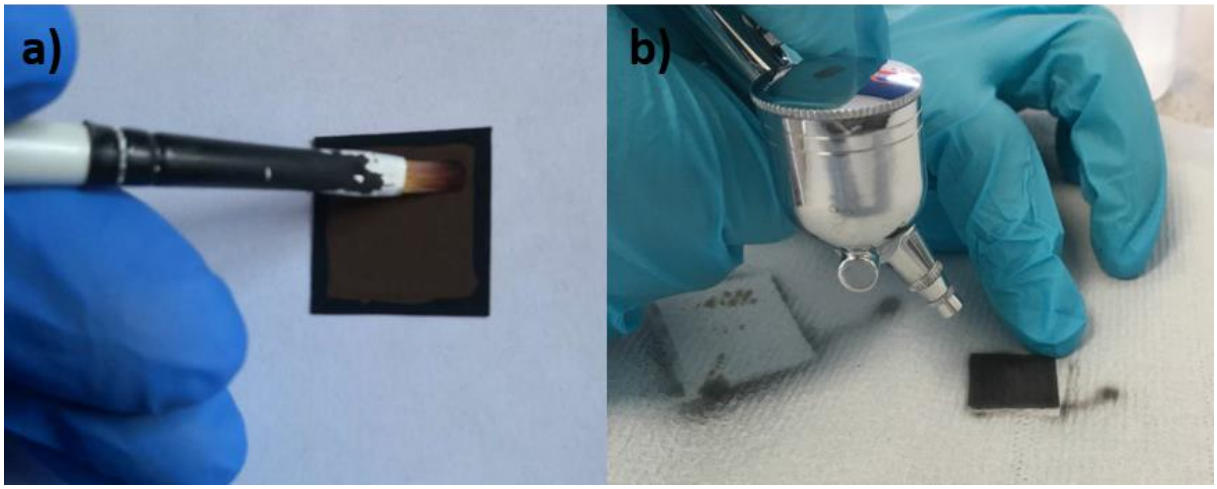

Figure 3.21 a) Painting of catalyst onto carbon paper, b) spraying of catalyst onto carbon paper.

3.9 Electrochemical CO_2 Reduction Reaction Electrochemical Systems

A lab-scale eCO_2RR system has been established as shown in Fig. 3.22. All the electrochemical reactions and measurements were carried out at ambient temperature and pressure, where the cell was self-designed and home-made as illustrated in Section 3.7. The external driving force for the reaction was electric power, which was supplied from the potentiostat/galvanostat. A constant CO_2 gas was supplied into cathode chamber with a precisely controlled flow rate using a flowmeter. A cathodic pump was required to transfer the liquid products and maintain the pH value of catholyte. For product analysis, gaseous products were collected using a gas sampling bags from outlet of cathode chamber and the analysed using the GC. The reduced liquid products were analysed by GC and IC.

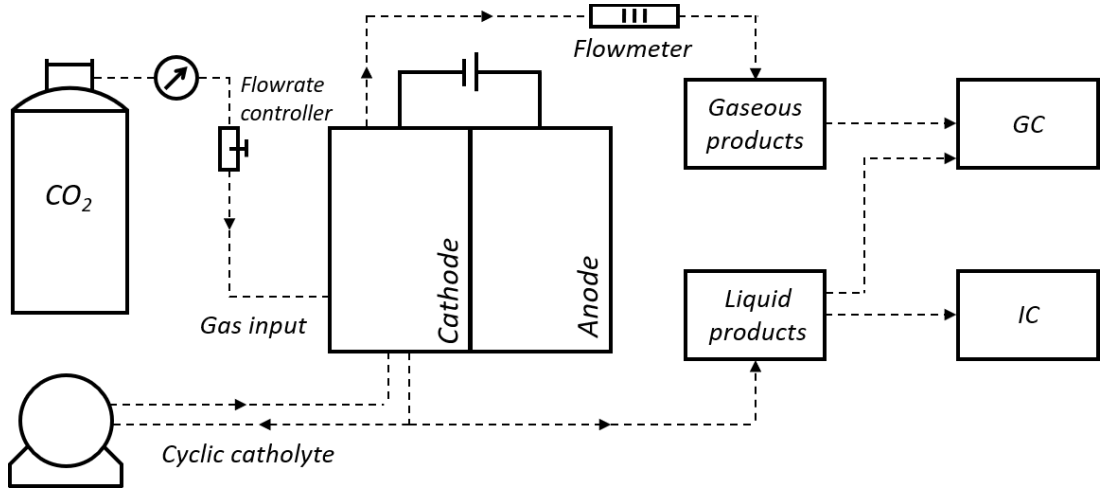

Figure 3.22 Flow diagram of eCO_2RR system

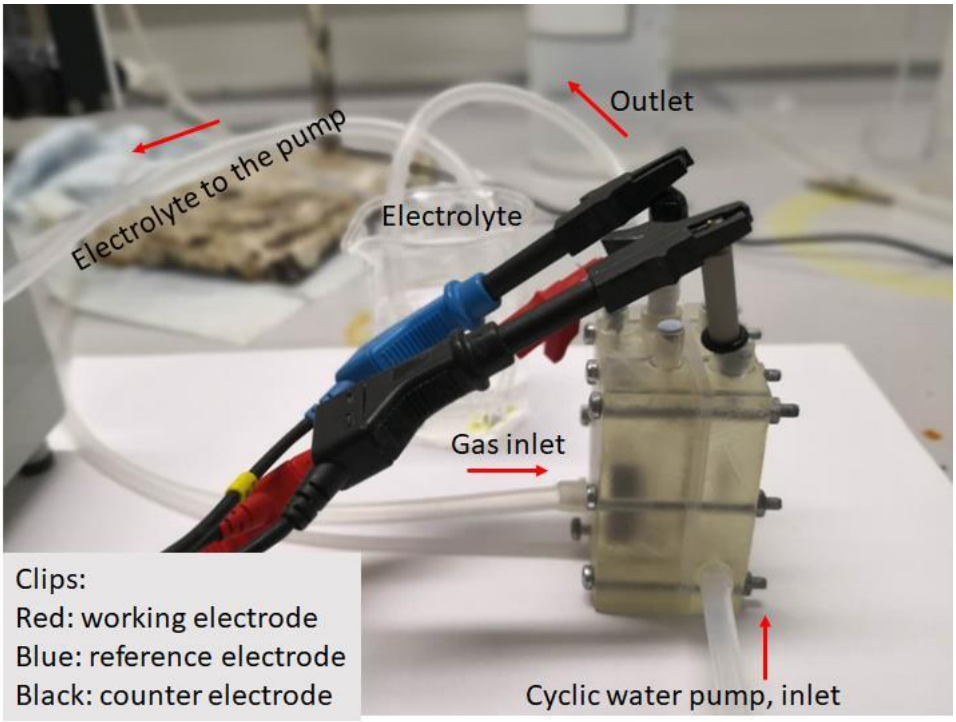

Figure 3.23 Photo of eCO_2RR system

3.10 3D-Printing Technology

The manufacture of electrochemical cells was achieved using the 3D-printing technology. The cells were firstly designed using SOLIDWORKS®, then the designed structures of components were printed under computer control to produce a 3D product. The 3D-printing resin was extruded and laser-cured layer by layer. This process is suitable for additive manufacturing (AM) processes as well as rapid prototyping processes. Two types of 3D-printer were employed in my PhD study, as illustrate below:

- Form 2, Formlabs®

The Form 2 3D printer was used to print H-cells and all GDE cells, and the printer was fed with clear resin (FLGPCL04, Formlabs®). The printed objects by this printer presented good tensile strength of 2.8 GPa[180], and it also presented good gas tightness and insulation properties.

- Objet 30 Pro, Objet®

The accuracy of Objet 30 Pro is down to 0.1 mm[181], which presents a higher accuracy than Form 2. The resin material (Vero White plus, Stratasys, Ltd.) used in Objet 30 Pro has lower strength (50-65 MPa[182]) than Form 2, thus it is feasible to print small and precise objects.

Chapter 4 Cu -contained Catalysts for eCO_2RR

Low activity, low durability and low selectivity of electrocatalyst are the key hurdles limiting the overall energy efficiency in eCO_2RR. In this chapter, commercial and home-made Cu and Cu oxides were introduced as electrocatalysts for eCO_2RR. Cu_2O nano-cubes were synthesized with regularly cubic crystal structure and hugely active catalytic surface area. The efficiency and selectivity of the nano-cube catalysts were investigated using electrochemical methods and product analysis. We have carried out experiments using H-cell and CP-cell, in order to explore the mechanism of mass transfer during eCO_2RR. In addition, the electrode preparation method and concentration of electrolyte were investigated to enhance the efficiency of eCO_2RR.

4.1 Introduction

As illustrated in Chapter 2, Cu has its potential converting CO_2 into high-value added carbonaceous and alcohol under environmental conditions[83-85]. However, electrochemical properties of bulk Cu present relatively low selectivity, low activity, low durability and high overpotential, which are hurdles for its practical use. In order to reduce the energy consumption and improve the energy efficiency, advanced Cu-based catalysts with novel microstructures are demanded for improving the catalytic properties. Graphene is a promising 2D material with its remarkable properties, including excellent electronic conductivity, good optical transmittance, large specific surface area, and superior chemical and mechanical stability. Therefore, fabrication of graphene based electrocatalyst has been regarded as one of the feasible strategies to improve the performance of eCO_2RR[183]. Based on these, we prepared a series of graphene supported Cu_xO_y (Cu_xO_y/Graphene), aiming to find a high-efficient catalyst for eCO_2RR.

Among all yields from eCO_2RR process, CO can be directly used as fuels for intermediate products for many industrial applications [184, 185]. While the electrocatalysts for the CO_2 conversion into CO are mostly the noble metals and their oxides, such as Au, Ag and Pd[186-188]. They are costly and often have problems such as low durability. Therefore, a low-cost substituted electrocatalyst with good energy efficiency and high selectivity of CO is in demand.

In this chapter, we firstly employed several Cu-contained catalysts, including commercial dendritic Cu, home-made Cu_2O nano-cubes, commercial Cu_2O nano particles as listed below, by adjusting the reaction conditions (including electrolyte, applied potential and reaction cells). The aim is to obtain a high selectivity and high Faradaic efficiency of CO and establish a high performance eCO_2RR reaction system.

- Dendritic Cu

The commercial dendric Cu was produced by an electrolytic method. Compared with bulk Cu, dendritic Cu presents a porous structure with a high aspect ratio (e.g., surface/volume). In eCO_2RR, a large surface area means more active sites, while a porous structure could enhance the CO_2 mass transfer. In this work, we employed commercial dendritic Cu powder (Sigma-Aldrich) in our study.

- Cu_2O

Cu_2O is reported to have a good selectivity with a low overpotential in eCO_2RR, where Cu(I) species play a critical role[33, 189, 190]. Here we synthesized Cu_2O nano particles (named as Syn. Cu_2O) using a hydrothermal method as illustrated in Section 3.3.1. The morphology of the nanoparticles we synthesized is nano-cubes. In comparison, we also used a commercial Cu_2O powders (Comm. Cu_2O, EPRUI Nanoparticles & Microspheres Co. Ltd.) for comparisons.

Additionally, we prepared a series of Cu_xO_y/Graphene electrocatalysts for eCO_2RR. By controlling the reaction conditions, four types of catalysts with different particle sizes and

morphology were developed, including nano-needle shaped Cu_xO_y/Graphene (n-Cu_xO_y/Graphene), nano-bundles shaped Cu_xO_y/Graphene (b-Cu_xO_y/Graphene), melted Cu_xO_y/Graphene (m-Cu_xO_y/Graphene) and nano-flower shaped Cu_xO_y/Graphene (f-Cu_xO_y/Graphene). The electrochemical properties of synthesized were tested using the designed H-cell and CP-cell.

4.2 Dendritic Cu and Cu_2O in eCO_2RR

4.2.1 Hydrothermal Methods for Synthesis of Cu_2O

The synthesis of Cu_2O nano particles was carried out using a hydrothermal method. Copper precursor (copper acetate, Sigma-Aldrich, 98%), potassium hydroxide (NaOH, Sigma-Aldrich, 98%), reducing agent ($C_6H_8O_6$ or L-ascorbic acid, Alfa Aesar, 99%) and surfactant (polyvinylpyrrolidone, Sigma-Aldrich, wt. 10000) were mixed with a mass ratio of 4:4:3:1 in a glass beaker for 30 mins under the ambient condition. The detailed reaction procedure has been discussed in Section 3.3.1. The formation process of Cu_2O nano-particles composes the following consecutive reactions[156]:

$$Cu^{2+} + 2OH^- \rightarrow Cu(OH)_2 \downarrow \quad \text{Eq. 4.1}$$

$$Cu(OH)_2 + C_6H_8O_6 \rightarrow Cu^{2+} + 2H_2O + C_6H_6O_6^{2-} \quad \text{Eq. 4.2}$$

$$2Cu^{2+} + C_6H_6O_6^{2-} + H_2O \rightarrow Cu_2O + C_6H_6O_6 + 2H^+ \quad \text{Eq. 4.3}$$

The reactions were carried out in an aqueous solution at the ambient condition with a stirring rate of 400 rpm. An obvious colour change can be observed during the reactions, as shown in Fig. 4.1.

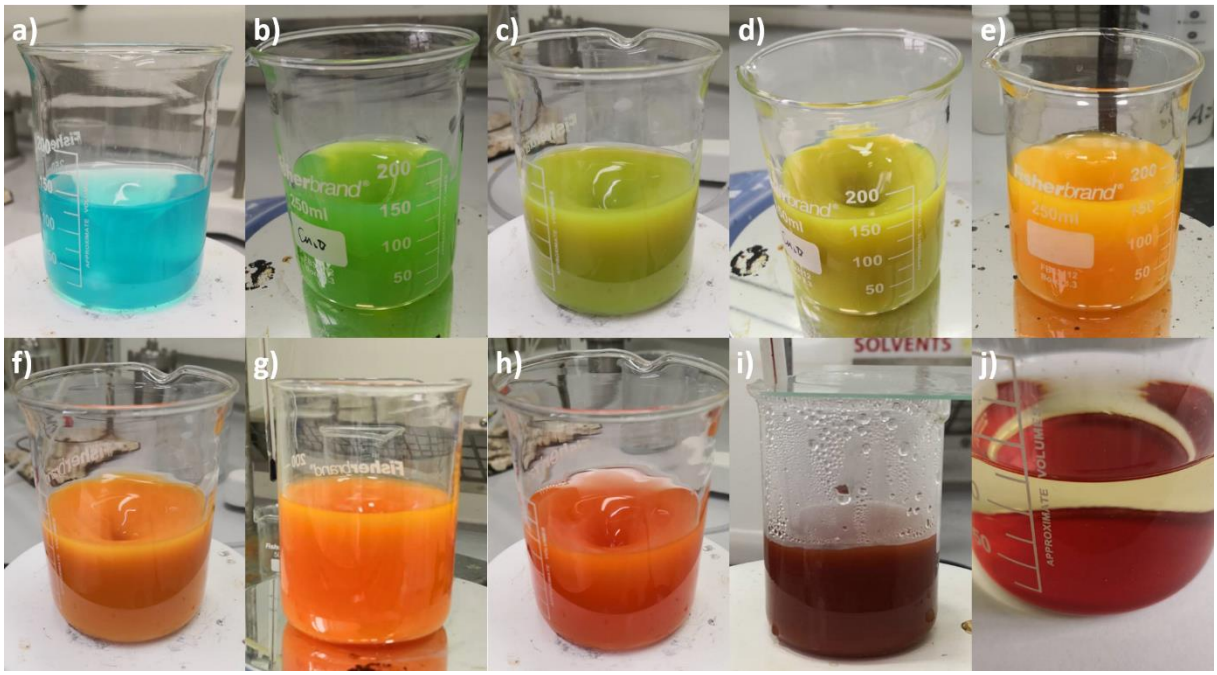

Figure 4.1 Synthesis of Cu_2O nano-cube, observed colour change during reaction, a) Formation of $Cu(OH)_2$ (light blue) suspension after adding of reducer. b-i) Cu(OH) reduced to Cu_2O (dark red), j) Cu_2O precipitation

In these reactions, Cu^{2+} was reacted with OH^- in the alkaline solution, and a blue coloured $Cu(OH)_2$ was firstly observed. After adding the reducing agent, the suspended $Cu(OH)_2$ was gradually reduced into Cu_2O. After further reaction for 30 min, Cu_2O precipitation was obtained. The precipitates were washed by deionised water for three times, centrifuged and dried in the oven. Then the synthesized nano catalyst was ready to use.

4.2.2 Electrochemical Methods

0.5 M and 1 M $KHCO_3$ were used as the catholyte and 1 M $KHCO_3$ was applied as the anolyte. Ag/AgCl and a Platinum wire were used as the reference electrode and counter electrode, respectively. Before the electrochemical test, the catholyte was purged with CO_2 (BOC 99.99%) for 30 min. For all the CP-cell, there is no need to pre-purge CO_2 into electrolyte because CO_2 will diffuse through gas phase rather than being dissolved in electrolyte. The CO_2 gas was constantly supplied with a flow rate during testing, controlled using a flow meter (Cole-Parmer TMR1-010462) with a flow rate of 15 $mL \cdot min^{-1}$.

To evaluate the reaction behaviour, the CA tests were performed at -1.2 V, -1.4 V, -1.6 V, -1.8 V and -2.0 V vs. Ag/AgCl (-0.47 V, -0.67 V, -0.87 V, -1.07 V, -1.27 V vs. RHE) for 1000 s. The current density (*j*) was recorded and then the gas/liquid products were collected for composition analysis using the GC and IC, for analysing gaseous and liquid products, respectively.

CV tests of three catalysts were performed with a half-cell (details are explained in Section 3.7), where catalyst was assembled with a rotating disk as working electrode, Pt as counter electrode, and Ag/AgCl as reference electrode. The scanning potentials were ranged from -1.6 V to -0.6 V vs. Ag/AgCl with a scanning speed of 50 $mV \cdot s^{-1}$. $KHCO_3$ (0.5 M or 1 M) was employed as the electrolyte and was purged with N_2 and CO_2 for 30 min before the tests. The gas flow rate was controlled using a flow meter (Cole-Parmer TMR1-010462) with a flow rate of 15 $mL \cdot min^{-1}$ during testing.

The electrochemical evaluation parameters of dendritic Cu and Cu_2O are listed in Table 4.1.

Table 4.1 Lists of electrochemical evaluation parameters of dendritic Cu and Cu_2O catalysts

No.	Cell	Catalyst	Catholyte	Anolyte	Method
1	Half-cell	Dendritic Cu	0.5M $KHCO_3$*		CV
2	Half-cell	Comm. Cu_2O	0.5M $KHCO_3$*		CV
3	Half-cell	Syn. Cu_2O	0.5M $KHCO_3$*		CV
4	H-cell	Dendritic Cu	0.5M $KHCO_3$	1M $KHCO_3$	CA
5	H-cell	Comm. Cu_2O	0.5M $KHCO_3$	1M $KHCO_3$	CA
6	H-cell	Syn. Cu_2O	0.5M $KHCO_3$	1M $KHCO_3$	CA
7	H-cell	Syn. Cu_2O	1M $KHCO_3$	1M $KHCO_3$	CA
8	CP-cell	Dendritic Cu	0.5M $KHCO_3$	1M $KHCO_3$	CA
9	CP-cell	Comm. Cu_2O	0.5M $KHCO_3$	1M $KHCO_3$	CA
10	CP-cell	Syn. Cu_2O	0.5M $KHCO_3$	1M $KHCO_3$	CA

11	CP-cell	Syn. Cu_2O	1M $KHCO_3$	1M $KHCO_3$	CA

*Only one chamber in Half-cell

4.2.3 Characterization of Catalysts

The commercial and synthesized Cu-based catalysts were characterised using XRD and SEM, and the aims are to identify their morphology and crystal structures.

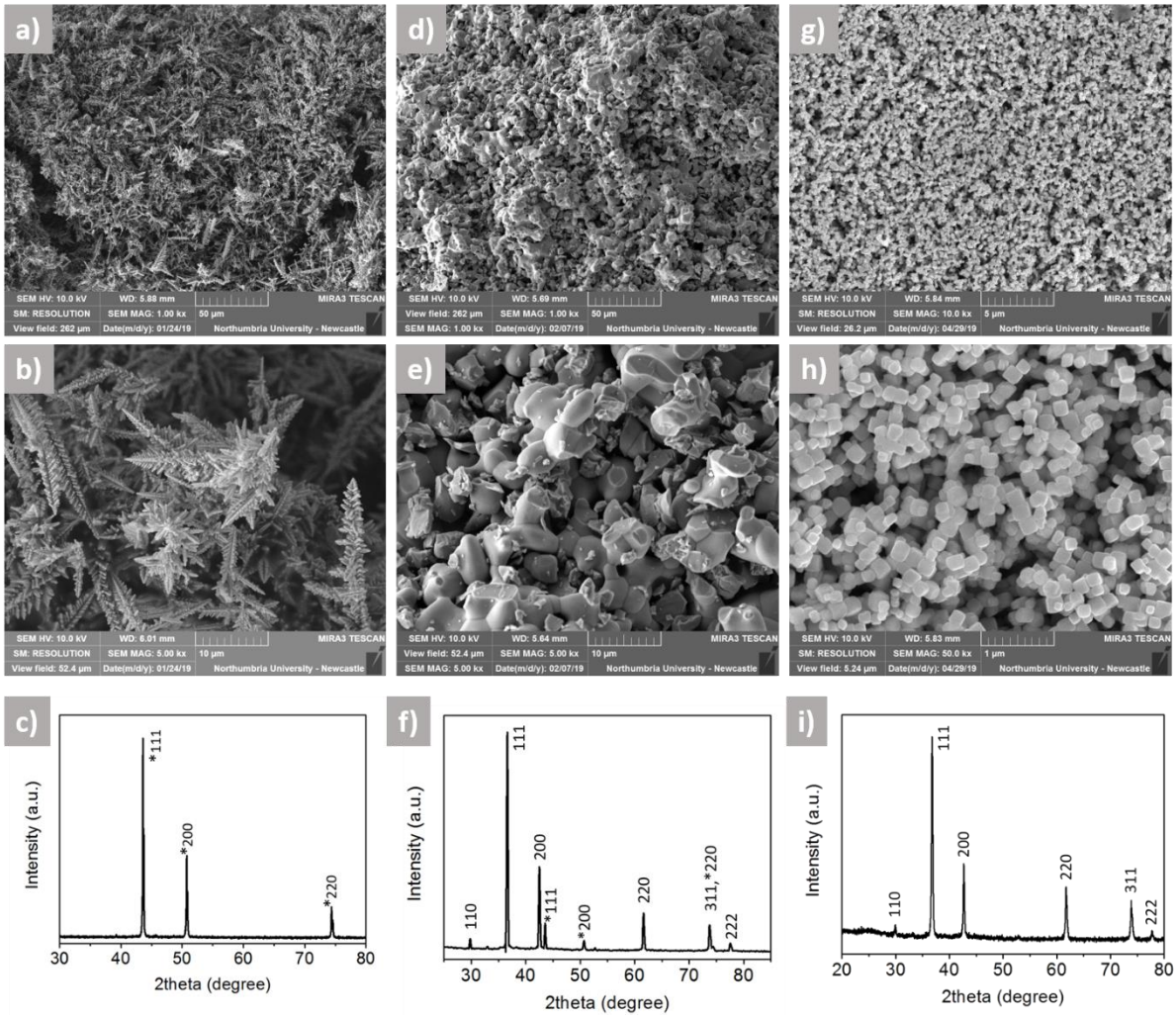

Figure 4.2 SEM images of a&b) Commercial dendritic Cu, d&e) Commercial Cu_2O, g&h) Synthesized Cu_2O nano-cubes. XRD patterns of c) Commercial dendritic Cu f) Commercial Cu_2O i) Synthesized Cu_2O nano-cubes.

Fig. 4.2 shows the Cu-based catalysts with different morphology and particle sizes. Those of the commercial dendritic Cu are shown in Fig. 4.2a and 4.2b with average sizes of 10-20 μm. Their XRD patterns (Fig. 4.2c) exhibit characteristic diffraction peaks of Cu (111) at 2θ of 43º,

Cu (200) at 2θ of 51º, Cu (220) at 2θ of 74º, indicating a typical face centred cubic (FCC) structure[191]. The home-made Cu_2O presents regular nano-cubes with an average length of ca. 200 nm, as shown in Fig. 4.2g and 4.2h. The diffraction peaks in Fig. 4.2i. are observed at 2θ = 30º, 36º, 42º, 61º, 74º and 78º which are related to (110), (111), (200), (220), (311) and (222) reflections of Cu_2O, respectively. The peak positions are consistent with the standard document of Cu_2O (JCPDS No. 05-0667)[192], indicating that the prepared material is crystalline Cu_2O. Meanwhile, no diffraction peaks of other possible impurities (such as Cu and CuO) are detected, demonstrating that the product is the pure Cu_2O[193]. In comparison, commercial Cu_2O presents an irregular surface morphology (ca. 4 μm microspheres) from SEM images (Fig. 4.2d and 4.2e), and its XRD pattern (Fig. 4.2f) shows a Cu_2O phase (Cu_2O (110) at 2θ of 30º, Cu_2O (111) at 2θ of 36º, Cu_2O (220) at 2θ of 61º, Cu_2O (311) at 2θ of 74º, Cu_2O (222) at 2θ of 78º) with minor Cu phase (Cu (111)* at 2θ of 43º, Cu (200)* at 2θ of 51º, Cu (220)* at 2θ of 74º).

4.2.4 Effects of Electrode Assembly

Electrode assembly is the process to load catalyst onto the GDL surface. Good catalyst-GDL interface and evenly distributed catalyst on GDL are the key points which can significantly influence the internal resistance and active sites on catalyst surface. At the meantime, the hydrophobicity of electrodes is related to permeate properties of electrode which will directly influence the stability of electrode. To explore the wettability of electrodes using different preparing methods, three electrodes were prepared by loading the commercial Cu_2O catalyst onto the carbon paper using dripping, painting and spraying method, and their surface morphologies were compared by SEM images (Fig. 4.3).

The PTFE particles can be observed on the original carbon paper surface due to the PTFE hydrophobic coating treatment on carbon paper surface (Fig. 4.3a). An obvious crack was

observed on dripping-treated sample surface under a high magnification SEM image (Fig. 4.3b), where the cracks may cause catalysts felling off from the carbon paper surface during the electrochemical reaction. Meanwhile, from the inset in Fig. 4.3b, the catalyst was stacked together showing its uneven distribution. Compared with that from the dripping treatment, the painting-treated sample shows a flat surface with minor grooves on its surface and a better distribution of catalyst (Fig. 4.3c). Spraying treatment sample presents a wavy catalyst layer, and no cracking is observed under a high magnification SEM image (Fig. 4.3d).

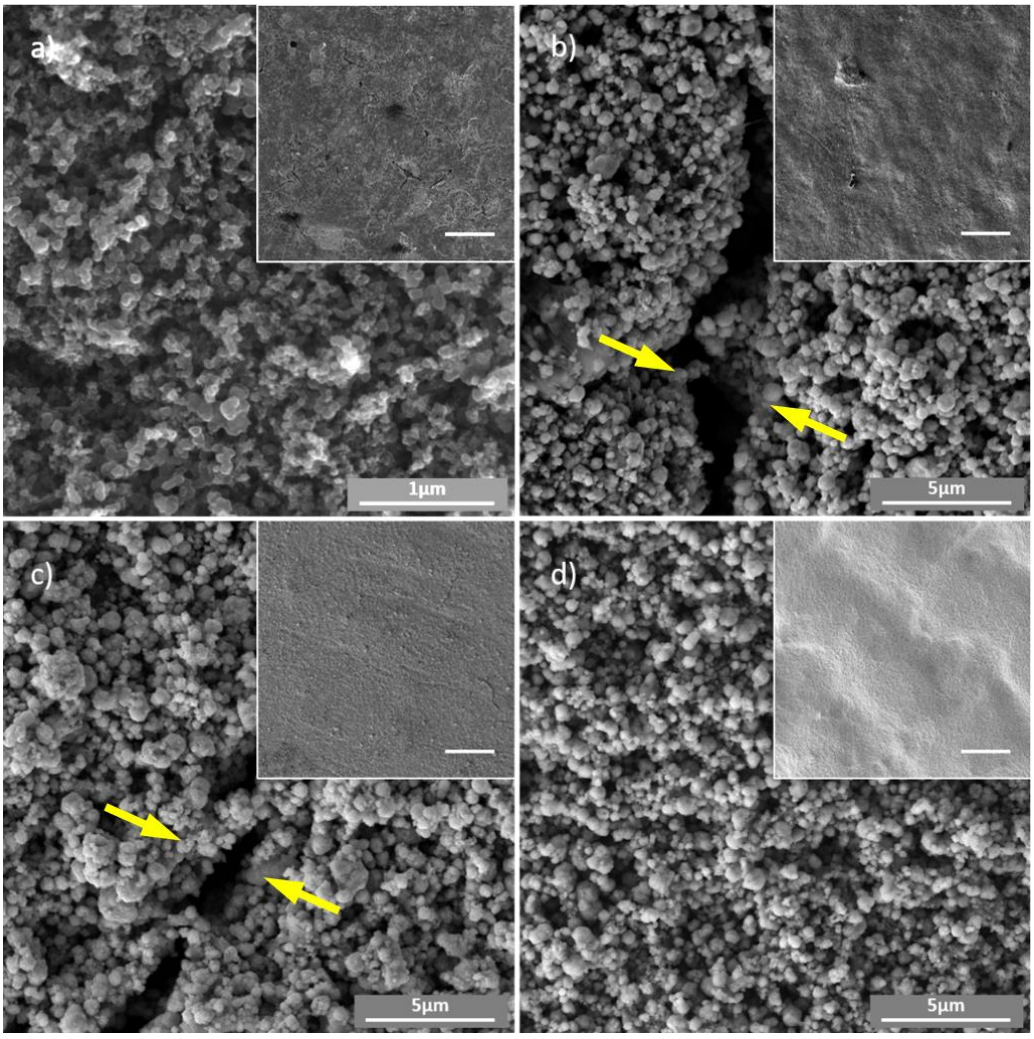

Figure 4.3 Surface morphology of a) original carbon paper (blank experiment), b) catalyst dropped electrode, c) catalyst painted electrode, d) catalyst sprayed electrode. Scale bar of insert images: 200 µm. (Groove between yellow arrows)

To further compare the properties of electrodes obtained using different preparation methods, the wettability of electrodes was analysed by DSA (details in Section 3.4.3) and the contact

angle between droplet and sample surface was measured. Sample images are displayed in Fig. 4.4. A larger contact angle means more hydrophobic properties of the sample surface. Original carbon paper presents the highest contact angle due to a PTFE coating on its surface. After catalyst loading on carbon paper, the GDLs partly lose their hydrophobicity. Among them, the dripping-electrode shows its best hydrophobicity, which is due to its higher surface roughness, while painting and spraying electrodes presents similar hydrophobicity properties.

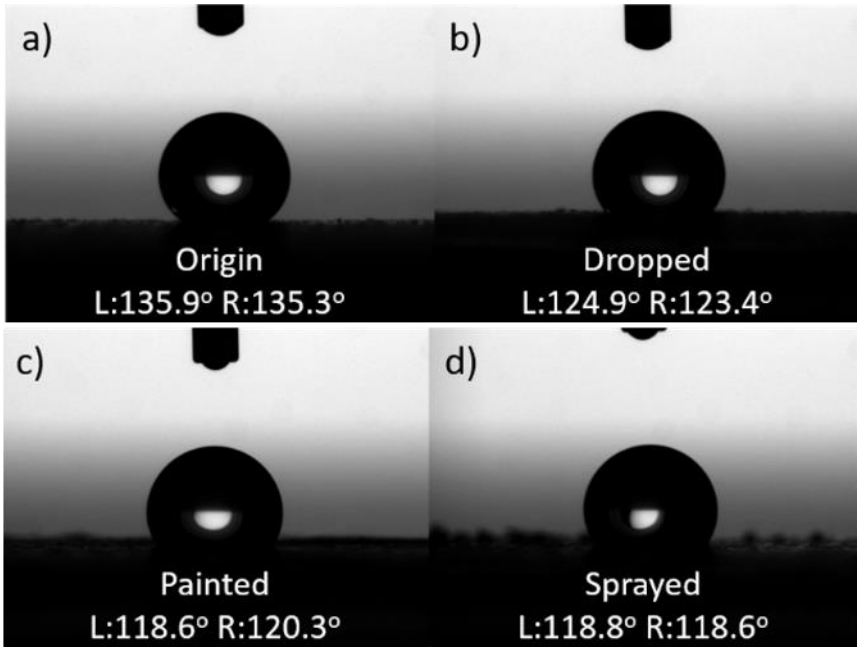

Figure 4.4 DSA contact angle test of carbon paper-based electrode. (droplets: 200 μL deionized water)

Based on the evaluation of electrode demonstrated above, painting and spraying are promised electrode assembly method rather than dropping. In practical work, painting method is easier to control the loading and surface area of catalyst. Therefore, painting method is used in this chapter.

4.2.5 Electrochemical Evaluation in Half-cell

CV results of each sample were obtained using a half-cell at N_2 and CO_2 atmosphere, respectively, as shown in Fig. 4.5.

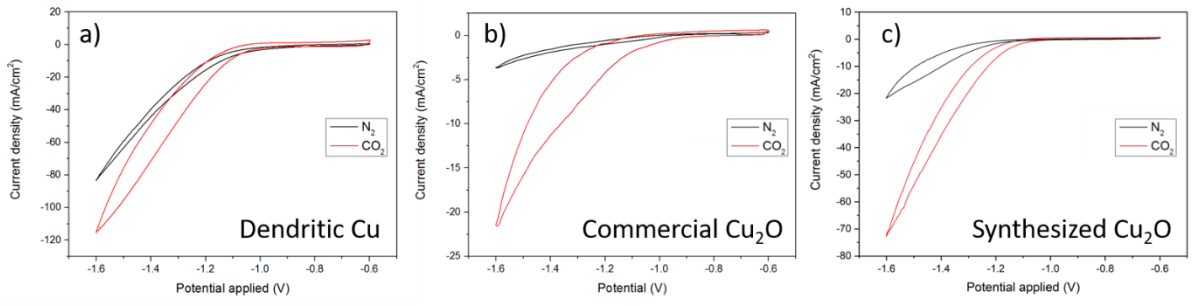

Figure 4.5 CV results of a) dendric Cu b) commercial Cu_2O and c) synthesized Cu_2O in half cell, potential scan from -0.6 V to -1.6 V vs. Ag/AgCl (0.13 V to -0.87 V vs. RHE) in 0.5 M $KHCO_3$.

From the CV results, no obvious redox peaks were found within the scanned potential range. Among them, the dendritic Cu presents the highest current density under N_2 (82 mA•cm^{-2}) and CO_2 (118 mA•cm^{-2}) at -1.6 V vs. Ag/AgCl (-0.87 V vs. RHE, Fig. 4.5a), where the high current density is mainly due to its high conductivity. It also has a high activity as to the lowest onset potential, which could be caused by its high dendric morphology with a large surface area. The onset potential of the reduction reaction was observed to be -1.1 V vs. Ag/AgCl (-0.37 V vs. RHE). While it presents a high current density under N_2, which means the dominant reaction at -1.6 V vs. Ag/AgCl is HER rather than eCO_2RR.

The CV results of commercial Cu_2O are shown in Fig. 4.5b. A very low HER activity is observed under N_2 (4 mA•cm^{-2}) and the current density under CO_2 is 22 mA•cm^{-2}, which is due to its relevantly low surface/volume ratio and low reduction activity. The onset potential of eCO_2RR was observed to be -1.2 V vs. Ag/AgCl (-0.47 V vs. RHE).

The synthesized Cu_2O presents a low reaction activity (21 mA•cm^{-2}) under the N_2 atmosphere, but a high current density value (72 mA•cm^{-2}) under the CO_2 atmosphere. It shows a good potential for eCO_2RR with low activity for HER. The onset potential of eCO_2RR was observed to be -1.2 V vs. Ag/AgCl.

The potential conversion between Ag/AgCl and reversible hydrogen electrode (RHE) is shown in Eq. 4.4:

$$E_{RHE} = E_{Ag/AgCl} + 0.73\ V \qquad \text{Eq. 4.4}$$

4.2.6 Electrochemical Evaluation in H-cell

The eCO_2RRs were carried out with H-cell using the CA electrochemical method at specific fixed potentials including -1.2 V, -1.4 V, -1.6 V, -1.8 V, -2.0 V vs. Ag/AgCl (-0.47 V, -0.67 V, -0.87 V, -1.07 V, -1.27 V vs. RHE), with a fixed reaction time of 1000 s for each individual constant potential scan. The CO_2 was constantly supplied into catholyte and its gas flow rate during testing was controlled using a flow meter (Cole-Parmer TMR1-010462) with a constant flow rate of 15 $mL \cdot min^{-1}$. The cathode chamber and anode chamber were filled with 0.5 M $KHCO_3$ and 1 M $KHCO_3$, respectively. Higher $KHCO_3$ concentration in the anode chamber can help to enhance the cation mass transfer. A gas sampling bag was used to collect the exit gas for analysing the gaseous products using GC, and the catholyte were collected after reaction and tested by IC. The electrochemical results in H-cell are shown in Fig. 4.6.

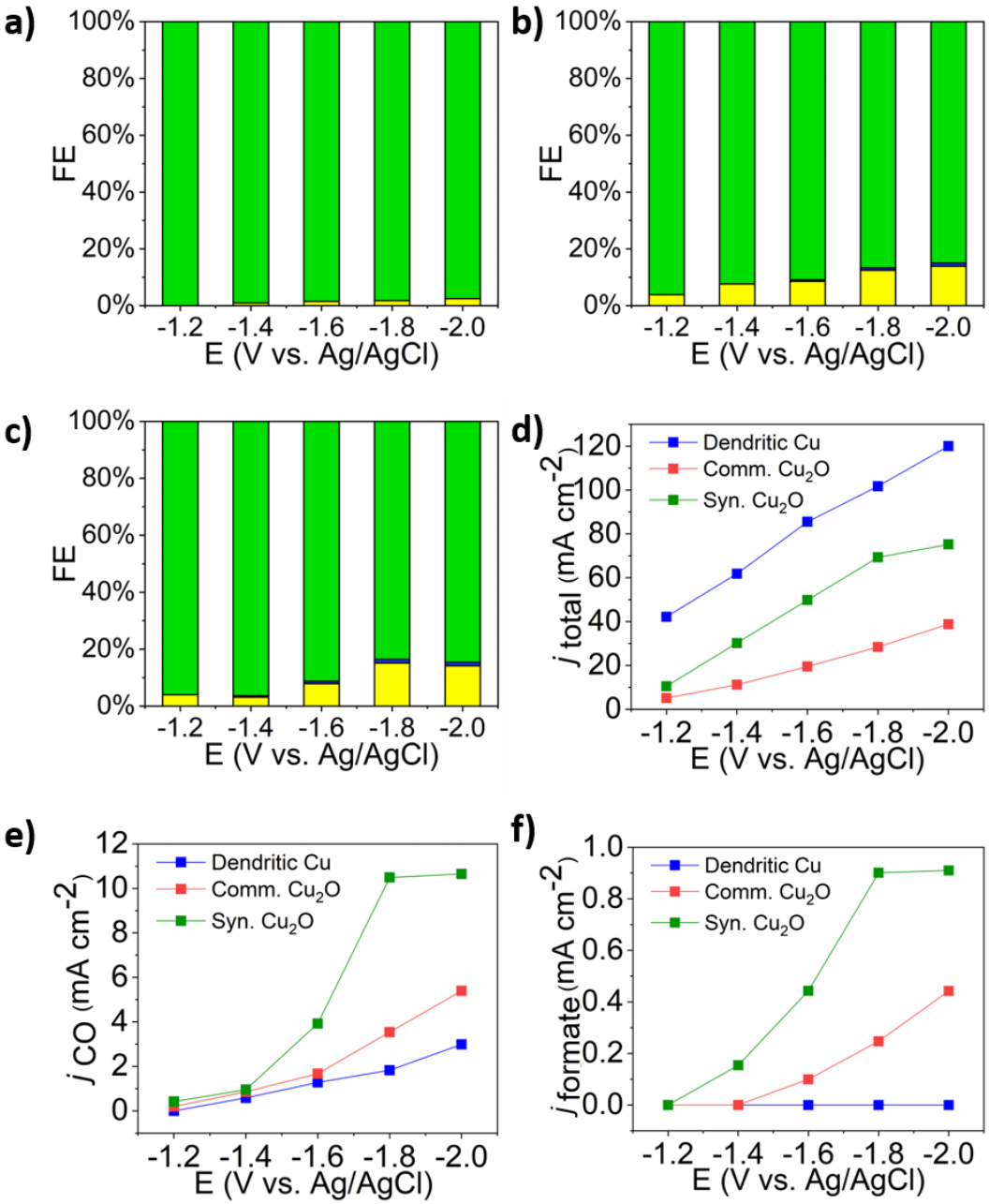

Figure 4.6 Faradaic efficiency profiles of H-cell using a) dendritic Cu, b) Commercial Cu_2O, c) Synthesized Cu_2O catalyst in 0.5 M $KHCO_3$ electrolyte of eCO_2RR with products including CO (yellow, bottom), Formate (blue, middle), H_2 (green, top); d) Total current density, e) Current density of CO and f) Current density of formate for results in a-c.

As shown in Fig. 4.6a, HER dominates the reaction in dendritic Cu, and only a small amount of CO has been produced. Although it has the highest current density (Fig. 4.6d) due to its high conductivity and dendritic morphology, the current densities for CO and formate (Fig. 4.6e and 4.6f) are relevantly low. Its FE values of CO at potentials of -1.2 V to -2.0 V vs

Ag/AgCl (-0.47 V to -1.27 V vs. RHE) are 0.00%, 0.95%, 1.50%, 1.80%, 2.49%, and no formate are obtained. Compared with those using the dendritic Cu, commercial Cu_2O shows a lower total current density due to its irregular surface morphology with smaller surface area, while it shows higher activity (higher current density as shown in Fig. 4.6e and 4.6f) towards CO and formate. From the product analysis, the FE for carbonaceous products for the commercial Cu_2O are slightly higher than those using the dendritic Cu. The FE values of CO are 3.90%, 7.65%, 8.56%, 12.48% 13.90% at potentials of -1.2 V to -2.0 V vs Ag/AgCl. Minor contents of formate are detected, with FE of formate at potentials of -1.2 V to -2.0 V vs Ag/AgCl are 0%, 0%, 0.51%, 0.87% and 1.14% (Fig. 4.6b). Among these catalysts, the home-made cubic Cu_2O shows the highest FE of CO and formate (Fig 4.6c) with a moderate total current density, mainly due to its nano-cube structure with considerably large surface areas. The FE of CO are 3.99%, 3.17%, 7.88%, 15.14%, 14.16% at potentials of -1.2 V to -2.0 V vs Ag/AgCl, and FE of formate are 0%, 0.51%, 0.89%, 1.30%, 1.21% at potentials of -1.2 V to -2.0 V vs Ag/AgCl (detailed data in Appendix 2).

All these catalysts present low activities towards eCO_2RR, where the HER dominates the reaction in all tests using H-cell. Therefore, the mass transfer issue should be considered. A low concentration of catholyte could limit the mass transfer of protons, which could reduce the overall reaction. The solution is to enhance the concentration of catholyte. A low solubility of CO_2 in H-cell could limit the CO_2 mass transfer and reduce the efficiency of eCO_2RR, therefore, a better cell design should be considered.

Based on the results and discussion above, higher concentration of catholyte (1 M $KHCO_3$) was employed using synthesized Cu_2O, and the obtained results are shown in Fig. 4.7.

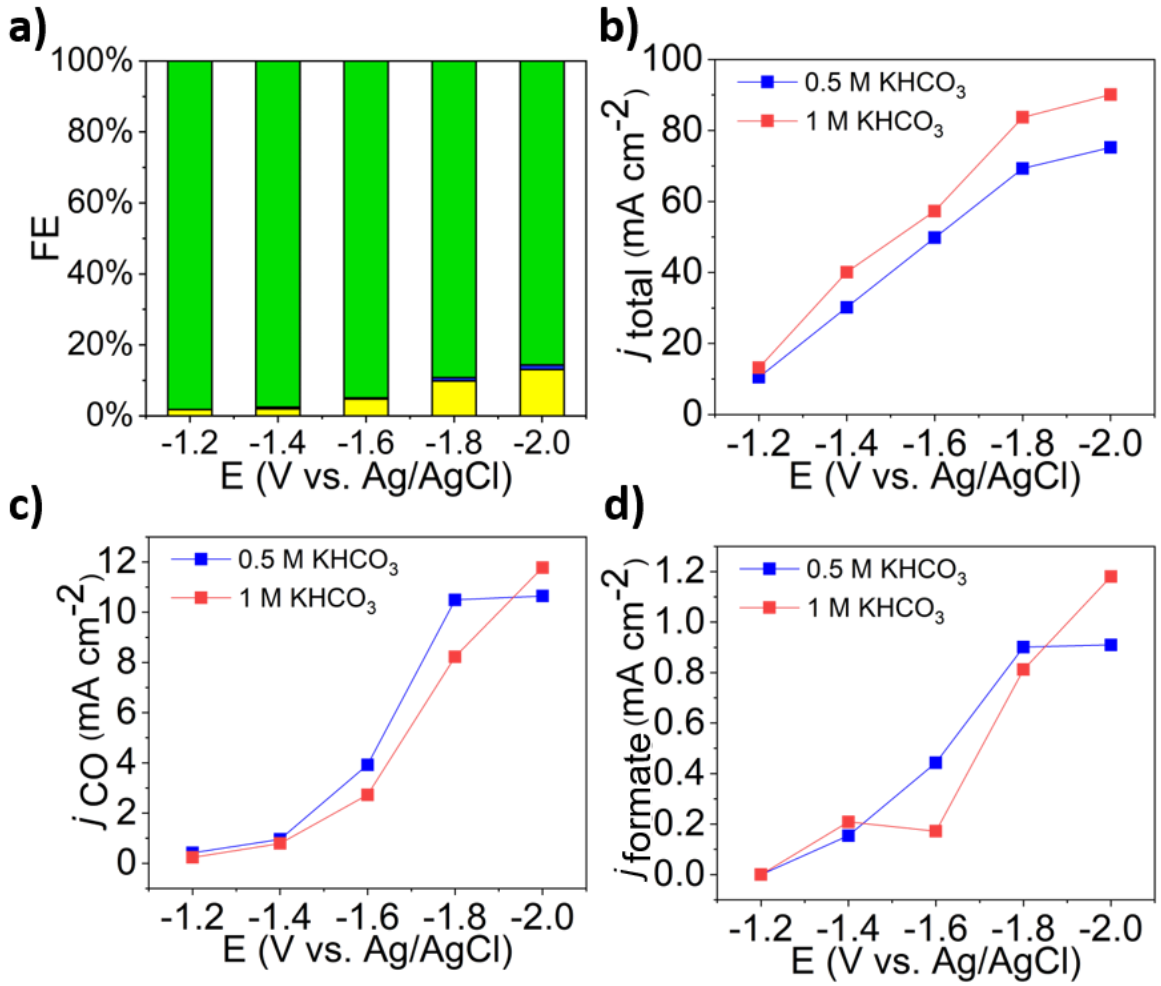

Figure 4.7 a) Faradaic efficiency profiles of H-cell using synthesized Cu_2O catalyst in 1 M $KHCO_3$ electrolyte of eCO_2RR with products including CO (yellow, bottom), Formate (blue, middle), H_2 (green, top) b) Total current density c) Current density of CO and d) Current density of formate of synthesized Cu_2O in 0.5 M $KHCO_3$ (blue) and 1 M $KHCO_3$ (red).

Compared with the FE results of the synthesized Cu_2O in 0.5 M $KHCO_3$ (Fig. 4.6c), there has no obvious enhancement of eCO_2RR activity by increasing the concentration of catholyte (Fig. 4.7a). From Fig. 4.7b, only minor increase of total current density is observed, which is due to a higher HER activity caused by an enhanced proton mass transfer[194] with higher concentration of electrolyte, but there is no significant enhancement of FE of CO or formate (Fig. 4.7c and 4.7d).

From the results above, it can be concluded that the HER is dominant for the overall reaction with low CO_2 mass transfer problem in H-cell. Enhancing the concentration of electrolyte

enhanced the proton transfer in electrolyte, but no significant enhancement of FEs for carbonaceous products was observed. Therefore, CO_2 mass transfer is the key problem which limits the overall efficiency of eCO_2RR.

4.2.7 Electrochemical Evaluation in CP-cell

Based on the results in Section 4.2.6, HER domains the reaction in H-cell and reduces the efficiency of eCO_2RR due to the low performance of CO_2 mass transfer. Therefore, the CP-cell was introduced to explore the mass transfer effect in eCO_2RR. Here we use the catalysts carried out by CA electrochemical method in the CP-cell. The parameters setting of scanned potential, concentration of electrolyte and reaction time were the same with those of the H-cell, while CO_2 gas was constantly supplied from the inlet of gas chamber then diffused through GDL and reached to the catalyst surface. The flow rate of CO_2 was controlled with a same value of 15 $mL \cdot min^{-1}$. The electrochemical results in CP-cell are shown in Fig. 4.8.

It is obvious that the FE results of carbonaceous products has been enhanced using CP-cell, due to the enhanced CO_2 mass transfer. Sufficient CO_2 could facilitate the eCO_2RR and supress the HER. Meanwhile, the properties of catalysts influence the efficiency and selectivity of products. The results of dendritic Cu are shown in Fig. 4.8a. The obtained FEs of H_2 at potentials of -1.2 V to -2.0 V vs Ag/AgCl, are 81.44%, 79.20%, 73.79%, 71.63%, 72.92%, which domains the overall reaction. The FE of CO at potentials of -1.2 V to -2.0 V vs Ag/AgCl are 2.56%, 2.64%, 5.60%, 8.16% and 7.98%, respectively. The FE of formate has a significant enhancement at the potentials of -1.2 V to -2.0 V vs Ag/AgCl, which are 16.00%, 18.16%, 20.61%, 20.21% and 19.10%, respectively. It is also noticeable that the current density of dendritic Cu in the CP-cell is lower than that of the H-cell, which is influenced by the supressed

reactions of hydrogen revolution. It also has the highest current density of formate as shown in Fig. 4.8f.

Fig 4.8b shows the results of commercial Cu_2O, where it presents the lowest current density at all tested potentials. From the results, it has considerable FE of carbonaceous products, and the FE values of CO at the potentials of -1.2 V to -2.0 V vs Ag/AgCl, are 26.61%, 34.46%, 46.80%, 48.27%, 45.52%. The FE values of formate at the potentials of -1.2 V to -2.0 V vs Ag/AgCl, are 14.99%, 13.38%, 16.37%, 19.08%, 14.84%. It has lowest total current density but moderate current densities of CO and formate.

The synthesized Cu_2O has a considerable FE and current density of CO as shown in Fig 4.8c and 4.8e. The FE values of CO at potentials of -1.2 V to -2.0 V vs Ag/AgCl, are 35.08%, 49.10%, 50.89%, 54.80%, 55.42%, which domain the reactions at all the tested potentials. The results also show that the synthesized Cu_2O catalyst has less selectivity of formate, and the FE values of formate at potentials of -1.2 V to -2.0 V vs Ag/AgCl, are 5.66%, 5.92%, 6.88%, 7.04%, 7.62%.

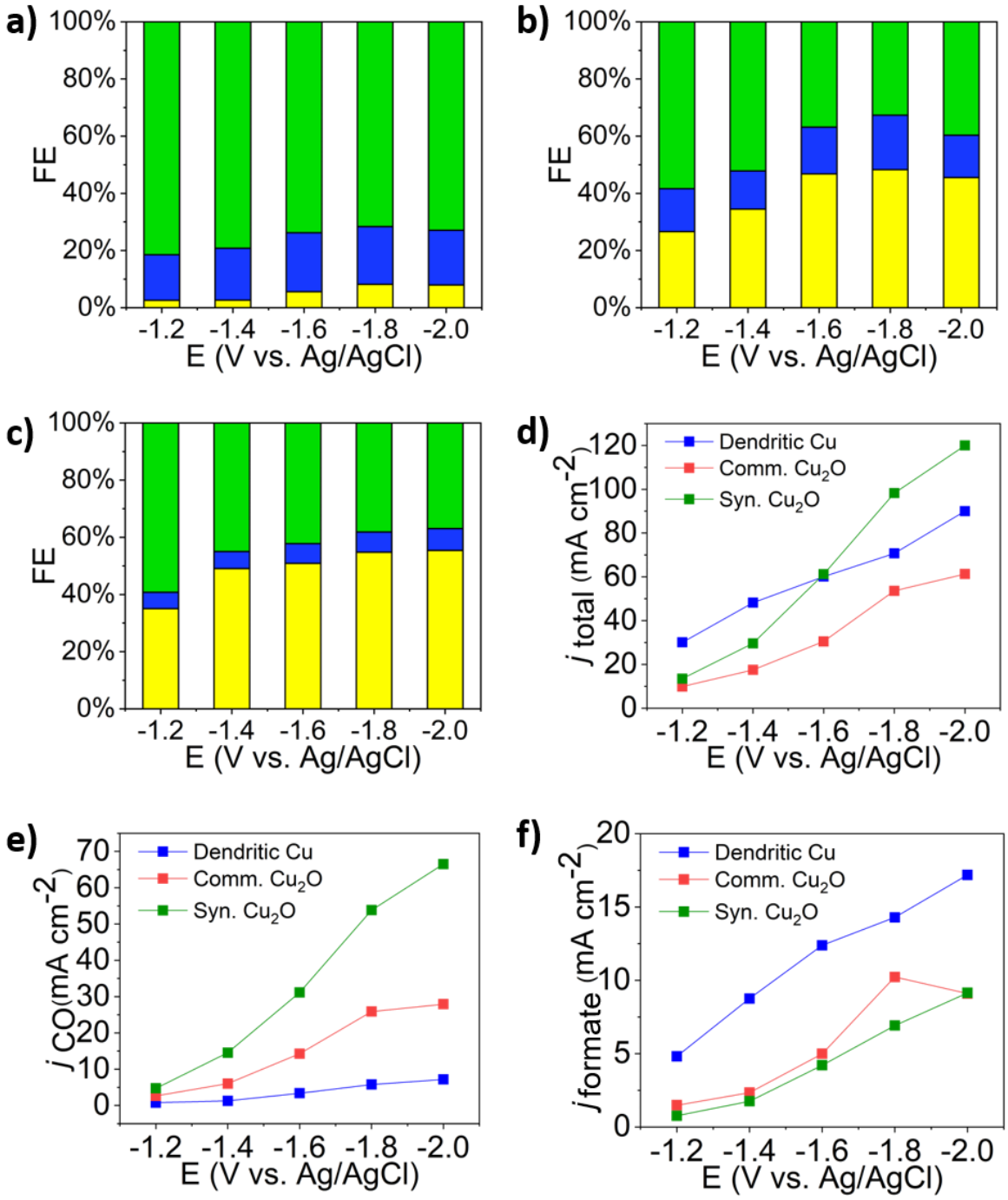

Figure 4.8 Faradaic efficiency profiles of CP-cell using a) dendritic Cu, b) Commercial Cu_2O, c) Synthesized Cu_2O catalyst in 0.5 M $KHCO_3$ electrolyte of eCO_2RR with products including CO (yellow, bottom), Formate (blue, middle), H_2 (green, top); d) Total current density, e) Current density of CO and f) Current density of formate for results in a-c.

From the above results, it is concluded that the FE values of overall reaction is controlled by catalyst and CO_2 mass transfer. By enhancing the CO_2 supplying method, the HER can be supressed and thus the FE value of carbonaceous products can be enhanced.

In order to explore the electrolyte influence in CP-cell, 1 M $KHCO_3$ was used as catholyte to enhance the proton transfer.

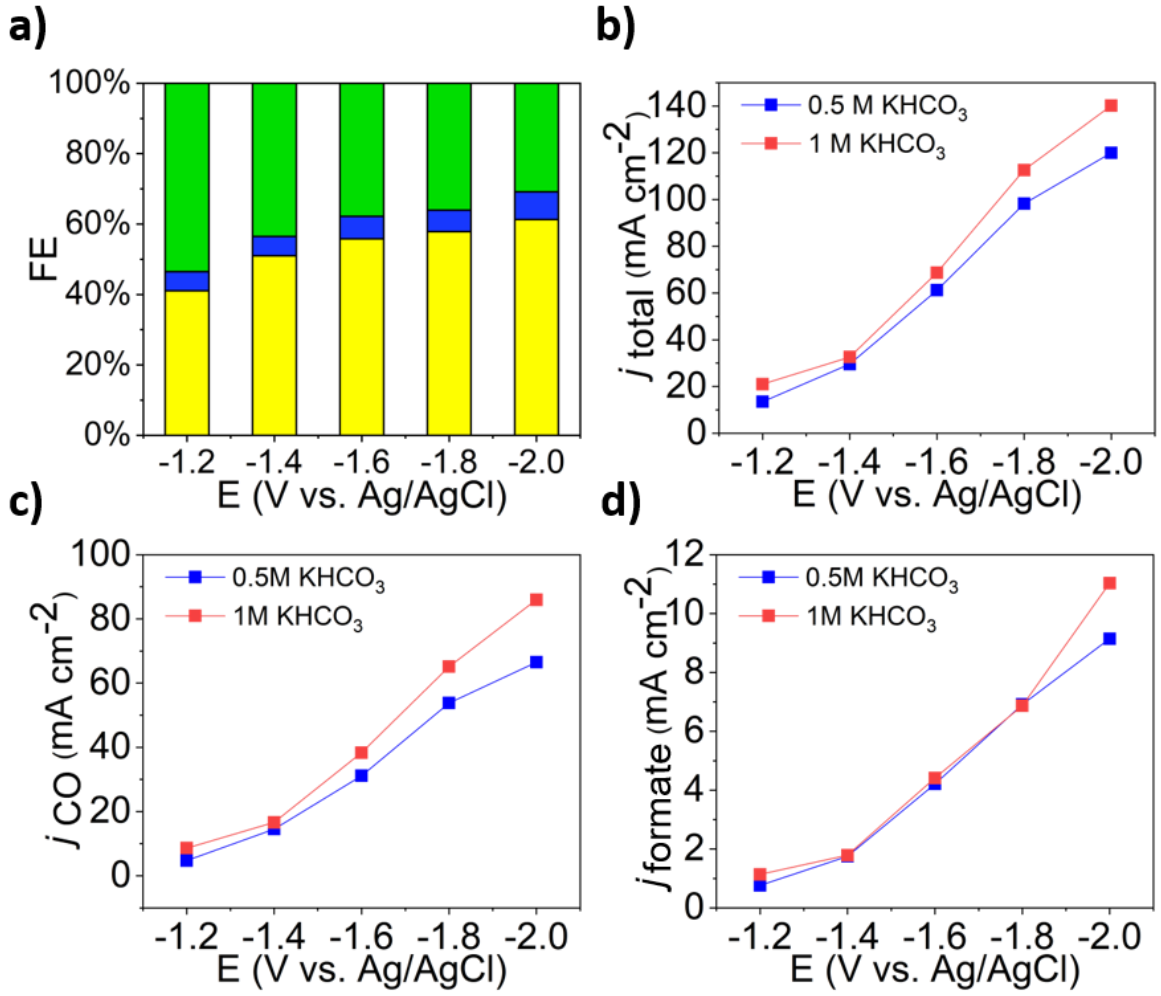

Figure 4.9 a) Faradaic efficiency profiles of CP-cell using synthesized Cu_2O catalyst in 1 M $KHCO_3$ electrolyte of eCO_2RR with products including CO (yellow, bottom), Formate (blue, middle), H_2 (green, top) b) Total current density c) Current density of CO and d) Current density of formate of synthesized Cu_2O in 0.5 M $KHCO_3$ (blue) and 1 M $KHCO_3$ (red).

Compared with those using the 0.5 M $KHCO_3$, the result of synthesized Cu_2O in 1 M $KHCO_3$ presents better reaction activity and selectivity of CO. The FE values of CO at potentials of -1.2 V to -2.0 V vs Ag/AgCl, are 41.07%, 50.98%, 55.80%, 57.85%, 61.31%, and FE values of formate at potentials of -1.2 V to -2.0 V vs Ag/AgCl, are 5.42%, 5.49%, 6.42%, 6.10%, 7.87%, respectively. Higher total current density on formation of CO can be observed in Fig. 4.9c.

Clearly better results can be obtained by enhancing mass transfer of reactants (CO_2 mass transfer and proton mass transfer).

4.3 Electrochemical Evaluation of Cu_xO_y/Graphene Nanoparticles

4.3.1 Reduction of Graphene Oxide

Graphene oxide was introduced as a precursor to produce graphene nanosheet, which can be used as the substrate. Here we use CV test to find the electrochemical properties of graphene oxide before and after reduction reaction. Graphene oxide and reduced graphene were brush painted on carbon paper (with PTFE single-face coating) and the electrochemical properties was tested using a half-cell, with 0.5 M $KHCO_3$ as electrolyte. The obtained results are shown in Fig. 4.10.

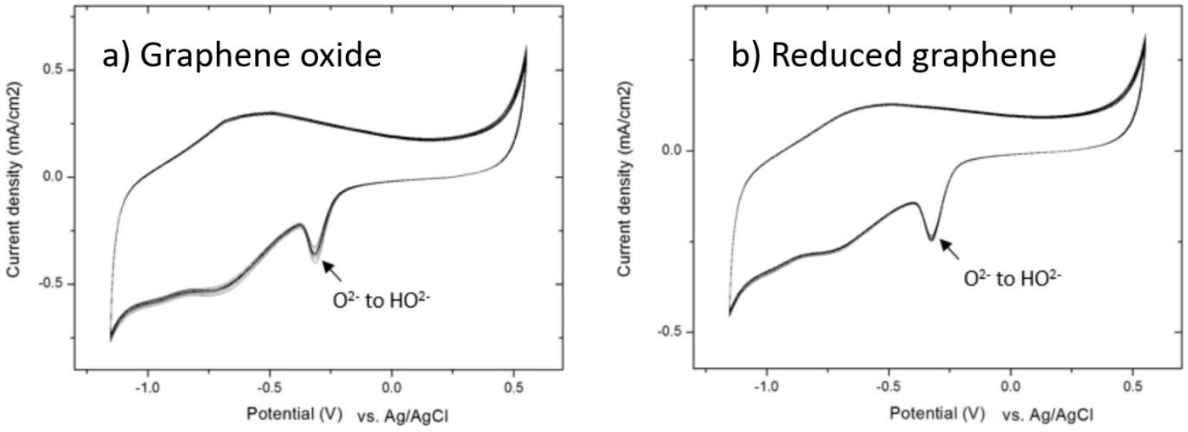

Figure 4.10 Cyclic Voltammogram of a) Graphene oxide, b) Reduced graphene in 0.5 M $KHCO_3$ at potential range from -1.3 V to 0.6 V vs. Ag/AgCl, the scan rate is 50mV•s^{-1}.

The CV plot in Fig. 4.10 shows that a peak appears at -0.7 vs. Ag/AgCl. Peaks at -0.7 V and -0.36 V vs. Ag/AgCl show a gradual decrease on current density, which could be the reduction of GO to graphene.

4.3.2 Morphology Control of Cu_xO_y/Graphene

The substrate can significantly affect the morphology and catalyst properties of the catalysts. As a novel material, graphene presents an extremely large surface-to-volume ratio, owning to its 2D nature and single-atom thickness. Moreover, its high chemical stability and ultrahigh thermal conductivity could potentially facilitate the high loading of catalytically active sites[195]. In order to investigate and develop a high-performance catalyst for eCO_2RR, the reaction temperature was controlled. SEM was employed to characterise the morphology changes of the Cu_xO_y/Graphene catalysts.

Four catalysts with different morphologies were obtained by controlling the reaction conditions. We firstly developed an n-Cu_xO_y/Graphene, which was synthesised at the temperature of 80 ^oC and standard pressure conditions (Figs. 4.11a and 4.11b). Nano-needle shaped particles were obtained under this reaction condition, with ca. 500 nm longitudinal length and ca. 100 nm diameter.

Higher temperature was then applied aiming to obtain a catalyst with a higher surface-to-volume ratio. Therefore, the reaction temperature was raised to 90 ^oC. A nano-bundle shaped catalyst was observed (b-Cu_xO_y/Graphene, Fig. 4.11c and 4.11d) with 2-2.5 μm longitudinal length, and 80-100 nm diameter for these bundles. The existence of bundles significantly increases the surface area of catalyst.

In order to obtain larger surface area/volume ratio of the catalyst, a higher reaction temperature was applied during reaction process, to further split the nano-bundles. However, once the reaction was increased to 100 ^oC (Figs. 4.11e and 4.11f), a ‘melted’ particles was obtained (m-

Cu_xO_y/Graphene, 2-3 μm longitudinal length, 70 μm horizontal length), which may be caused by the deconstruction of microstructure at such a high temperature.

Then we employed 1g sodium dodecyl sulfate (SDS) as the surface surfactant mixed with Cu precursor before reaction, and obtained an f- Cu_xO_y/Graphene as shown in Fig. 4.11g and 4.11h. Compared with the b-Cu_xO_y/Graphene, this f- Cu_xO_y/Graphene has thinner little bundles with ca. 50 nm diameter, and the overall longitudinal length is about 3 μm. It has considerably large surface areas which are beneficial for eCO_2RR.

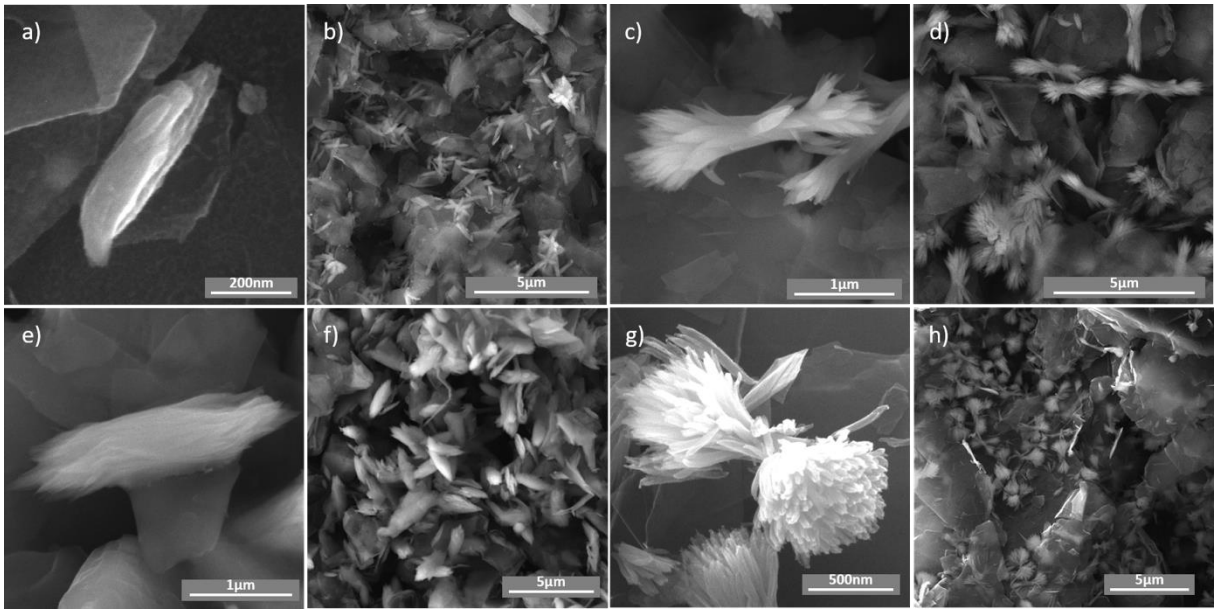

Figure 4.11 SEM images of synthesized Cu_xO_y/Graphene particles under different reaction conditions a-b) n-Cu_xO_y/Graphene, 80°C c-d) b-Cu_xO_y/Graphene, 90°C e-f) m-Cu_xO_y/Graphene, 100°C g-h) f-Cu_xO_y/Graphene, 90°C with surfactant

4.3.3 Electrochemical Methods

In order to investigate substrate influences of catalyst, we applied the Cu_xO_y/Graphene catalysts in H-cell and CP-cell, respectively. Their electrochemical behaviours were compared with the synthesized Cu_2O catalyst (states in Section 4.2). The CV tests were performed with a half-cell at potentials range from -1.2 V to 0.6 V vs. Ag/AgCl with scanning speed of 50 $mV \cdot s^{-1}$. The Pt wire was used as the counter electrode and the Ag/AgCl as reference electrode. 0.5 M $KHCO_3$

was employed as the electrolyte and was purged with N_2 and CO_2 for 30 min before the tests. The CA tests were performed at -1.2 V, -1.4 V, -1.6 V, -1.8 V and -2.0 V vs. Ag/AgCl (-0.47 V, -0.67 V, -0.87 V, -1.07 V, -1.27 V vs. RHE) for 1000 s. The current density (*j*) was recorded and then the gas/liquid products were collected for composition analysis using the GC and IC, for analysing gaseous and liquid products, respectively.

The electrochemical evaluation parameters for the Cu_xO_y/Graphene are listed in Table 4.2.

Table 4.2 List of electrochemical evaluation of Cu_xO_y/Graphene catalysts

No.	Cell	Catalyst/material	Catholyte	Anolyte	Method
1	H-cell	n-Cu_xO_y/Graphene	0.5M $KHCO_3$	1M $KHCO_3$	CV, CA
2	H-cell	b-Cu_xO_y/Graphene	0.5M $KHCO_3$	1M $KHCO_3$	CV, CA
3	H-cell	m-Cu_xO_y/Graphene	0.5M $KHCO_3$	1M $KHCO_3$	CV, CA
4	H-cell	f-Cu_xO_y/Graphene	0.5M $KHCO_3$	1M $KHCO_3$	CV, CA
5	CP-cell	n-Cu_xO_y/Graphene	0.5M $KHCO_3$	1M $KHCO_3$	CA
6	CP-cell	b-Cu_xO_y/Graphene	0.5M $KHCO_3$	1M $KHCO_3$	CA
7	CP-cell	m-Cu_xO_y/Graphene	0.5M $KHCO_3$	1M $KHCO_3$	CA
8	CP-cell	f-Cu_xO_y/Graphene	0.5M $KHCO_3$	1M $KHCO_3$	CA

4.3.4 Electrochemical Evaluation in H-cell

The performance of Cu_xO_y/Graphene catalysts were firstly evaluated by CV using H-cell in 0.5 M $KHCO_3$ catholyte and 1 M $KHCO_3$ anolyte. The potential ranges were from -0.6 V to -1.6 V vs. Ag/AgCl (0.13 V to -0.87 V vs. RHE), with scanning rate of 50 $mV \cdot s^{-1}$.

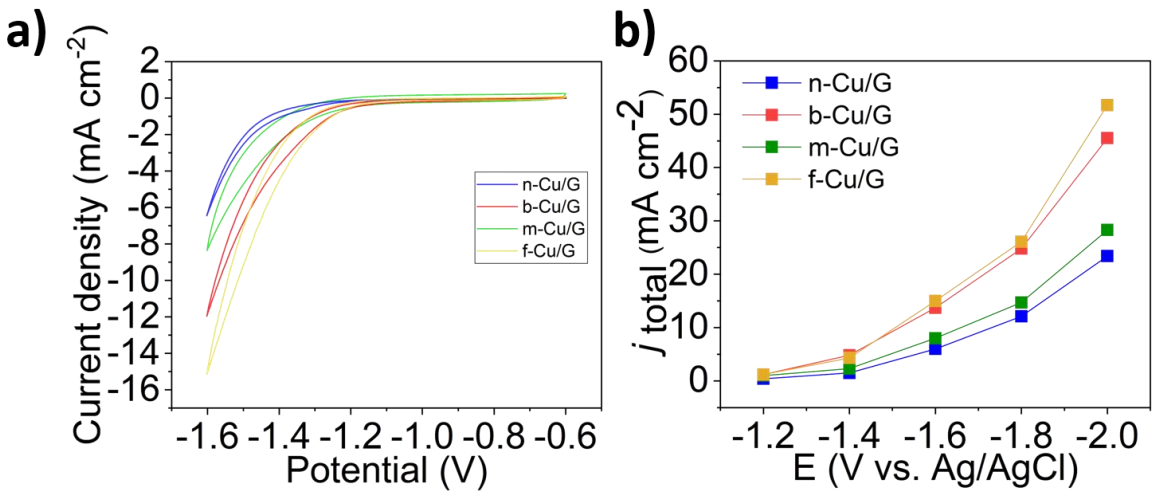

Figure 4.12 a) CV of Cu_xO_y/Graphene catalysts in H-cell b) total current density of Cu_xO_y/Graphene in H-cell

From the CV results shows in Fig. 4.12a, all the Cu_xO_y/Graphene catalysts present low current densities, and no obvious redox peaks can be observed. Among them, the f-Cu_xO_y/Graphene shows the highest current density (15.1 mA•cm^{-2}). However, compared with that of the synthesized Cu_2O (72 mA•cm^{-2}), a lower current density has been obtained. The explanation of this lower value is the less loading of Cu oxides for f-Cu_xO_y/Graphene compared with synthesized Cu_2O. Therefore, less active sites on the f-Cu_xO_y/Graphene surface results a lower activity of eCO_2RR.

To further evaluate its selectivity and efficiency, the catalysts were evaluated using CA method and products analysis. Fig. 4.12b shows the current density results. There are no carbonaceous products are detected, which means that only HER happens.

4.3.5 Electrochemical Evaluation in CP-cell

We further employed a CP-cell for eCO_2RR and product analysis. The FEs of products and current density in CP-cell are presented in Fig. 4.13.

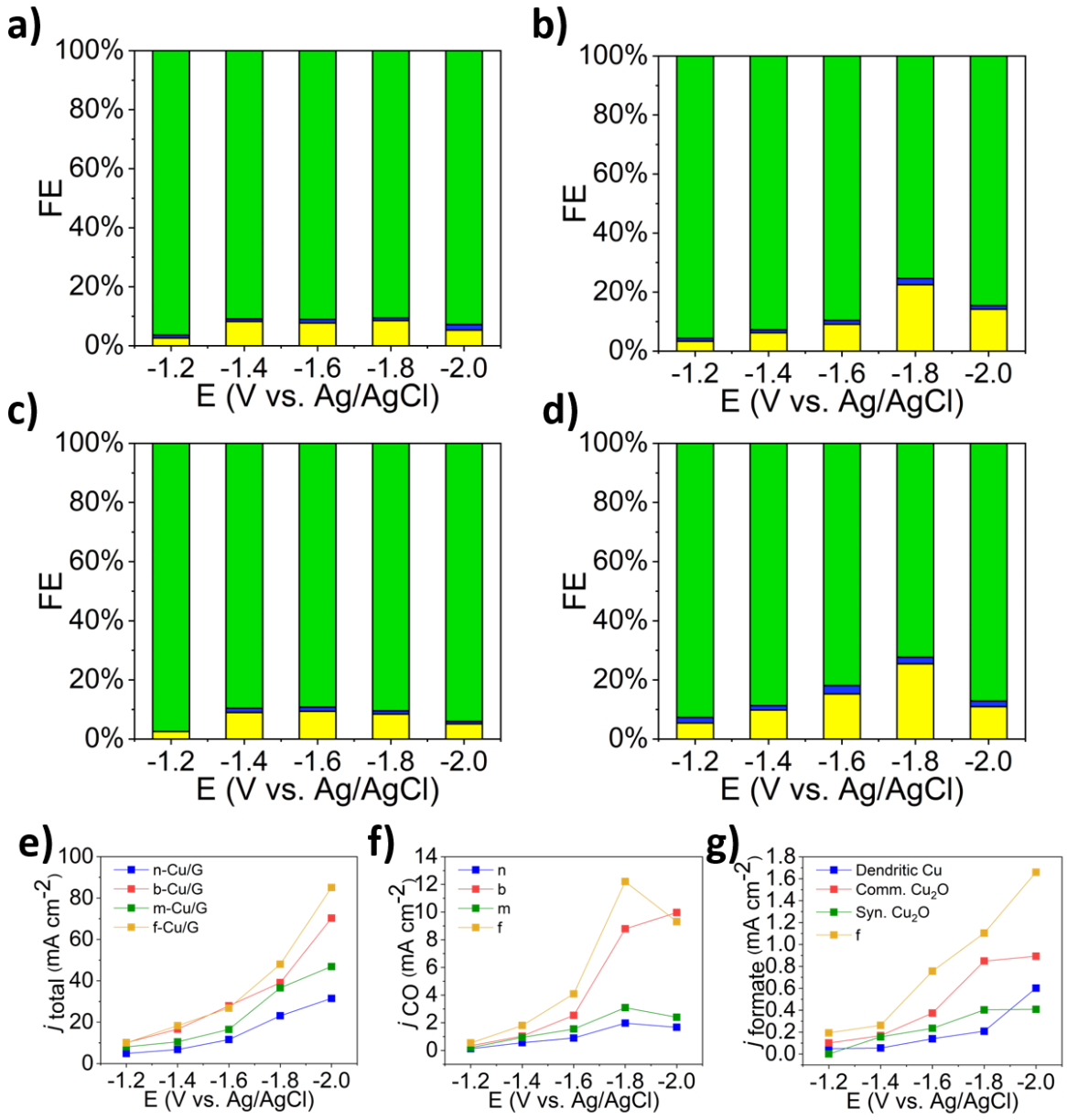

Figure 4.13 Faradaic efficiency profiles of CP-cell using a) n-Cu_xO_y/Graphene, b) b-Cu_xO_y/Graphene, c) m-Cu_xO_y/Graphene d) f-Cu_xO_y/Graphene catalyst in 0.5 M $KHCO_3$ electrolyte of eCO_2RR with products including CO (yellow, bottom), Formate (blue, middle), H_2 (green, top); d) Total current density, e) Current density of CO and f) Current density of formate for results in a-c.

The HER domains the overall reaction and the catalysts present a low activity for eCO_2RR. Here graphene plays an important role as an efficient HER catalyst which boosts the hydrogen production[196]. Moreover, HER is happened at lower overpotential (-0.41 V vs. SHE) compared with carbonaceous products such as CO (-0.52 V vs. SHE) and formate (-0.61 V vs. SHE)[77], therefore HER is triggered rather than eCO_2RR. Among Cu_xO_y/graphene catalysts, the f-Cu_xO_y/Graphene shows the highest FE values as shown in Fig 4.13d. Its FEs of CO at potentials

from -1.2 V to -2.0 V vs. Ag/AgCl, are 5.43%, 9.84%, 15.26%, 25.42%, 10.94%. FEs of formate at potentials from -1.2 V to -2.0 V vs. Ag/AgCl, are 1.93%, 1.43%, 2.82%, 2.30%, 1.95%. However, the FEs are much lower compared with those of the synthesized Cu_2O (Fig. 4.8c). All detailed data is available in Appendix 3.

4.3.6 Characterization of Catalysts before/after eCO_2RR

In order to further reveal the catalyst behaviour in eCO_2RR, we have performed EDS dot-mapping after the overall reaction, in order to analyse the electrochemical corrosion and elemental distributions of Cu_xO_y/Graphene catalysts. Meanwhile, XRD was used to analyse the crystal structure of synthesized Cu_xO_y/Graphene catalysts.

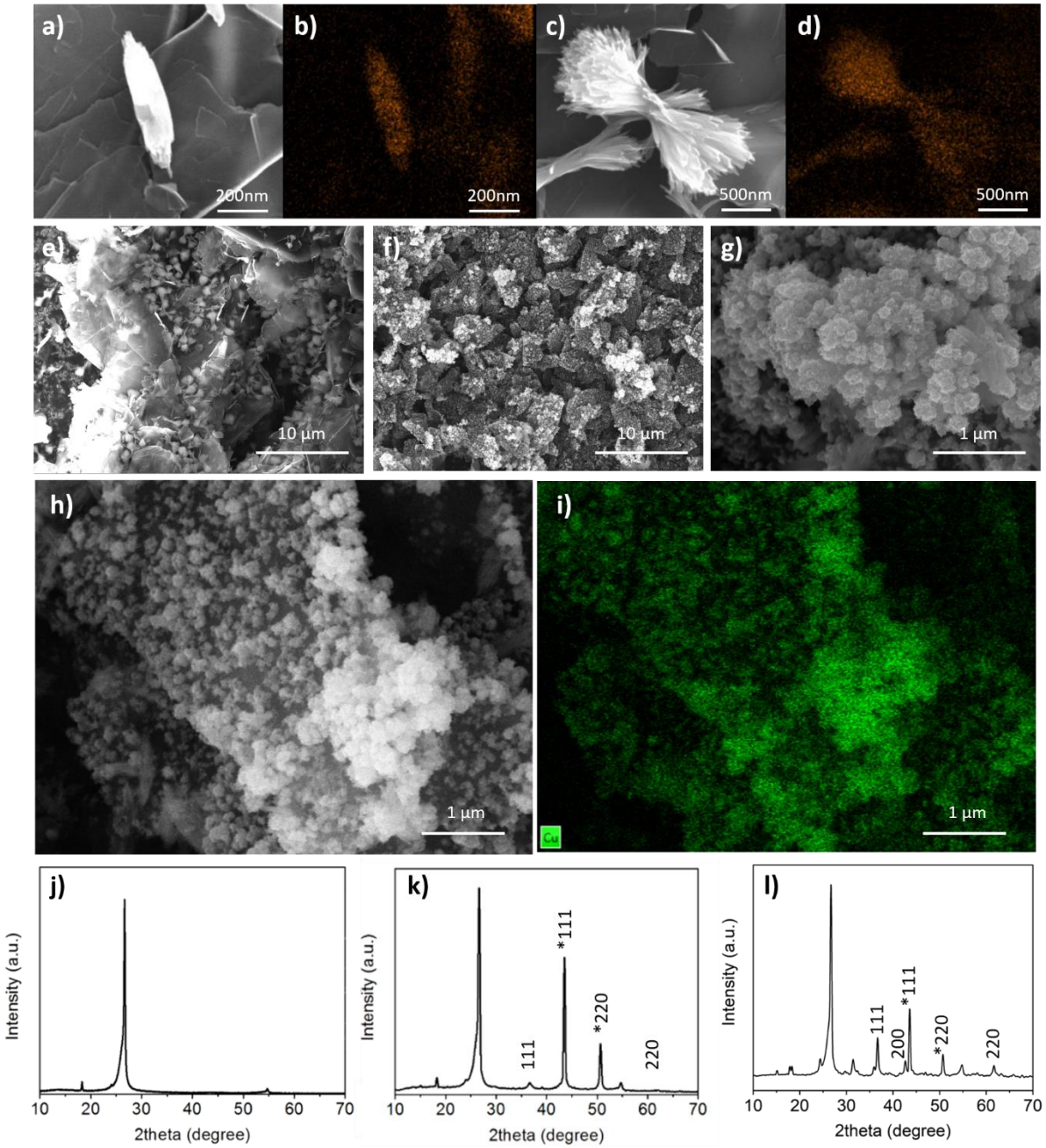

Figure 4.14 SEM/EDS dot-mapping (Cu element distribution) of a&b) n-Cu_xO_y/Graphene, c&d) f-Cu_xO_y/Graphene before eCO_2RR. SEM of f-Cu_xO_y/Graphene catalyst e) before and f-h) after 1000 s reaction of eCO_2RR, at -1.8V vs. Ag/AgCl. i) EDS mapping (Cu element distribution) of f-Cu_xO_y/Graphene after eCO_2RR. XRD patterns of j) blank carbon paper k) f-Cu_xO_y/Graphene loaded carbon paper

The EDS dot-mappings of n-Cu_xO_y/Graphene and f- Cu_xO_y/Graphene are shows in Figs 4.14a-d, where the observed white particles are Cu. The catalysis corrosion behaviour happens during reaction can be observed in Figs. 4.14 e-g. Before the eCO_2RR, the f-Cu_xO_y/Graphene catalyst

was loaded onto the 2D graphene surface forming nano-flower shaped particles. While after 1000 s of the electrochemical reaction, the nano flowers were turned into bulk particles. Therefore their surface areas and active sites are reduced, which could lower the catalyst activity for electrochemical reactions.

The XRD analysis of the carbon paper was done first and the results is shown in Fig. 4.14j as a reference. The XRD pattern of catalyst loaded carbon paper is shown in Fig. 4.14k, which exhibits characteristic diffraction peaks of Cu_2O (Cu_2O (111) at 2θ of 37º, Cu_2O (220) at 2θ of 62º), and minors mixture of Cu (Cu (111)* at 2θ of 43º, Cu (220)* at 2θ of 74º). After reactions, the intensities of Cu_2O peaks are decreased, and those of Cu peaks are increased. It means the Cu_2O was partially reduced into Cu. Therefore, it can be concluded that Cu_xO_y/Graphene catalyst has lost its nano-flower shapes and are partially changed its crystal type after one-hour eCO_2RR, which could reduce its catalyst properties for eCO_2RR.

4.4 Conclusion

In this study, several Cu-contained catalysts have been developed using two different cells, and different concentration of electrolytes were studied. According to the experimental results, the influence of catalyst and mass transfer of CO_2 can be concluded.

The results suggested that CP-cell with CO_2 supplied through gas diffusion presents a higher selectivity for carbonaceous products and the suppression of HER compared to H-cell with CO_2 purging into electrolyte. Higher concentration of electrolyte could enhance the reaction activity for a certain degree, while it can only promote the HER if CO_2 is insufficient.

All catalysts present a low activity for eCO_2RR in H-cell. Dendritic one presents a moderate activity on formation of formate in CP-cell, while the HER domains the overall reaction. Commercial Cu_2O present relevantly low activity in all tests due to its low surface aera compared with other two catalysts.

Synthesized Cu_2O shows its considerable selectivity and activity on CO products. This is mainly due to its nano-sized particles with large surface areas, which supplies sufficient active sites for eCO_2RR. Meanwhile, its specific crystal structure supressed the HER, thus enhanced the reaction efficiency of CO. By combining synthesized Cu_2O with GDE type cell, the FE of CO can be up to 61.31% at -2.0 V vs Ag/AgCl in 1 M $KHCO_3$. The results are promising for further development and scale-up.

We also used the graphene as substrate aims to enhance the catalyst activity and selectivity for eCO_2RR. However, from the results, the graphene promotes the HER reaction rather than eCO_2RR and results in a poor catalyst performance of carbonaceous products. Further development is necessary such as enhancing the loading of Cu on graphene, which could enhance the active sites. Find a way to eliminate the HER, such as using high concentrated electrolyte to reduce the H^+ in electrolyte can also be considered. Other method includes to promote the CO_2 mass transfer and enhance the eCO_2RR behaviour.

Chapter 5 ATO, ITO and In-MOF as catalysts for eCO_2RR

Several electrocatalysts with two different reaction cells for eCO_2RR were investigated in Chapter 4. Results suggested that analysis using the CP-cell presents the best electrochemical performance with considerable FE of CO. Formate is another high-value added product in eCO_2RR, and is commonly used in industries, such as tanning industry, textiles industry, pharmaceutical industry and rubber processing industry[76, 197]. Formate can also be used in direct formate fuel cells as a feed stock of renewable energy for electricity production[198]. Based on this, we researched a reaction system with commercial nano-sized ATO, ITO, and advance-structured In-MOF (collaboration with Manchester University) as electrocatalyst, aiming to establish a high yield reaction system for formate product.

5.1 Introduction

In 1985, Hori *et al.*[73] investigated the electrochemical reduction of CO_2 using various metal sheets at constant current scanning (Chronopotentiometry, 5 $mA \cdot cm^{-2}$) in 0.5 M $KHCO_3$ for 30 to 60 min. Among the results, Sn and In electrodes present considerable FE of formate (Sn: 65.5 – 79.5 % at -1.40 ± 0.04 V vs. SHE, In: 92.7 to 97.6% at -1.51 ± 0.05 V vs. SHE), which are the most active catalysts towards eCO_2RR in aqueous electrolytes for formate products. They also have high overpotentials for HER, and negligible CO adsorption[124], which show great potentials to achieve a high FE of formate production electrochemically. However, several challenges remain for these catalysts. For Sn, it is observed that organometallic complexes were formed on the electrode surface during the eCO_2RR, which promoted the HER and led to the declined FE of eCO_2RR[199]. The low durability of this catalyst also needs

consideration for further improvement. For In, the electrochemical results of pure In_2O_3 nanoparticles present a low current density of less than 30 mA•cm^{-2}, because the CO_2 conversion is hindered by its low catalyst activity[200]. A Sb-containing catalyst was reported by Li *et al.*[201]. They developed a sandwiched Sb nanosheet mixed in graphene for eCO_2RR, and obtained 88.5% FE of formate at a potential of -0.96 V vs. RHE. However, the current density achieved was only 8 mA•cm^{-2}. Meanwhile, they also demonstrated that the bulk Sb present a low current density less than 2 mA•cm^{-2}.

In order to overcome these drawbacks of monometallic and mono metal oxide catalysts during eCO_2RR, here we employed two bi-metal oxide catalysts for eCO_2RR, including ATO and ITO. ATO and ITO are widely used to produce solar panel, TV/monitor display coatings etc. Their nanosized ones are promising materials which are reported in solar cells enzymatic fuel cell[202], sensors[203], water electrolyser[204] and direct methanol fuel cell[205] etc. However, they have not been reported for applications in eCO_2RR. Meanwhile, In, Sn and Sb all have a good selectivity of formate, thus ATO and ITO have the potentials to have good performance towards eCO_2RR.

As In shows active eCO_2RR performance, we tested an In-MOF with a porous three-dimensional framework structure in eCO_2RR. They were reported to have high adsorption and selectivity towards CO_2, therefore promoting the activation and conversion for eCO_2RR[206]. However, In-MOFs present poor electrical conductivity in an aqueous condition[207], which results a low current density and thus a low reaction efficiency. Therefore, in this chapter, carbon black was added in In-MOF with the propose of enhancing its conductivity.

Finally, we considered the influence of pH of the electrolyte. The electrolyte for eCO_2RR is a crucial part and influences the whole system and the results of eCO_2RR[208]. A high pH alkaline

electrolyte has its advantages in eCO_2RR. Its hydroxide ions (OH^-) plays an important role in modulating active catalytic active sites as reported by Dinh *et al.*[209]. It can also supress the HER because of slow kinetics of the Volmer step, thus lowering the H^+ absorption and influencing the subsequent Tafel and Heyrovsky steps[124, 210].

Volmer step: $$H^+ + 1e^- + M \rightarrow MH_{ad}$$ Eq. 5.1

Tafel step: $$MH_{ad} \rightarrow 2M + H_2(\mathrm{g})$$ Eq. 5.2

Heyrovsky step: $$H^+ + 1e^- + MH_{ad} \rightarrow M + H_2(\mathrm{g})$$ Eq. 5.3

Here M is the surface metal active sites. However, a high pH electrolyte is not acceptable in the conventional H-cell, where CO_2 dissolved in a high-pH electrolyte will rapidly react, forming a neutral-pH carbonate mixture. In contrast, in a GDE cell, CO_2 diffuses directly to catalyst surface for reaction before it is converted into carbonate. Therefore, the GDE cell make it possible for eCO_2RR to occur in alkaline conditions[209]. In order to evaluate the pH effect as illustrate above, 1 M KOH alkaline solution was employed for electrochemical evaluation.

5.2 Electrochemical Evaluation of ATO

5.2.1 Working Electrode Assembly

20 mg ATO powder was placed into 2 mL vial and 500 µL isopropanol was added into the vial. Then the vial was sonicated in an ultrasonic sound bath for 10 mins. 40 µl (10% wt.) Nafion® solution (5%) was then added into the vial and further sonicated for 1 h. Then the ink was brush painted onto a carbon paper with an effective area of 2 cm^2. The loading of ATO catalyst (Δm) is 5 $mg \cdot cm^{-2}$.

5.2.2 Electrochemical Apparatus Setup

The performance of ATO catalyst was evaluated in both the H-cell and CP-cell. 0.5 M $KHCO_3$ and 1 M $KHCO_3$ were employed as catholyte and anolyte, respectively. The reference electrode was RE-61AP (ARE, BASI) in catholyte, and the counter electrode was Pt wire mounted in anolyte. The pH value of 0.5 M $KHCO_3$ electrolyte was 9.04, and the conversion to E_{RHE} can be calculated from:

$$E_{RHE} = E_{ARE} + 0.65\,V \qquad \text{Eq. 5.4}$$

The catalyst assembled with two cells were firstly CV scanned at potential range from -1.0 V to 1.0 V vs. RHE at 50 $mV \cdot s^{-1}$ scan rate under N_2 and CO_2 condition (one electrode scanned in N_2 and then CO_2). Then the systems were tested using CA at -0.4 V, -0.6 V, -0.8 V, -1.0 V and -1.2 V vs. RHE for 1000 s at each potential. Each time when the CA scan was finished, the catholyte was removed and collected, then new catholyte (0.5 M $KHCO_3$) was added for the next testing. The gas products were collected using a gas bag from the outlet of cell, then the catholyte was collected after reaction and sent to IC for liquid products analysis. The CO_2 gas flow rate was controlled with a value of 15 $mL \cdot min^{-1}$. Electrochemical evaluation has also been conducted in 1 M KOH as catholyte, and the results will be shown in Chapter 7.

5.2.3 Results and Analysis

The catalyst performance was evaluated using CV in CP-cell, and the results are shown in Fig. 5.1a. From the results, a reduction peak of ATO can be found at a potential of -0.3 V vs. RHE under N_2 atmosphere. It is noticeable that the current density value in N_2 has reached to 80 $mA \cdot cm^{-2}$, which is higher than the current density in CO_2 (~60 $mA \cdot cm^{-2}$). The HER happens under N_2 atmosphere which increases the current density, whereas less HER reaction happens under CO_2, because the existence of CO_2 could supress the HER. The onset potential of the

reaction is -0.15 V vs. RHE. The current density of ATO electrode under CO_2 is 60.7 mA•cm^{-2} which is much higher than those of any pure Sb or Sn reported so far. The high current density is attributed from the following reasons. (1). The nanosized catalyst induces large surface areas with abundant surface-active sites; and (2). HER happens and contributes the current density.

In order to study its selectivity and activity of formate, CA scanning and products analysis were further performed. After CV evaluation, the catalyst was assembled in H-cell and CP-cell for CA scanning. The results show a >17 folds FE difference between H-cell and CP-cell, as demonstrated in Figs. 5.1b-d. In H-cell, HER dominates the reaction, and only a small amount of carbonaceous products were detected (Fig. 5.1d). The reason for the low FE of carbonaceous products is due to its poor CO_2 mass transfer caused by the low CO_2 solubility in electrolyte. The dissolved CO_2 was easily reacted and consumed by alkaline electrolyte. Looking at the current density, the H-cell presents a high total current density (Fig. 5.1d), while its current densities of formate generation (Fig. 5.1c) is less than 15 mA•cm^{-2}. In the CP-cell (Fig. 5.1b), an enhanced mass transfer results in a high FE of formate at potentials from -0.4 V to -1.2 V vs. RHE, which the FEs are 35.10%, 47.99%, 51.11%, 52.98%, 56.76%. The current densities of formate in CP-cell are shown in Fig. 5.1c, which are 7.1 mA•cm^{-2}, 16.8 mA•cm^{-2}, 21.5 mA•cm^{-2}, 34.8 mA•cm^{-2}, 51.1 mA•cm^{-2}. The results of CP-cell confirm that ATO is active towards eCO_2RR due to the presence of antimony oxide and tin oxide. Its nanostructure provides more active sites and lower resistance, thus higher current density of formate (Fig. 5.1c) has achieved. Meanwhile, comparing with the data in H-cell and CP-cell, the results again prove that the enhancement of CO_2 mass transfer can benefit the overall FE of carbonaceous products and supress the HER. By combining the advanced electrochemical CP-cell with a good electro-catalyst, a high reaction activity, high FE and high selectivity reaction system can be established. The detailed data is available in Appendix 4.1.

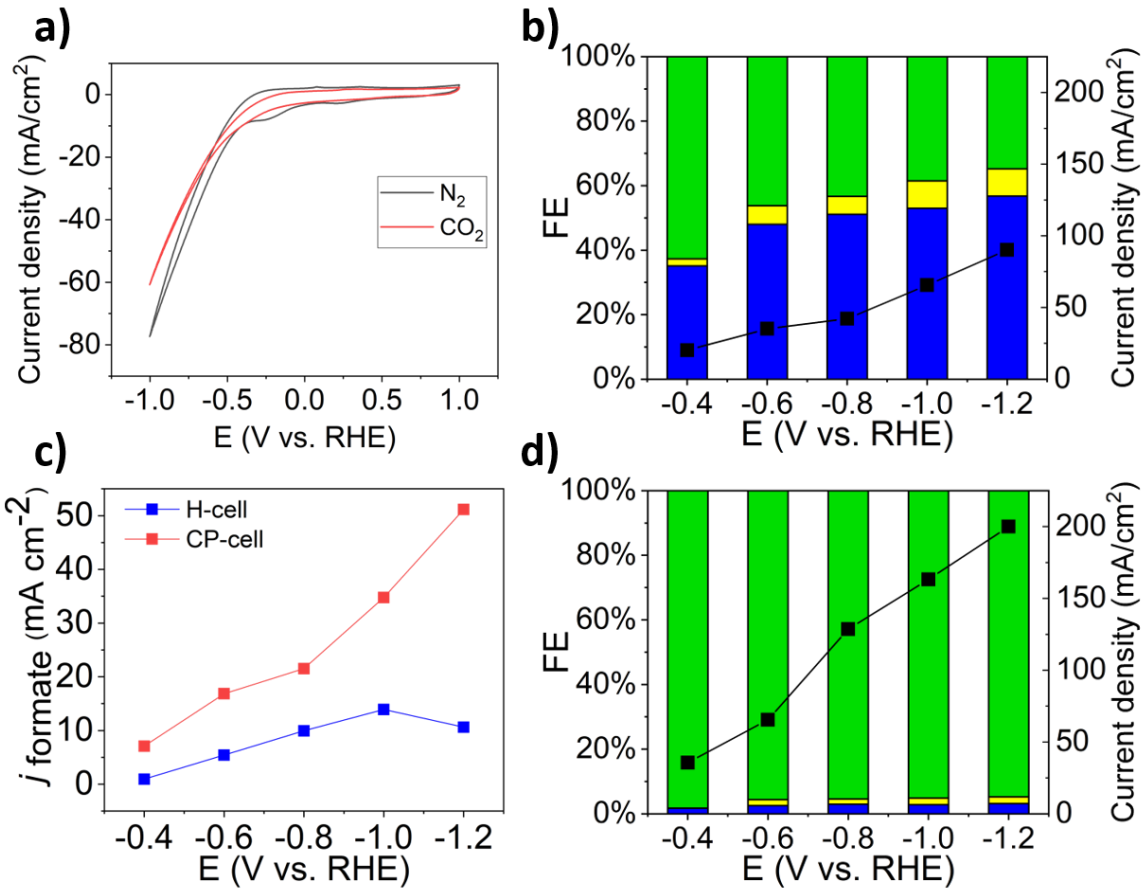

Figure 5.1 a) CV results of ATO in CP-cell, at potential scan from -1.0 V to 1.0 V vs. RHE in 0.5 M $KHCO_3$. FE profiles of b) CP-cell and d) H-cell using ATO catalyst in 0.5 M $KHCO_3$ electrolyte, with products including CO (yellow), Formate (blue), H_2 (green). d) Total current density for results in b and d.

However, it is noticeable that the FEs of formate in CP-cell is lower than the reported results (normally > 70%[73, 201]) by Hori *et al.* and Li *et al.* From my results, the FE of HER is 62.69%, 46.24%, 43.33%, 38.55%, 34.78% in CP-cell, which consumes a large proportion of electrons. Therefore, an effective way to supress HER is necessary. Due to this reason, we designed a GACP-cell which can prevent water penetration through the CP electrode. Details are shown in Chapter 7.

5.3 Electrochemical Evaluation of ITO

5.3.1 Electrochemical Setup

We then evaluated ITO for eCO_2RR. We prepared ITO ink as the catalyst using the same method detailed in Section 5.2.1, and the ink was printed on a piece of carbon paper GDL. The CP-cell was again employed to evaluate its electrochemical performance. Various electrolytes including 1 M $KHCO_3$ and 1 M KOH were employed as catholyte, and 5 M KOH was used as anolyte. High pH electrolytes were used aiming to supress the HER. The reference electrode was RE-61AP (ARE, BASI) in catholyte because this is a particular type reference electrode which was designed for strong alkaline environment, and the counter electrode was Pt wire injected in anolyte.

Firstly, CV measurement of ITO was evaluated in a CP-cell at potential from -1.0 V to 1.0 V vs. RHE with a scan rate of 50 $mV•s^{-1}$. The electrolyte was purged by N_2 for 30 minutes, and then a CV scan under N_2 environment was performed. Then CO_2 was purged for 30 minutes, then another CV was performed with a constant supply of CO_2 at a flow rate of 15 $mL•min^{-1}$. Next, the eCO_2RR performance of catalysts were tested by CA measurement, at a specific potential range from -0.4 V to -1.2 V vs. RHE. Due to the main product of catalysts is formate, we collected the catholytes after each test, and the results were analysed using the IC.

5.3.2 Results and Analysis

CV results are shown in Fig. 5.2a. Under N_2 atmosphere, clear redox couple of peaks can be observed at potential range of -0.4 V and 0.2 V vs. RHE. Under CO_2 saturated atmosphere, while scanning toward negative potentials, a drastic increase in the current density was

observed at lower onset potentials (-0.4 V vs. RHE), thus reaching a current density of approximately 50 mA•cm^{-2} at -1.0 V vs. RHE.

To further explore the electrochemical performance of ITO, CA measurement was performed using a CP-cell at potentials of -0.4 V -0.6 V, -0.8V, -1.0 V and -1.2 V vs. RHE holding for 1000 s in 1 M $KHCO_3$ and 1 M KOH catholyte. The FE results are shown in Fig 5.2b. The FE values of formate in 1 M $KHCO_3$ and 1 M KOH present similar results. The FE values of formate in 1 M $KHCO_3$ at potentials ranging from -0.4 V to -1.2 V vs. RHE are 9.53%, 57.32%, 64.54%, 56.02%, 67.54%. In 1 M KOH electrolyte, the FE of formate are 18.70%, 57.77%, 63.74%, 67.26%, 74.24%.

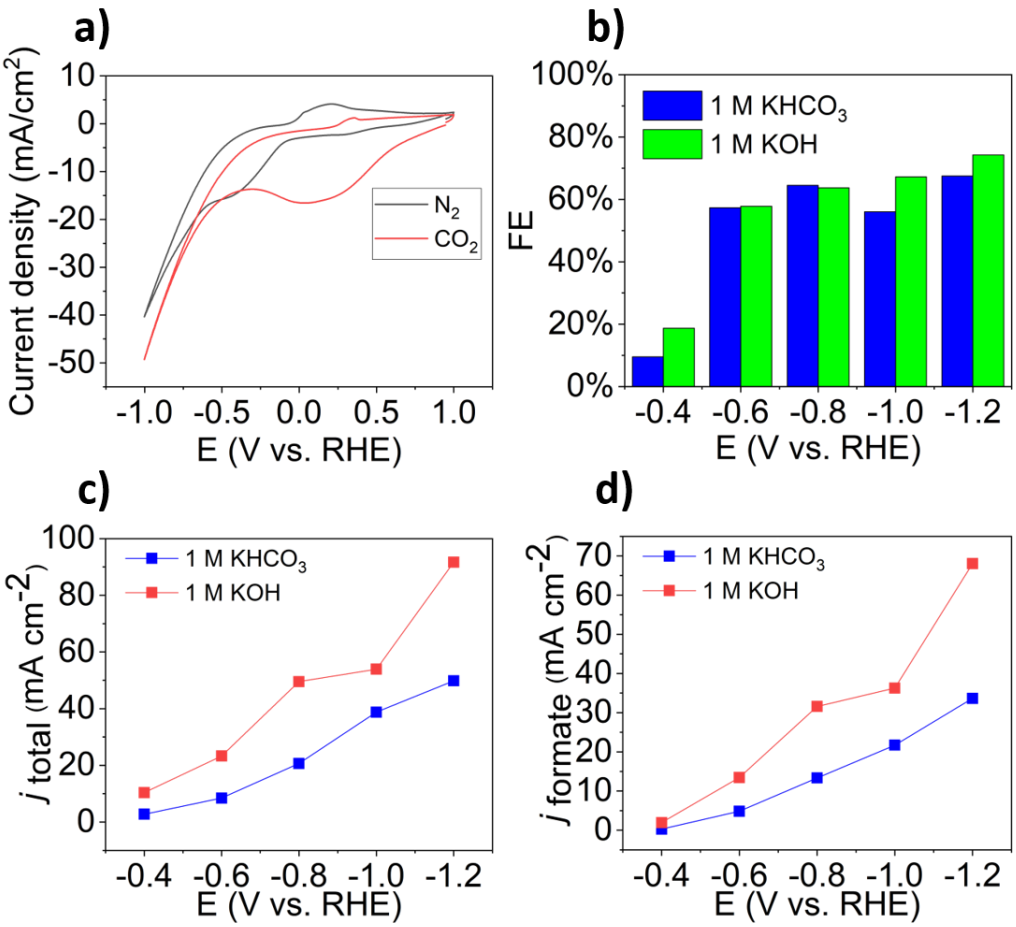

Figure 5.2 a) CV of ITO in 1 M $KHCO_3$, CP-cell; b) FE profiles of ITO in 1 M $KHCO_3$ (blue) and 1 M KOH (green) electrolyte of eCO_2RR with products of formate; c) Total current density, e) Current density of formate for results in b).

Comparing with 1 M $KHCO_3$ electrolyte, those at 1 M KOH electrolyte shows a higher reaction activity with higher total current density absolute values as shown in Fig. 5.2c. The reason of higher current density in the 1 M KOH is that the charge transfer resistance/electrolyte resistance is decreased with a higher concentration of hydroxide (OH^-)[111]. The results shown in Fig. 5.2d indicates that the current densities of formate in 1 M KOH is higher than in 1 M $KHCO_3$. All detailed data is available in Appendix 4.2.

In this section, we demonstrated ITO as electrocatalyst for eCO_2RR in CP-cell with two different electrolytes. From the results, a high value of FE of formate (74.24%) has achieved at potentials of -1.2 V vs. RHE in 1 M KOH, with highest current density (68.04 mA•cm^{-2}). The results also proved that a high pH electrolyte in GDE cells could improve the eCO_2RR performance to a certain degree by supressing HER. However, it still shows 30-50% FE towards HER. Therefore, future studies should be focused on high performance catalyst with ability of CO_2 adsorption, high porosity (more active sites), high product selectivity etc.

5.4 Electrochemical Evaluation of In-MOF

5.4.1 Ink Preparation of Electrode

In-MOF was obtained from Yang's group in Manchester University. To enhance the conductivity of MOF materials, carbon black (Vulcan® XC72R) was added in the In-MOF during the ink preparation. 16 mg In-MOF powder and 4 mg carbon black were placed into 2 mL vial and 500 µL isopropanol was added into the vial. Then the vial was sonicated for 10 mins. 40 µl (10% wt.) Nafion® solution (5%) was added into the vial and then further mixed for 1h. Then the ink was painted onto a carbon paper with an effective area of 2 cm^2. The

loading of overall MOF and carbon (Δm) was 5 mg•cm^{-2}, with the effective In-MOF loading of 4 mg•cm^{-2}.

5.4.2 Electrochemical Evaluation of In-MOF in $KHCO_3$ Electrolyte

The eCO_2RR performance of In-MOF was evaluated by CA. All detailed data is available in Appendix 4.3. In order to verify the electrolyte influence, we firstly employed 0.1 M, 0.5 M and 1 M $KHCO_3$ as catholyte in eCO_2RR. The FEs and current density at -0.4 V to -1.2 V vs. RHE are shown in Fig. 5.3.

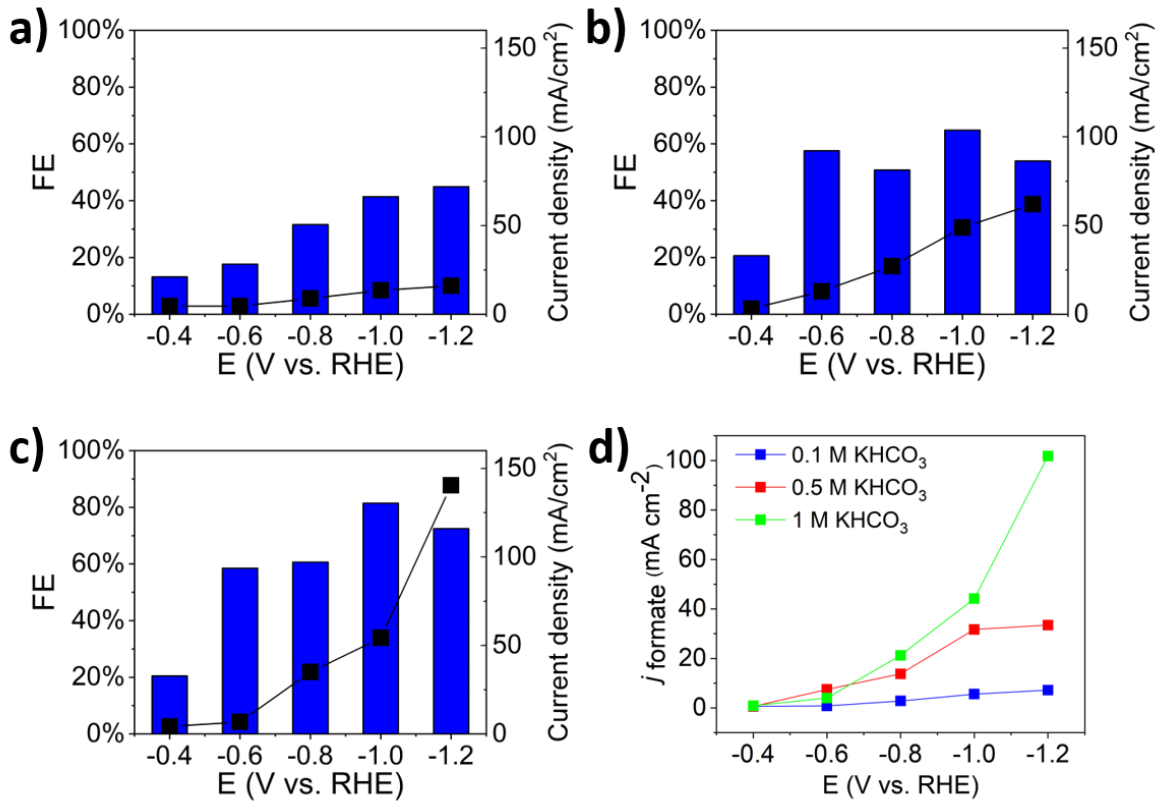

Figure 5.3 a) FEs and total current density of In MOF in a) 0.1 M $KHCO_3$, b) 0.5 M $KHCO_3$, c) 1 M $KHCO_3$ electrolyte of eCO_2RR with products of formate; c) Current density of formate for results in a-c.

The FE and current density results of In-MOF in 0.1 M $KHCO_3$ are shown in Fig. 5.3a, where the low concentration of electrolyte limits the proton mass transfer in electrolyte and results in

low current densities. The FE values are 13.17%, 17.65%, 31.55%, 41.41%, 44.90% at potentials ranging from -0.4 V to -1.2 V vs. RHE. Once the concentration of electrolyte was increased to 0.5 M, an increased current density at higher potentials was observed (Fig. 5.3b). The FE values in 0.5 M $KHCO_3$ are slightly higher towards formate, which are 20.64%, 57.57%, 50.81%, 64.84%, 53.99%, at potentials ranging from -0.4 V to -1.2 V vs. RHE. Fig 5.3c shows the results of FE and current density in 1 M $KHCO_3$, where the current density presents a dramatic increase at higher potentials in particular at -1.0 and -1.2 V vs. RHE. Moreover, the total current density at -1.2 V is three folds higher than the current density at -1.0 V, and the FEs are 20.48%, 58.51%, 60.67%, 81.45%, 72.46% at potentials ranging from -0.4 V to -1.2 V vs. RHE. From these results, it can be concluded that a higher concentration of electrolyte can enhance the proton transfer of reactants in the electrolyte at higher potentials and result in a less electrolyte resistance. Therefore, a higher reaction efficiency has been achieved.

According to the results above, higher concentrations of 2 M $KHCO_3$ and 0.1 M KOH with higher pH as electrolyte were chosen for further testing. The FE results in 2 M $KHCO_3$ are shown in Fig. 5.4a. A similar current density of formate in 1 M and 2 M $KHCO_3$ can be observed as shown in Fig 5.3d and Fig. 5.4c. However, the FE values of formate are 39.08%, 61.77%, 64.97%, 58.07%, 63.59%, at potentials ranging from -0.4 V to -1.2 V vs. RHE, which are lower than those in 1 M $KHCO_3$. It means although they have similar activities on producing of formate, the 2 M $KHCO_3$ presents a higher total current density than that of 1 M $KHCO_3$ at all tested potentials. This also indicates that HER has been enhanced in 2 M $KHCO_3$.

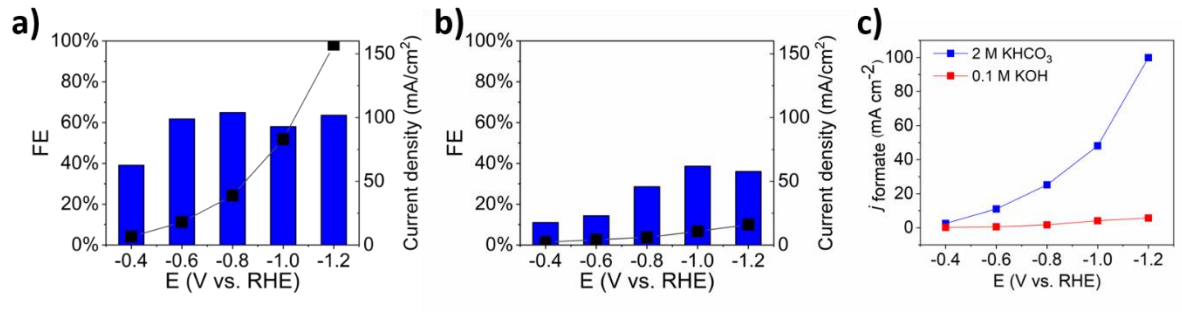

Figure 5.4 a) FEs and total current density of In MOF in a) 2 M $KHCO_3$, b) 0.1 M KOH electrolyte of eCO_2RR with product of formate; c) Current density of formate for results in a and b.

While in 0.1 M KOH, the results show relevantly low FEs and low current density (Fig. 5.4b). Because the MOFs are pH sensitive, the structures of In-MOFs were often damaged and their catalytic properties were vanished[211]. Therefore, a low performance of In-MOF was observed in 0.1 M KOH.

The durability test was conducted at the reaction condition which produces the highest FE. We performed the eCO_2RR at -1.0 V vs. RHE in CP-cell and 1 M $KHCO_3$ with a constant CO_2 supply with flow rate of 15 mL•min^{-1}, in order to analyse the stability of this reaction system. The experiment was proceeded for 1 hours first and then was paused to analysis the catholyte. After this, new 1 M $KHCO_3$ was injected inside the solution and the test was done for another 1 h. The total reaction time was 4 h.

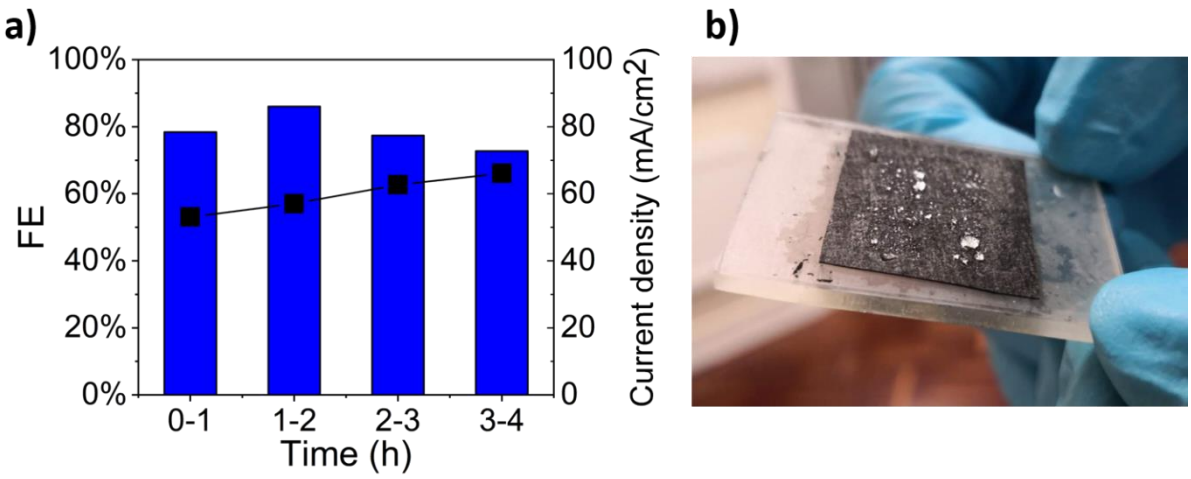

Figure 5.5 a) Stability test of In MOF in 1 M $KHCO_3$, CP-cell, 4 hours reaction. b) working electrode penetration after 4 h eCO_2RR

The stability test results are shown in Fig. 5.5a. The FE values of In-MOF in the first two hours are 82.41% and 83.02% at -1.0 V vs. RHE. After 2 h reaction, the FE values are slightly decreased to 79.40% (after 3 h reaction) and 76.76% (after 4 h reaction), which indicates that the In-MOF presents a good stability towards electrochemical testing in 1 m $KHCO_3$ electrolyte at -1.0 v VS. RHE. The slightly increased total current density shows that the decrease of FEs are mainly caused by HER, which is due to electrode permeation after a long-term reaction. Fig. 5.5b shows an image of the back of working electrode, where the electrolyte passed through the carbon paper formed as liquid drops. This caused much less areas of gas-liquid-solid three-phase interfaces, thus reduced the properties of eCO_2RR.

From the results above, a high value of FE of formate (83.02%) has achieved at potentials of -1.0 V vs. RHE in 1 M KOH, and the current density of formate was 47.4 $mA \cdot cm^{-2}$. The results also demonstrated that the electrolyte concentration influences the overall eCO_2RR. A low concentration of electrolyte could limit the proton transfer in electrolyte, thus limit the current density and lower the FE of formate.

5.5 Conclusion

In this chapter, results showed the increased FEs up to 56.76%, 74.24% and 83.02% towards formate production using ATO, ITO and In-MOF, which are higher than previously reported values in literature. For ATO, we introduced H-cell and CP-cell to evaluate the CO_2 mass transfer influence of eCO_2RR, where we proved that an efficient mass transfer of CO_2 can promote the FE of carbonaceous products, meanwhile supress the HER. For ITO, we considered the influence of pH in catholyte, and the results showed that a high pH value of electrolyte could reduce the H^+ in electrolyte, therefore suppressed the HER for a certain degree. For In-MOF, we studied the concentration of electrolyte, and concluded that increase of the concentration of electrolyte could promote the proton transfer, thus the better FE results were obtained. Moreover, nanostructured catalyst with more active sites (ATO, ITO) and advanced structed In-MOF enhanced the selectivity and activity of reaction, which is important for eCO_2RR.

Based on these concepts, we achieved the highest FE of formate up to 83.02% at -1.0 V vs. RHE by In-MOF, with a current density of 57.04 $mA \cdot cm^{-2}$. It has been proven that the selected nanoparticles perform well as eCO_2RR catalysts with relatively high FEs in our eCO_2RR reaction system. Both the ATO and ITO are readily available with relevantly low lost compared with novel metal catalyst. In-MOFs are easy to be synthesized. Therefore, they have great potentials for further scale up and commercialized.

Chapter 6 Graphene Aerogel - New Gas Diffusion Layer Exploration

6.1 Introduction

In Chapters 4 and 5, we have developed several electrocatalysts which have been tested using H-cell and CP-cell. We evaluated their electrochemical properties under different reaction condition and have discovered that a low CO_2 mass transfer in H-cell resulted high FE of H_2 generation from the HER which competes the eCO_2RR. We also obtained a high FE of desired products with minimised HER (below 40%) using the CP-cell. This is achieved with enhanced CO_2 mass transfer mechanism, in which CO_2 is diffused from the gas phase to catalyst layer surface rather than dissolved in the liquid electrolyte, and then transferred to the catalyst surface. However, HER still happens in all reactions in CP-cell, and an inhomogeneous CO_2 gas flow is often observed, mainly because the 2D structure of carbon paper could easily be penetrated by electrolyte and then the HER will be triggered. Therefore, a GDL with better electrochemical and mechanical properties is required.

GA is a group of carbon metamaterials with unique characteristics including large surface aera with tuneable porosity, good conductivity, ultralight weight and excellent organic solvent absorbency[145-149, 212]. Its 3D porous structure gives its potential to benefit the CO_2 mass transfer. In this chapter, we introduced the GA as GDL (Fig. 6.1), focused on evaluating the mechanical and electrochemical properties including conductivity, water-organic absorption ability, hydrophobicity, density and tensile test. We also synthesised a GA using graphene oxide aqueous solution and its morphology was observed by SEM.

Figure 6.1 GA used in our experiment

6.2 Preparation of the GA Electrode

GA was supplied by Gaoxi Technology Co., Ltd. Cu_2O nano particles show a good eCO_2RR performance as discussed in Chapter 4. Therefore, they are adopted as the catalyst and made as ink then loaded onto the surface of GA using spraying coating method (Section 3.8). The catalyst loading state will be checked on the GA surface.

6.3 Morphology of the GA and Electrode

Fig. 6.2 shows typical SEM images of GA. It can be seen from Fig 6.2a that the morphology of the aerogel is uniform in the large scale and exhibit a 3D network of randomly oriented sheet-like structures. It is rich in the hierarchical pores, and achieves an ultralow bulk density of $\approx$ 0.03 g•cm^{-3}, which is only $\approx$ 6.6% of that of carbon paper (0.44 g cm^{-3}, Toray TGPH-060) and $\approx$ 0.16% of that of graphite block ($\approx$ 1.82 g cm^{-3})[150]. In Fig. 6.2b, the catalysts agglomerates can be observed on the GA layer surface rather than a full homogenous coverage. In eCO_2RR, the exposed graphene layer could promote HER. Therefore, the catalyst directly supported on GA does not show any merit towards inhabitation of HER. According to this, we combined the carbon paper and GA into a hybrid GDL and designed a graphene aerogel-carbon paper GDE cell (GACP-cell) for eCO_2RR (all the details will be shown in Chapter 7).

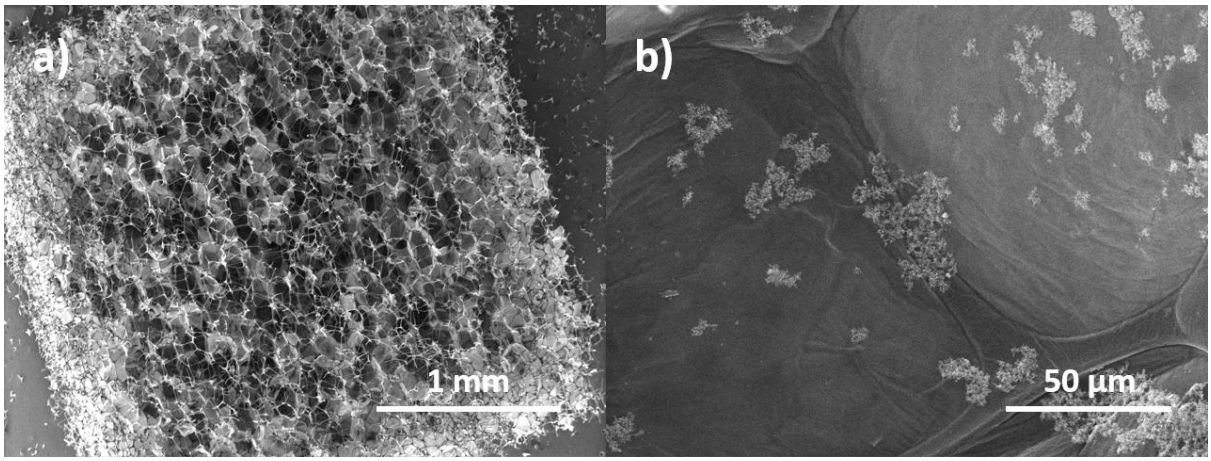

Figure 6.2 SEM scanning of GA, a) large scale scan b) Cu_2O catalyst supported GA layer

6.4 Conductivity

The conductivity of GA (without catalyst) was obtained from measuring the voltage and current using Autolab® potentiostat/galvanostat as shown in Figs. 6.3a and 6.3b. The clips were connected to the two ends of GA samples, then applied the potential range from 0 V to 0.2 V. A current vs. potential plot was collected by potentiostat and the conductivity of GA were calculated by Eq. 6.1.

$$\sigma = \frac{L}{R \times S} \qquad \text{Eq. 6.1}$$

In this equation, the resistance R and be calculated by linear fitting the current vs. potential plot, where the 1/R is the slope of the linear line. L is the sample length (distance between the clips), and the S is the cross section (blue square region shows in Fig. 6.3) of GA.

The result in Table 6.1 indicates a competitive conductivity of GA, if compared to those of the other commonly used electrodes and current collector materials, e.g., TGPH-060 carbon paper

and graphite block. Since the GAs are highly elastic, with a Young's module of 0.256 MPa, we also assessed the conductivity under mechanical compression. Interestingly, the conductivity of GA remained unchanged when we applied the compression strain along the longitudinal direction as shown in Fig. 6.3c, and along the horizontal direction as shown in Fig. 6.3d. Table 6.2 lists all the data of the conductivity.

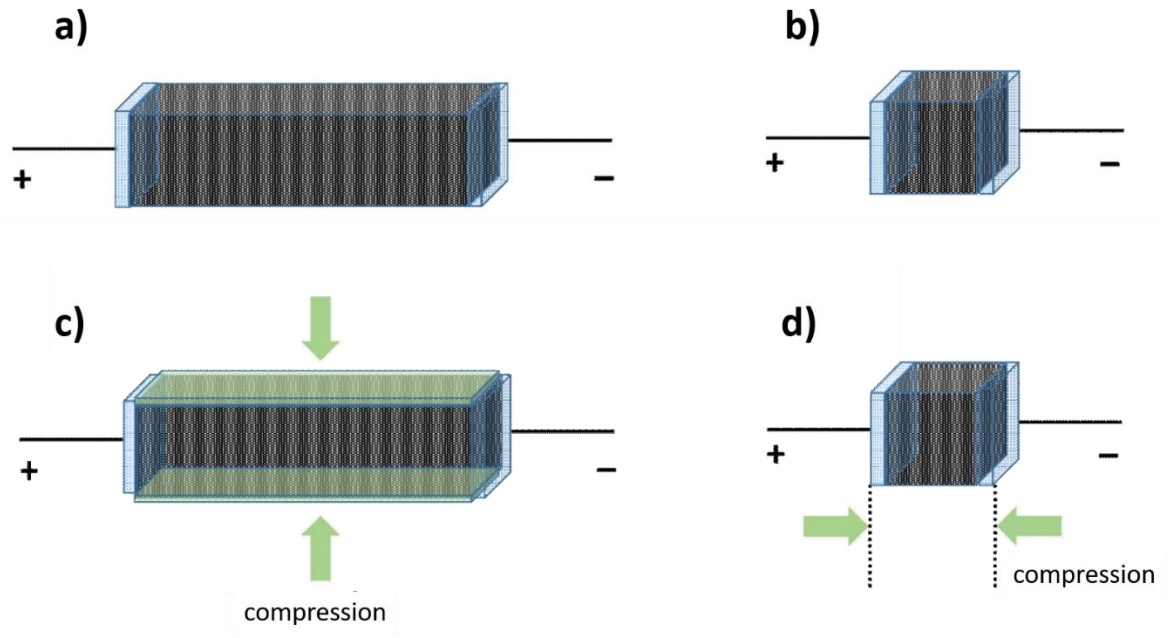

Figure 6.3 Scheme of conductivity test method, the cross-section area is 10 x 10 mm^2, the length of GA in test a) is 30 mm (to simulate in-plane), in test b) is 10 mm (to simulate through-plane). Conductivity test of GA under compression with different direction c) vertical compression, d) side compression, the conductivity data was analysed against the strain

Table 6.1 Conductivity of GA using the set-up in Fig. 6.3a and 6.3b, TGPH-060 carbon paper and graphite block (Fuel Cell Grade GM-10) are used as comparison.

	Method	Cross Section Area / mm^2	Length / mm	Conductivity / $S \cdot m^{-1}$
GA	a)	100	30	0.153
	b)	100	10	0.471
TGPH-060	a)	100	30	0.125
	b)	19	0.19	1.724
Graphite Block	a)	100	30	0.171
	b)	100	10	0.509

Table 6.2 Conductivity of GA under compression, using the set-up in Fig. 6.3c and 6.3d, result shows conductivity does not response with the strain

Method	GA Conductivity Response to Strain						
c)	Strain / %	0%	10%	20%	30%	40%	50%
	Conductivity / Sm^{-1}	0.15	0.15	0.15	0.15	0.16	0.16
d)	Strain / %	0%	10%	20%	30%	40%	50%
	Conductivity / Sm^{-1}	0.47	0.42	0.47	0.43	0.41	0.42

6.5 Self-Assembly Preparation Method for New Graphene Aerogel

The synthesis of GA was carried out using the methods as illustrated in Section 3.3.3. The synthesis steps are shown in Fig. 6.4. 60 mL of 4.0 $mg \bullet mL^{-1}$ graphene oxide aqueous solution and L-ascorbic acid was added into a 200 mL beaker (Fig. 6.4a), and sonicated for 2 hours (Fig. 6.4b). The mixture was placed in an oven at 40 ^{o}C for two days, and a graphene hydrogel was obtained as shown in Fig. 6.4c. Fig. 6.4d shows the graphene aerogel after freeze drying for one day, and there are highly porous structures observed on its surface after the hydrogel is fully dried. Fig. 6.4e shows the prepared graphene aerogel, which can stand itself on a piece of filter paper. The microstructure of GA from the SEM image is shown in Fig 6.4f, in which randomly oriented nanosheets of reduced graphene aerogel can be observed, with macropores between the nano layers. However, GA synthesized using the self-assembly method presents very low mechanical strength. It was easily crashed with a low compression strain applied, which is impossible to be utilize as GDL. Therefore, more research is required to synthesis GA with better properties.

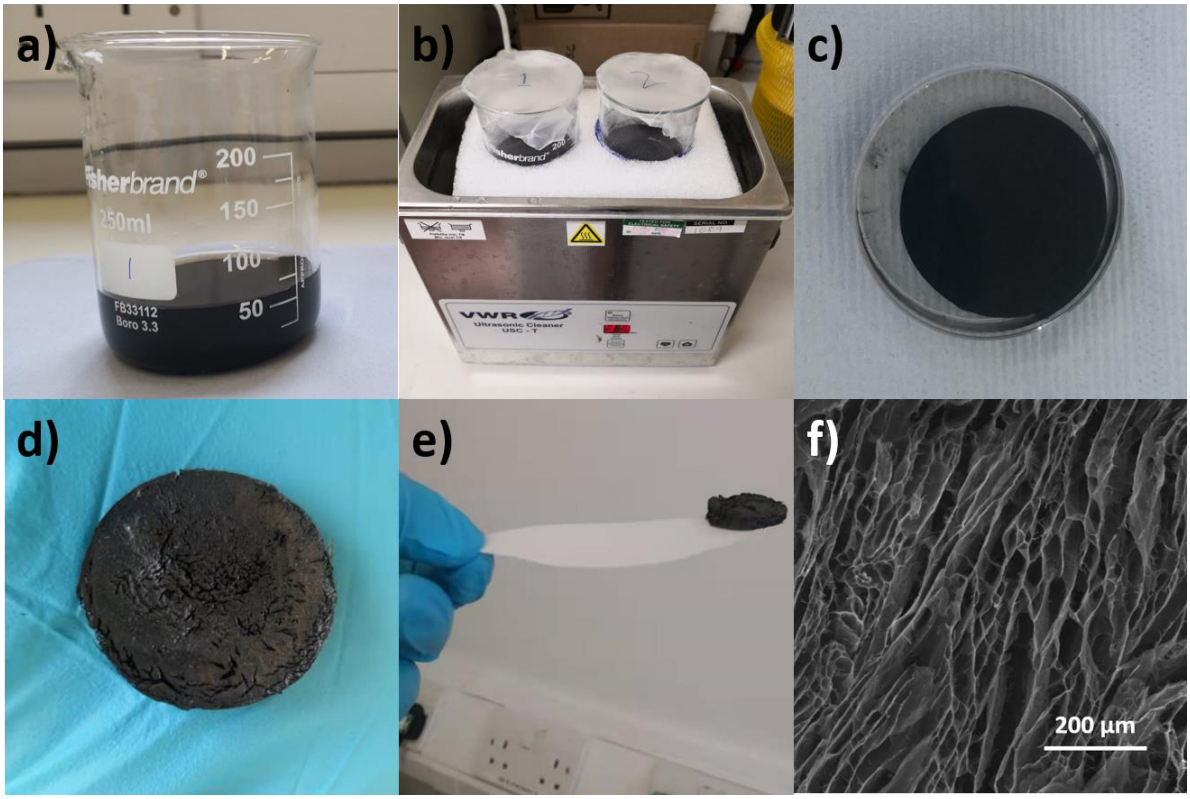

Figure 6.4 Synthesis of graphene aerogel. a) graphene oxide aqueous solution and L-ascorbic acid before reaction b) ultrasonic bath for GA preparation c) synthesized graphene hydrogel d) synthesized graphene aerogel e) graphene aerogel with ultra-low density supported on a filter paper f) SEM image of GA

6.6 Conclusion

In this chapter, we have discussed and evaluated several properties of GA, and demonstrated that the commercial GA have a high porosity and a good conductivity, which is a desired material for GDL. Based on this, we employed GA into GDE cell for eCO_2RR, which the cells design is demonstrated in Fig. 3.15 and 3.16, and its eCO_2RR properties will be studied in Chapter 7. We also tried to synthesize a GA by reducing graphene oxide, while its mechanical and chemical properties are not sufficient of being an electrode for eCO_2RR. Therefore, further research on GA synthesis is needed.

Chapter 7 Hybrid Gas Diffusion Electrode Allowing Directional Gas onto Catalyst Bed for Enhanced CO_2 Electrochemical Reduction

Comparing to the massive efforts in the innovation of catalyst material systems and technologies, structural design of cells has attracted less attentions on the road towards high performance eCO_2RR. Here, we propose a hybrid gas diffusion electrode-based reaction cell by using highly porous carbon paper and GA, which is expected to offer directional diffusion of gas molecules onto the catalyst bed and sustain a high CO_2 conversion performance. The above hypothesis has been approved by both the experimental and simulation results, which show that the Carbon paper + GA combined configuration increases the FE from ~60% to over 94% towards CO and formate production compared with a CP only cell. It also suppresses the undesirable side reaction - hydrogen evolution over 65 times than the conventional H-cell. By combining with advanced catalysts with high selectivity, a 100% FE of the cell with a high current density could be realised. This described strategy sheds a light on future development of eCO_2RR in structural manners.

7.1 Introduction

In this chapter, we introduce a porous bi-layer design with interface of two porous materials, with expectation to create alternative mass transfer by establishing the circulation/diffusion sub-cycle for improving the overall eCO_2RR performance. We firstly design and compare four types of electrochemical reactors (Fig. 3.11, 3.14-3.16), in which the first design is a compact H-cell (Fig. 3.11). Comparing with the conventional H-cell[175], this compact H-cell presents incremental optimization by suppling more areas for the working electrode but less spaces

between cathode and anode (ca. 1 cm). This can result in a lower electrolyte resistance (causing an overpotential) for electro-chemical behaviour[177]. This type of gas supply will inevitably enable poor CO_2 transfer caused by the low solubility of CO_2 in electrolyte[178], while hydrogen evolution reaction will also happen and reduce the CO_2 reduction efficiency[179]. Meanwhile, CO_2 supplying method based on the idea of 'bubbling into electrolyte' will be likely to occur to destabilize the system, where some CO_2 bubbles will stick on the surface of working electrode and block the pathway of proton transfer to the catalyst surface (Fig. 7.1). These will yield less electrode areas for reactions, thus leading to a significantly reduced current density.

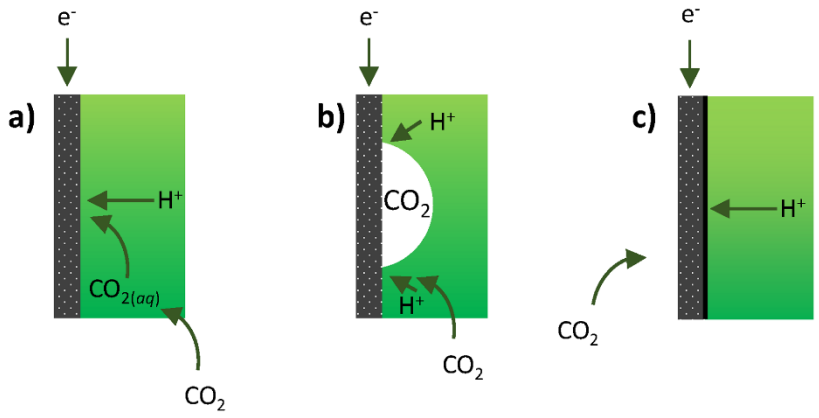

Figure 7.1 a) CO_2 transfer in aqueous phase by dissolving in electrolyte by H-type cell. b) purged CO_2 bubble block the catalyst surface by H-type cell c) CO_2 transfer through gas diffusion layer (GDL) by GDE type cell.

The core structure for the second design (CP-cell) is a conventional carbon paper based GDE which serves as a current collector and substrate to support the catalyst layer (Fig. 3.13a). The integrated CP-cell design is illustrated in Fig. 3.14, where the catalyst layer with an average thickness of 10 μm is homogenously facilitated on the CP surface (Fig. 7.2a). However, the structure of carbon paper will decay after a long-term reaction, and the permeation of water easily happen in this type of cell to trigger HER as well as the blockage of CO_2 mass transfer pathway. Additionally, an inhomogeneous CO_2 gas flow is often observed in carbon paper base GDE design.

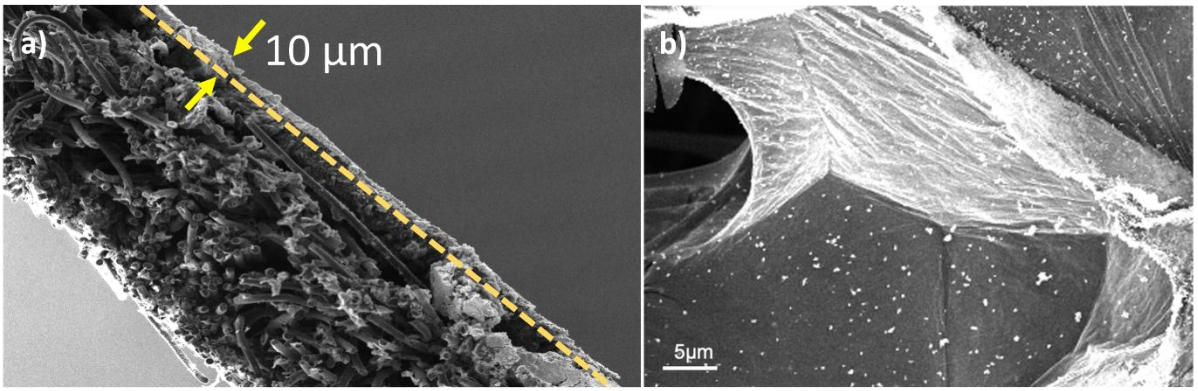

Figure 7.2 a) Cross-section view of bilayer with catalyst layer b) Catalyst on graphene aerogel

GA is a promising material that has been used as an electrode material for different scenarios, due to its bespoken porosity and stability. Our group has previously developed a direct methanol fuel cell (DMFC) technology with a higher mass power density by using GA to replace carbon paper[151]. The concept of GA GDE is introduced in the 3rd design (Fig. 3.13b) with an integrated cell design (GA-cell) shown in Fig. 3.15, where the GA is inserted in the chamber and allows CO_2 to diffuse within the highly porous GA rather than passing through the empty chamber. The high porosity from GA offers a large surface area and a considerably good conductivity ($\approx$10 S cm^{-1})[151], which make it a suitable alternative material as a catalyst substrate. Moreover, the 3D structure of GA could resist the permeation of electrolyte effectively. It should be noted that, the high roughness on GA's surface could be problematic during the coating process for catalyst, even at a higher loading of 5 mg•cm^{-2} or after surface treatment, thus leading to a coarse structure and exposing the GA to the electrolyte (Fig. 7.2b).

Next, we create a porous bi-layer design (GACP-cell) by combining GA (without catalyst) to the CP GDE. A schematic of this bi-layer GDE configuration and an integrated cell design are shown in Fig. 3.13c and Fig. 3.16, where an interface effect is expected to increase the mass transfer of CO_2 with a guided diffusion on the catalyst layer (Fig. 3.16c). We used 3D printing technique to create the parts with the design details of GACP-cell and then fully assemble of

the whole device. The GACP-cell consists of three chambers. The gas chamber in the left-hand side contains GA, where the CO_2 flows into gas chamber, diffuses through GA and then CP, and finally reaches to the catalyst layer. The middle chamber is filled with catholyte, where the cathode coated with catalyst is exposed to the catholyte, and a reference electrode is inserted in this chamber. The right chamber is the anode chamber with anolyte and the inserted counter electrode (Pt wire). A cation exchange membrane is placed between the anode and cathode chambers to allow H^+ to pass through. All the components with gaskets are firmly connected and sealed to ensure a good contact without any leakage**.** The whole cell was designed to reduce the electrolyte resistance.

Since the pore sizes in the carbon paper and graphene aerogel are more than 10 μm, the CO_2 mass transfer in these two media is through gas flow. When the CO_2 approaches to catalyst layer, there is a gas concentration gradient near the catalyst layer as result of gas diffusion, which can be predicted by the Fick's second law as a function of the gas concentration, distance and time[213].

$$\frac{\partial C}{\partial t} = D_a \frac{\partial^2 C}{\partial x^2} \qquad \text{Eq. 7.1}$$

where C is the CO_2 concentration ($mol \cdot L^{-3}$), t is time (s), D_a is the molecular diffusion coefficient in air ($L^2 \cdot s^{-1}$), and x is the distance along the axis of flow (L). Compared with the CP-cell, the GA cells provide a uniform CO_2 flow before the gas approach to catalyst layer. This will lead to a homogenously distributed and increased CO_2 molar concentration. Moreover, the interface between the CP and GA play a key role as the boundary for the gas transfer, where a sub-circulation of gas is expected to enhance the CO_2 gas diffusion and also prevent the water penetration.

7.2 Results and Discussion

To explore and compare the mass transfer for the designed cells, COMSOL® simulation (Detailed information in Appendix 5.1) of real time CO_2 molar concentrations along the cathode catalyst layer has been performed for the CP-cell, GA-cell and GACP-cell (Fig. 7.3). The simulation results are based on the following assumptions. (1). There is no inflationary effects of heating; (2). Sufficient CO_2 is supplied from the inlet; (3). CO_2 is reacted once reaches the catalyst layer; (4). The internal pressure will not cause membrane rupture.

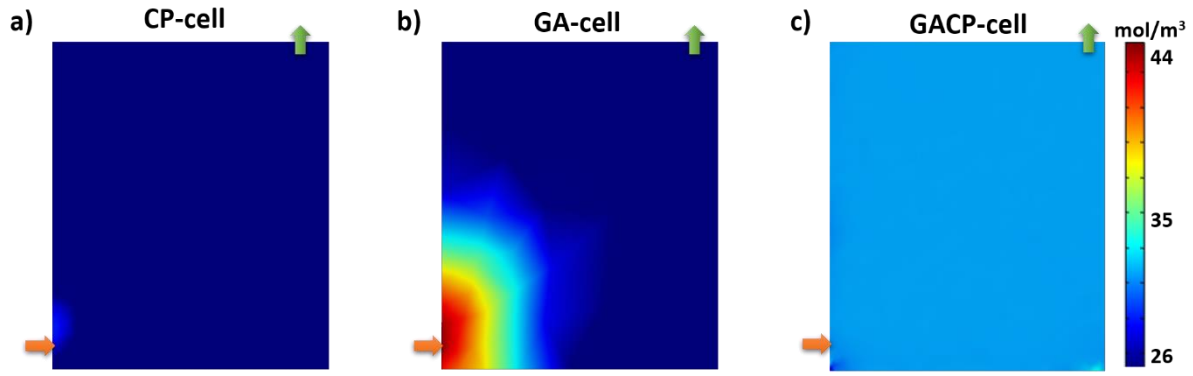

Figure 7.3 COMSOL® simulation on CO_2 molar concentration along the cathode catalyst layer for a) CP-cell b) GA-cell and c) GACP-cell

Detailed parameters, settings and conditions in the COMSOL simulations are listed in Tables S5.1 and S5.2. In the CP-cell (Fig. 7.3a), CO_2 molar concentration is generally lower than those of the other cells. The GA-cell (Fig. 7.3b) shows a high CO_2 molar concentration around the inlet with a fast decreasing gradient, and the rest of the electrode shows a nearly constant CO_2 molar concentration, which is slightly higher than that of the CP cell. The GA increases CO_2 gas diffusion within the electrode and slows down its speed when leaving the chamber. The gas flow is effectively enhanced in the GACP-cell, where the GA forms CO_2 feedstock supplies reactant more evenly through its body to the catalyst layer. A clear improvement in the uniformity of CO_2 molar concentrations along the electrode surface is obtained as shown in Fig. 7.3c, in which a homogeneous distribution is seen along all the electrode surface.

Abundant supply of reactant improves the mass transfer. As a consequence, a higher value of FE and a better eCO_2RR performance can be achieved.

The catalyst system used in this research are homemade Cu_2O and commercially available ATO nanoparticles. It was reported that the Cu_2O has a high electrocatalytic activity to produce CO with a high value of FE under ambient conditions[70, 214], and antimony oxide and tin oxide have good activity on generating formate[108,109]. Therefore, ATO is used in this study to assess high value of FE of formate for both gas and liquid productions. These catalysts were coated onto the surface of carbon paper with a loading of 5 mg•cm^{-2}.

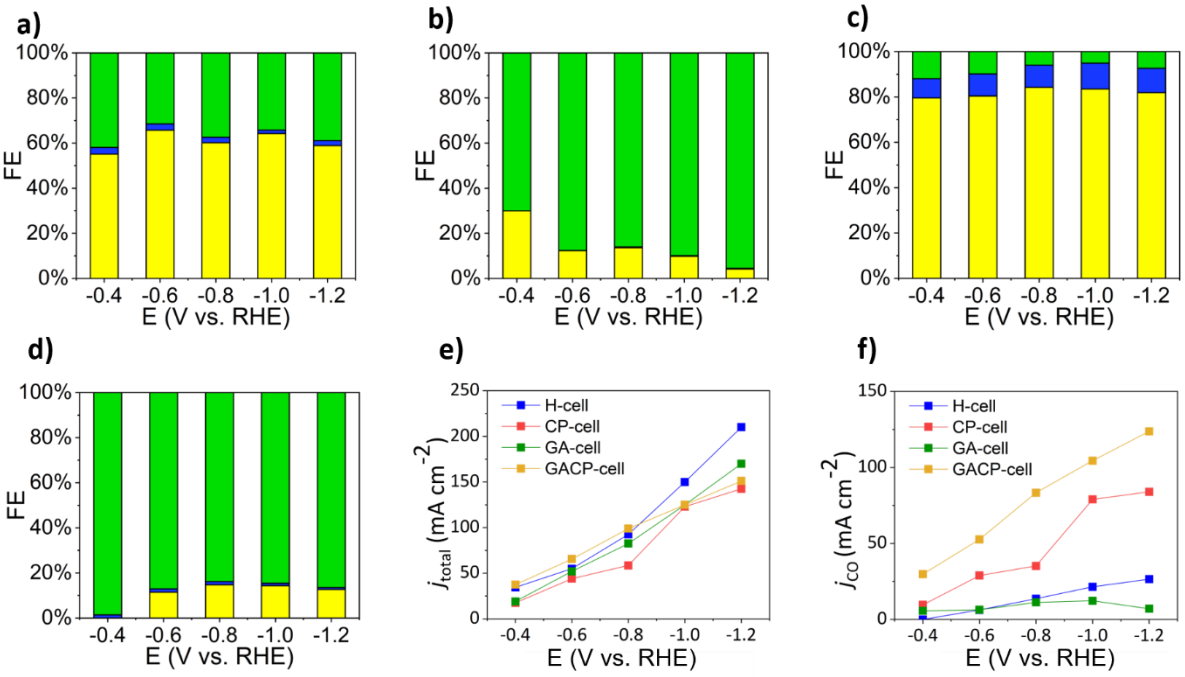

Figure 7.4 Faradaic efficiency profiles of a) CP-cell, b) GA-cell, c) GACP-cell and d) H-cell using Cu_2O catalyst in 1 M KOH electrolyte of eCO_2RR with products including CO (yellow, bottom), Formate (blue, middle), H_2 (green, top); e) Total current density; f) Current density of CO for results in a-d).

The FE results of CP-cell, GA-cell, GACP-cell and H-cell are shown in Figs. 7.4a-d (more data inputs for calculating FE and random errors are listed in Tables S5.3-S5.6), where the green bars represent H_2 generated from HER, yellow bars represent CO, and the blue bars represent

formate. The total current density and current density of CO generated from Autolab potentiostat are shown in Fig. 7.4e and 7.4f (more data inputs for calculating current density values and random errors are listed in Tables S5.7 and S5.8). It can be seen from Fig. 7.4d that the HER dominates the reaction in the H-cell, and only a small amount of CO and formate are produced at -0.4 V *vs*. RHE. At low potentials, the main product is hydrogen as the overpotential of HER in the alkaline environment is near to 0 V vs. RHE. There is an increase of FE value for the CO when increasing potential, but that of the formate remains unchanged. For the H-cell, in the aqueous media, CO_2 gas is dissolved in catholyte and form CO_2(aq.), which is then transferred from the catholyte to surface of the catalyst layer[111]. A low solubility will limit CO_2 supply and the HER will happen when there is absence of CO_2. This will lead to a low FE of carbonaceous products[179].

Increasing the solubility of CO_2 in electrolyte has been seen as one of the promising means to enhance CO_2 mass transfer in H-cell, in which CO_2 was supplied under high pressure and high temperature to address the solubility issues[111]. However, the non-ambient processing conditions may destabilise the system and are less feasible for scale-up application. A re-configuration of the liquid CO_2 supplying is desirable for mass transfer problem from above perspectives. Although the above solutions may improve the mass transfer by enhancing the solubility of CO_2, it is theoretically relied upon CO_2 in liquid phase devices for eCO_2RR. Therefore, the solubility issue cannot be easily solved. Besides, K^+ in electrolyte would be easily bound onto the electrode and prohibit CO_2 diffusion[111, 215], which leads to the overall reaction turning into water splitting.

The CP-cell shows a much higher FE value of CO than that of H-cell as shown in Fig. 7.4a. Its FE values of CO at potentials of -0.4 V, -0.6 V, -0.8 V, -1.0 V,-1.2 V, are 55.13%, 65.71%,

60.19%, 64.23%, 58.93%, and the FEs of formate at potentials of -0.4 V -0.6 V, -0.8 V, -1.0 V, -1.2 V, are 2.95%, 2.83%, 2.42%, 1.54%, and 2.19%, respectively. The decreased FE values towards HER are resulted from the minimised exposure of carbon paper and the creation of three phase boundaries which improve the CO_2 mass transfer. As shown in Fig 7.2a of the cross-sectional view of the CP GDE, the catalyst is formed a uniform layer with a thickness of 10 μm, and the CP was pre-treated with PTFE layer to block the water. In this configuration, the CO_2 gas can directly reach to the catalyst layer, thus overcoming the gas diffusion limitations in the electrolyte.

Among these three GDE type cells, the GA-cell presents the lowest FE value of formate as shown in Fig. 7.4b. A large amount of graphene is exposed while printed with the catalyst ink, and this results in an inhomogeneous catalyst layer. It can be seen in Fig. 7.2b, even with a high catalyst loading of 5 mg•cm^{-2}, there is still exposure of GA 'skeleton' (graphene) which takes part in HER. Moreover, the organic-friendly GA may absorb the formate and reduce its concentration, which can be detected in the IC test. The FE values of CO are 29.97%, 12.34%, 13.62%, 9.86%, 4.17% at potentials from -0.4 V to -1.2 V.

Once a plain GA is attached at the back of the CP GDE, the GACP-cell is constructed. In Fig. 7.4c, the FE values of CO are enhanced to 79.58%, 80.41%, 84.20%, 83.54%, 81.91% and the FE values of formate are increased to 8.47%, 9.73%, 9.81%, 11.35%, 10.73%, respectively, at -0.4 V to -1.2 V potentials for the GACP-cell. This new cell suppresses the FE values of H_2 from HER to 11.95%, 9.86%, 5.99%, 5.11%, 7.36%, at -0.4 V to -1.2 V, which is 11 times improvement compare to those of the H-cell. Compare with CP cell, GACP cell presents a higher current density (Fig. 7.4e) in the potential ranged from -0.4 V to -0.8 V vs. RHE, and the H-cell shows a higher current density at a larger negative potential. This shows the evidence

that the HER is dominated the reaction. From the current density of the desired product CO (Fig. 7.4f), it is obvious that the GACP-cell presents the highest current density for CO production. Such experimental results confirmed our prospective that the improvement in mass transfer induces a higher CO_2 molar concentration, and it also agrees well with the simulation results.

COMSOL® simulation results of over-potential (OP) distribution along the cathode catalyst layers for CP-cell, GA-cell and GACP-cell are presented in Fig. 7.5. All the results show a mixed distribution of the OP ranges from -0.2 V to 0 V. The HER occurs at OP near to 0 V. Generation of CO and formate from eCO_2RR provides the OPs of -0.11 V and -0.20 V vs. RHE (pH=7)[36], respectively. An increasing trend of the absolute value of OPs can be observed with the sequence order for the CP-cell, GA-cell then GACP-cell. This means a higher production of CO and formate for both the GA-cell and GAPC-cell which agrees well with our experimental results. However, the GA-cell shows a different profile for both results of CO_2 molar concentration and OP simulations, due to the unavailability of defining the exposure of graphene on GA during COMSOL® simulations.

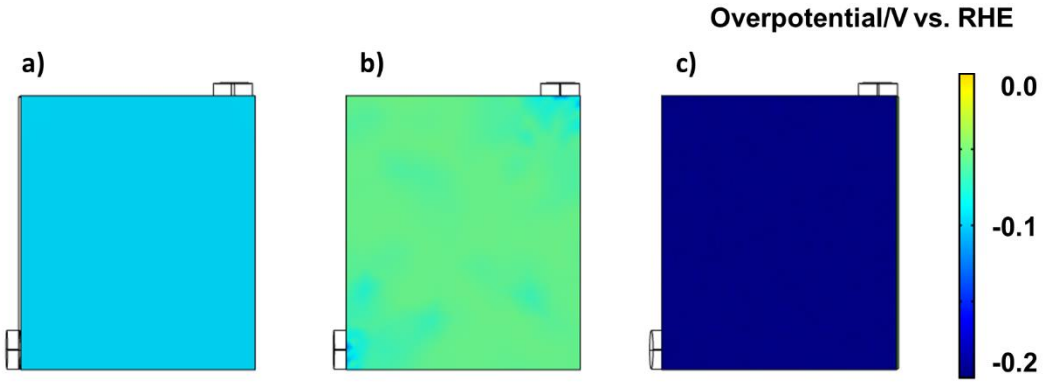

Figure 7.5 COMSOL simulation of overpotential distribution on catalyst surface for a) CP-cell, b) GA-cell and c) GACP-cell. The assumption of pH of the electrolyte is 7.

To analyse the stability of CP-cell and GACP-cell, we performed the eCO_2RR under -1.0 V vs. RHE in 1 M KOH with a constant CO_2 gas supply (15 $mL \cdot min^{-1}$). The durability test results for both these cells are shown in Fig. 7.6. The long-term experiment was proceeded for 4 hrs first and then it was paused to analysis the catholyte for liquid products. Then a new solution of 1 M KOH was added inside, and the reaction was continued for another 4 hrs. The tail gas was collected by gas bag to analyse the gaseous products during each 4 hrs electrochemical test. From the reaction efficiency CA diagram in Fig. 7.6a and the FE results shown in Fig. 7.6b, the FE values of CO are reduced from 63.28% to 22.93%, and the FE values of H_2 are increased from 34.92% to 75.53% at -1.0 V for the CP-cell. The FE values of CO are reduced from 83.36% to 79.27%, and FE value of H_2 increased from 5.74% to 12.50% at -1.0 V for the GACP-cell. It is found that the GACP-cell presents a better stability than the CP-cell, due to the homogenous distribution of CO_2 induced by porous bi-layer. Meanwhile, the catalyst layer is protected from peeling off from the carbon paper during the reaction, which leads to less carbon exposed to the electrolyte. GA also prevents the permeation of electrolyte through the GDL which leads the CP lost its GDE function.

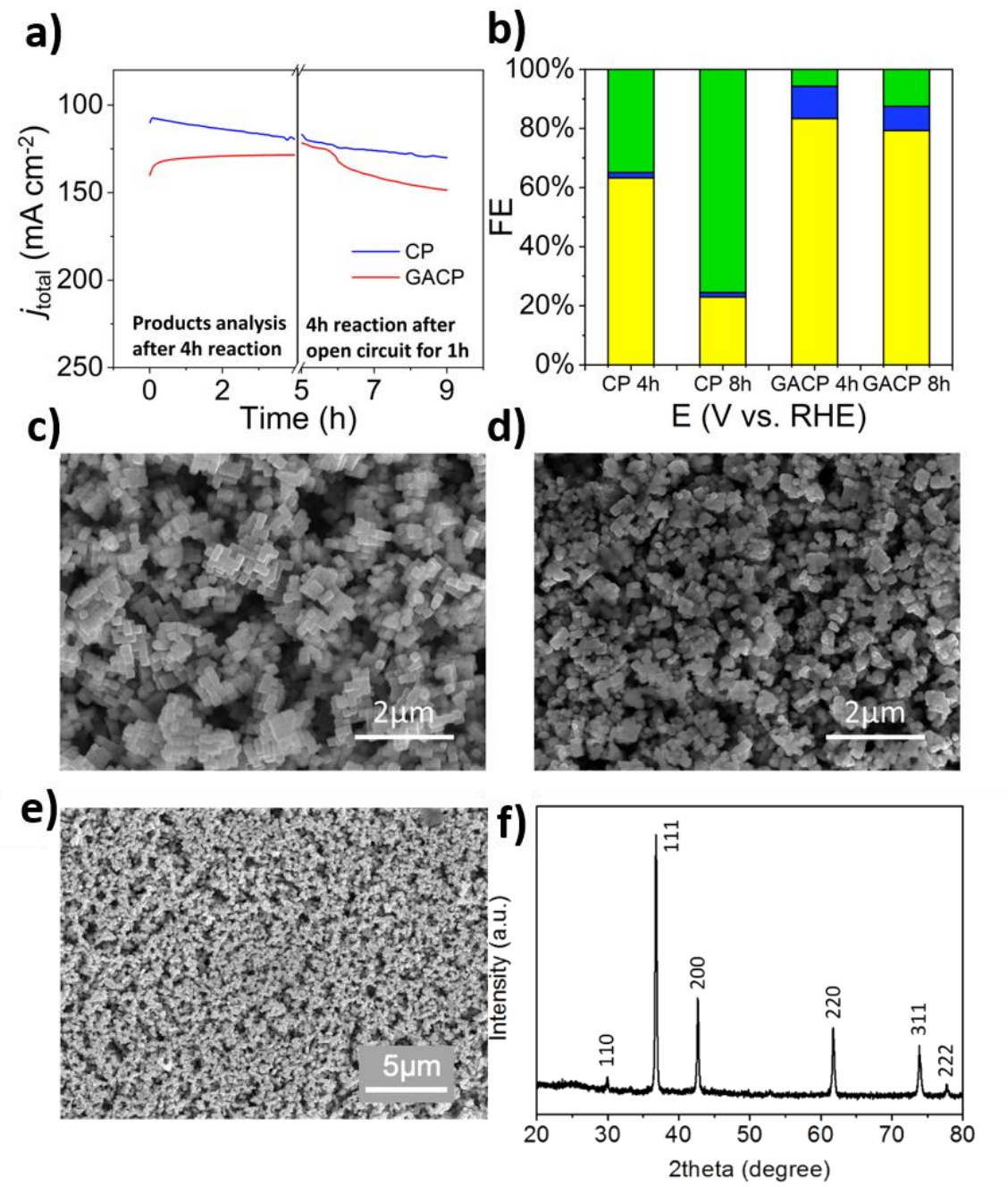

Figure 7.6 Durability test results under 1 V vs. RHE of CP-cell and GACP-cell a) CA plot for durability test b) Faradaic efficiency results c) and e) SEM of the catalyst surface of GACP-cell before durability test and d) after durability test, f) XRD pattern of Cu_2O coated carbon paper

The system's durability could also be influenced by the competing reaction of HER. After durability test, we found the catholyte was partially permeated through the CP GDE, which will lead to a higher FE value for the CP-cell towards HER. GA's hydrophobic surface delays the liquid penetration, which sustains a high FE value towards the eCO_2RR. The catalyst

morphology of GACP-cell before durability tests are shown in Figs. 7.6c and 7.6e. The XRD patten of Cu_2O coated carbon paper is shown in Fig. 7.6f. The SEM image of electrode surface after durability test is illustrated in Fig. 7.6d. Cu_2O nano cubes were found to uniformly distribute on the carbon paper before and after the durability test, which indicates that the structure of catalyst layer has not been destroyed without much loss of the catalyst loading. However, Cu_2O appears to be slightly corroded because of electrochemical corrosion, which could reduce its catalyst properties. This phenomenon could explain well the decrease of the FE value in the GACP-cell. Detailed data of durability test and relevant random error are listed in Table S5.9.

We then use the commercially available ATO nanoparticles as the eCO_2RR catalyst to investigate the feasibility of using GACP-cell to produce formate, which is in a liquid form. The performance of four types of cells are presented in Fig. 7.7. Within the potential range of -0.4 V to -1.2 V vs. RHE, the H-cell (Fig. 7.7a) presents the lowest FE values of formate and CO but the highest current densities because the HER dominates the reactions. The CP-cell (Fig. 7.7b) shows a higher FE values towards eCO_2RR, and the GACP-cell obtained the highest FE values from all potentials. From the result, the FE values of formate in the CP-cell are 45.98%, 53.66%, 55.91%, 59.71%, 49.36% at a potential range from -0.4 V to -1.2 V, where FE values of formate in the GACP-cell (Fig. 7.7d) are 70.10%, 76.91%, 78.11%, 82.98%, 84.54%, respectively. The full set of data for FEs and random errors are listed in Table S10-S15. For the GA-cell (Fig. 7.7c), the exposed skeleton will only benefit water splitting and a lower FE value of eCO_2RR is observed. Figs. 7.7e and 7.7f show the total current density and formate partial current density. The H-cell presents the highest current density towards HER, and the lowest current density of formate product. The other three types of devices present similar current densities, and the GACP-cell shows the highest current density of formate. The

results agree with our simulation results, and they can also be confirmed by the results using Cu_2O catalyst.

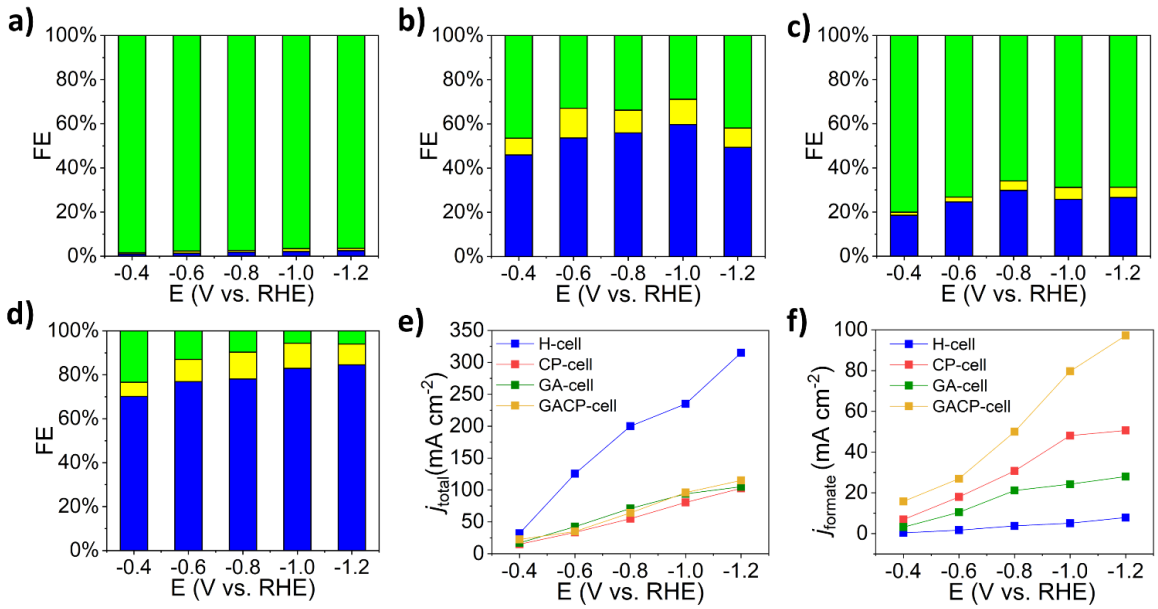

Figure 7.7 Faradaic efficiency profiles of a) H-cell b) CP-cell c) GA-cell d) GACP-cell using ATO catalyst in 1 M KOH electrolyte of eCO_2RR with products including formate (blue, bottom), H_2 (green, top) and CO (yellow, middle). e) Total Current density for results a-d), f) Current density of formate for results a-d)

7.3 Conclusion

In this chapter, we demonstrate to achieve a high FE of over 94% for CO and formate generation through improving the mass transfer of CO_2 reactant within the electrode. Results from the GACP-cell configuration shows the highest CO_2 molar concentration along the electrode surface. By using two types of catalysts, it has been confirmed that our GACP-cell can be applied for both gas and liquid products. The influence of CO_2 supply is mainly due to device design which can enhance overall eCO_2RR performance and realise low cost and high efficiency eCO_2RR. This study also shed a light on improving eCO_2RR from engineering design point of view.

Chapter 8 Chapter 8 Conclusions and Future Work

8.1 Conclusions

In this PhD study, I have demonstrated the merits of eCO_2RR technique for fuel generation. Several strategies have been employed to establish a high efficiency eCO_2RR system and results showed achievements of dramatically increased FE. I firstly focused on high performance and low-cost catalysts, in order to enhance the selectivity and activity of targeted products. High-active catalysts were explored and evaluated in re-designed and homemade GDE based electrochemical cells. The concentration and pH of electrolyte have also investigated to enhance the overall efficiency of eCO_2RR. Finally, we have established an eCO_2RR system with considerable FE and reaction activity.

The following issues were addressed in this study.

- Enhanced selectivity and activity of carbonaceous products in CP-cell

In Chapter 4, several Cu-based catalysts were evaluated using both the H-cell and CP-cell. Compared with H-cell, CP-cell with CO_2 supplied through gas diffusion electrodes show that a higher mass transfer induces a better selectivity for CO production and an improved suppression of HER. Among the results, a homemade Cu_2O nanoparticles with high surface area, which supplies sufficient active sites for eCO_2RR, showed a considerable selectivity and activity towards CO product. The FE reached to 61.31% at -2.0 V vs Ag/AgCl (-1.27 V vs. RHE) in 1 M $KHCO_3$.

In Chapter 5, commercially available ATO, ITO and In-MOF (supplied by Manchester University) were employed as electrocatalyst for eCO_2RR. We have demonstrated the CO_2

mass transfer influence using ATO in CP-cell, and a >17 folds FE increase has been achieved compared to the results in H-cell. This has clearly proved the CO_2 mass transfer effect for eCO_2RR. Then we evaluated the pH influence in CP-cell using ITO as catalyst, and the results indicated that high pH electrolyte in GDE cells could improve the eCO_2RR performance though supressing HER. Finally, In-MOFs were evaluated in $KHCO_3$ electrolyte with different concentrations. Using higher concentration of electrolyte, better FE results has been obtained with an enhanced proton transfer in electrolyte, therefore a reduced electrolyte resistance. A FE of formate up to 83.02% with a current density of 57.04 $mA \cdot cm^{-2}$ has been achieved using In-MOF at -1.0 V vs. RHE.

The CO_2 mass transfer has been found as the key reason through the studies on electrochemical cells design and manufacturing. A concept of gas diffusion electrode was used for eCO_2RR and several GDE cells were designed and fabricated using 3D-printing technique, which achieved a great enhancement on CO_2 mass transfer.

- Hybrid gas diffusion electrode cell (GACP-cell) for the enhancement of eCO_2RR

In Chapter 6, I prepared and evaluated the mechanical and electrical performance of GA, which was then employed for an advanced new cells structure in Chapter 7. A hybrid gas diffusion electrode was designed and utilized in eCO_2RR. It combines the advantages from both carbon paper and GA to dramatically improve the FE. Graphene aerogel was filled in the gas chamber, redirected CO_2 flow pathway and improved the mass transfer. Carbon paper as the substrate supported the catalyst layer. Finally, we have achieved a high FE of over 94% for CO and formate generation using synthesized Cu_2O and ATO reported in Chapters 7. This is attributed to the hybrid GDE cell with enhanced CO_2 mass transfer.

We showcase the performance achieved in this work as listed in Table 8.1, which presents the exploration pathway. By concern about the catalysts, electrolytes and cells etc, the FE has enhanced significantly.

Table 7.1 Some electrochemical results in Chapter 4-7, with enhanced FE and current density by reaction condition control.

No.	Catalyst	Cell	Electrolyte	Main C products	Applied potential	FE	Partial Current density ($mAcm^{-2}$)	Chapter or Ref.
1	Dendric Cu	H-cell	0.5 M $KHCO_3$	CO	-2.0 V vs. Ag/AgCl	2.49%	2.99	Chap. 4
2	Cu_2O	H-cell	0.5 M $KHCO_3$	CO	-1.8 V vs. Ag/AgCl	15.14%	10.49	Chap. 4
3	ATO	H-cell	0.5 M $KHCO_3$	Formate	-1.0 V vs. RHE	3.17%	10.6	Chap. 5
4	Cu_2O	CP-cell	0.5 M $KHCO_3$	CO	-2.0 V vs. Ag/AgCl	55.42%	66.50	Chap. 4
5	ATO	CP-cell	0.5 M $KHCO_3$	Formate	-2.0 V vs. Ag/AgCl	56.76%	51.1	Chap. 5
6	Cu_2O	CP-cell	1 M $KHCO_3$	CO	-2.0 V vs. Ag/AgCl	61.31%	85.96	Chap. 4
7	ITO	CP-cell	1 M $KHCO_3$	Formate	-1.2 V vs. RHE	67.54%	33.64	Chap. 5
8	ITO	CP-cell	1 M KOH	Formate	-1.2 V vs. RHE	74.24%	68.04	Chap. 5
9	Cu_2O	GACP-cell	1 M KOH	CO	-1.0 V vs. RHE	83.54%	125	Chap. 7
10	ATO	GACP-cell	1 M KOH	Formate	-1.2 V vs. RHE	84.54%	115	Chap. 7

8.2 Future works

This study focused on improving eCO_2RR from engineering design point of view. However, further enhancement on eCO_2RR are still under high demands to realize its commercialization. The critical issues include development of low-cost and stable catalyst, improvement of cells and scaling up of the system.

- Simulation assisted design of GDE cells for eCO_2RR

Simulation of CO_2 mass transfer and reaction results could greatly assist the design of cell before manufacturing. In the future, COMSOL® will be used to improve the cell design, to improve the CO_2 mass transfer, and to reduce the charge transfer resistance in cell.

- Scaling up of the current system

Currently, all the designed cells are still in a lab scale. To aim for commercialize, scale up of cells is necessary. However, there are a lot of challenges for scaling up, such as the lifetime of cells, and ease of operation for workers, etc. Therefore, more strategies should be taken to solve these problems.

- Development of gas diffusion electrodes

Low water resistance ability always occurs after long-term eCO_2RR in GDE cells. This phenomenon leads to electrolyte permeation, and the GDE cells will therefore lost its gas diffusion function. To overcome this problem, advanced materials should be discovered for GDL, with good hydrophobicity, good porosity for CO_2 capture and mass transfer. Preparation of catalyst layer should also be carefully concerned, enhancement of porosity, conductivity and hydrophobicity of catalyst layer are effective methods for eCO_2RR.

Reference

1. O. W. i. D. Hannah Ritchie and Max Roser, CO2 emissions, https://ourworldindata.org/co2-emissions#:~:text=Carbon%20dioxide%20emissions%20are%20the%20primary%20driver%20of%20global%20climate%20change.&text=This%20debate%20arises%20from%20the,for%20traded%20goods%20and%20services.).
2. S. A. Al-Saydeh and S. J. Zaidi, *Carbon Dioxide Chemistry, Capture and Oil Recovery*, 2018, 41.
3. BP, Statistical Review of World Energy, https://www.bp.com/en/global/corporate/energy-economics/statistical-review-of-world-energy.html).
4. G. Ott, *The global energy context--chances and challenges for the 21st century*, 2002.
5. M. North, in *Carbon Dioxide Utilisation*, Elsevier, 2015, pp. 3-17.
6. K. M. Mostofa, C.-Q. Liu, W. Zhai, M. Minella, D. Vione, K. Gao, D. Minakata, T. Arakaki, T. Yoshioka and K. Hayakawa, *Biogeosciences*, 2016, **13**, 1767-1786.
7. U. S. E. P. Agency, Global Greenhouse Gas Emissions Data, https://www.epa.gov/ghgemissions/global-greenhouse-gas-emissions-data).
8. NASA, Carbon dioxide Vital Signs of the planet, https://climate.nasa.gov/vital-signs/carbon-dioxide/).
9. NASA, The Cause of Climate Change, https://climate.nasa.gov/causes/).
10. B. news, Climate change: UK government to commit to 2050 target, https://www.bbc.co.uk/news/science-environment-48596775).
11. U. Nations, The Paris Agreement, https://unfccc.int/process-and-meetings/the-paris-agreement/the-paris-agreement).
12. GOV.UK, UK becomes first major economy to pass net zero emissions law, https://www.gov.uk/government/news/uk-becomes-first-major-economy-to-pass-net-zero-emissions-law).
13. P. Styring, E. A. Quadrelli and K. Armstrong, *Carbon dioxide utilisation: closing the carbon cycle*, Elsevier, 2014.
14. A. Taheri Najafabadi, *International Journal of Energy Research*, 2013, **37**, 485-499.
15. B. Metz, *Carbon Dioxide Capture and Storage: IPCC Special Report. Summary for policymakers, a report of Working Group III of the IPCC; and, Technical summary, a*

report accepted by Working Group III of the IPCC but not approved in detail, World Meteorological Organization, 2006.

16. A. Samanta, A. Zhao, G. K. H. Shimizu, P. Sarkar and R. Gupta, *Industrial & Engineering Chemistry Research*, 2011, **51**, 1438-1463.
17. M. Wang, A. Lawal, P. Stephenson, J. Sidders and C. Ramshaw, *Chemical engineering research and design*, 2011, **89**, 1609-1624.
18. H. Zhao, J. Hu, J. Wang, L. Zhou and H. Liu, *Acta Physico-Chimica Sinica*, 2007, **23**, 801-806.
19. Z. H. Ban, L. K. Keong and A. Mohd Shariff, *Advanced Materials Research*, 2014, **917**, 134-143.
20. G. Xu, F. Liang, Y. Yang, Y. Hu, K. Zhang and W. Liu, *Energies*, 2014, **7**, 3484-3502.
21. S. Bertelle, T. Gupta, D. Roizard, C. Vallières and E. Favre, *Desalination*, 2006, **199**, 401-402.
22. A. Ridgwell, T. J. Rodengen and K. E. Kohfeld, *Geophysical research letters*, 2011, **38**.
23. F. M. Orr, *Science*, 2009, **325**, 1656-1658.
24. C.-H. Huang and C.-S. Tan, *Aerosol and Air Quality Research*, 2014, **14**, 480-499.
25. N. Muradov, in *Liberating Energy from Carbon: Introduction to Decarbonization*, Springer, 2014, pp. 325-383.
26. A. Rafiee, K. Rajab Khalilpour, D. Milani and M. Panahi, *Journal of Environmental Chemical Engineering*, 2018, **6**, 5771-5794.
27. X. Xiaoding and J. Moulijn, *Energy & Fuels*, 1996, **10**, 305-325.
28. G. Zhao, X. Huang, X. Wang and X. Wang, *J. Mater. Chem. A*, 2017, **5**, 21625-21649.
29. J. Fu, K. Jiang, X. Qiu, J. Yu and M. Liu, *Materials Today*, 2020, **32**, 222-243.
30. S. Nahar, M. F. M. Zain, A. A. H. Kadhum, H. A. Hasan and M. R. Hasan, *Materials (Basel)*, 2017, **10**.
31. K. Li, B. Peng and T. Peng, *ACS Catalysis*, 2016, **6**, 7485-7527.
32. H. Narayanan, B. Viswanathan and S. Yesodharan, *Current Catalysis*, 2006, **5**, 79-107.
33. J. Qiao, Y. Liu, F. Hong and J. Zhang, *Chem Soc Rev*, 2014, **43**, 631-675.
34. C.-S. Chen, W.-H. Cheng and S.-S. Lin, *Applied Catalysis A: General*, 2004, **257**, 97-106.
35. S. Roy, A. Cherevotan and S. C. Peter, *ACS Energy Letters*, 2018, **3**, 1938-1966.
36. J. Wu, Y. Huang, W. Ye and Y. Li, *Adv Sci (Weinh)*, 2017, **4**, 1700194.
37. S. R. Lingampalli, M. M. Ayyub and C. N. R. Rao, *ACS Omega*, 2017, **2**, 2740-2748.

38. H. Yamashita, Y. Fujii, Y. Ichihashi, S. G. Zhang, K. Ikeue, D. R. Park, K. Koyano, T. Tatsumi and M. Anpo, *Catalysis Today*, 1998, **45**, 221-227.
39. K. Sayama and H. Arakawa, *The Journal of Physical Chemistry*, 1993, **97**, 531-533.
40. H. Fujiwara, H. Hosokawa, K. Murakoshi, Y. Wada, S. Yanagida, T. Okada and H. Kobayashi, *The Journal of Physical Chemistry B*, 1997, **101**, 8270-8278.
41. R. Zhou and M. I. Guzman, *The Journal of Physical Chemistry C*, 2014, **118**, 11649-11656.
42. S. Wang, Y. Guan, L. Lu, Z. Shi, S. Yan and Z. Zou, *Applied Catalysis B: Environmental*, 2018, **224**, 10-16.
43. B. AlOtaibi, S. Fan, D. Wang, J. Ye and Z. Mi, *ACS Catalysis*, 2015, **5**, 5342-5348.
44. J. L. Gunjakar, T. W. Kim, H. N. Kim, I. Y. Kim and S.-J. Hwang, *Journal of the American Chemical Society*, 2011, **133**, 14998-15007.
45. C. G. Silva, Y. Bouizi, V. Fornes and H. Garcia, *Journal of the American Chemical Society*, 2009, **131**, 13833-13839.
46. Y. Lee, J. H. Choi, H. J. Jeon, K. M. Choi, J. W. Lee and J. K. Kang, *Energy & Environmental Science*, 2011, **4**, 914-920.
47. X.-L. Luo, Z. Yin, M.-H. Zeng and M. Kurmoo, *Inorganic Chemistry Frontiers*, 2016, **3**, 1208-1226.
48. M. W. Logan, S. Ayad, J. D. Adamson, T. Dilbeck, K. Hanson and F. J. Uribe-Romo, *Journal of Materials Chemistry A*, 2017, **5**, 11854-11863.
49. X. Wang, K. Maeda, A. Thomas, K. Takanabe, G. Xin, J. M. Carlsson, K. Domen and M. Antonietti, *Nature materials*, 2009, **8**, 76-80.
50. P. Ji, M. Takeuchi, T.-M. Cuong, J. Zhang, M. Matsuoka and M. Anpo, *Research on Chemical Intermediates*, 2010, **36**, 327-347.
51. X. Chen and C. Burda, *Journal of the American Chemical Society*, 2008, **130**, 5018-5019.
52. G. Xi, S. Ouyang, P. Li, J. Ye, Q. Ma, N. Su, H. Bai and C. Wang, *Angewandte Chemie International Edition*, 2012, **51**, 2395-2399.
53. Z. Zhang, Y. Huang, K. Liu, L. Guo, Q. Yuan and B. Dong, *Advanced Materials*, 2015, **27**, 5906-5914.
54. S. Garg, M. Li, A. Z. Weber, L. Ge, L. Li, V. Rudolph, G. Wang and T. E. Rufford, *Journal of Materials Chemistry A*, 2020, **8**, 1511-1544.

55. J. Durst, A. Rudnev, A. Dutta, Y. Fu, J. Herranz, V. Kaliginedi, A. Kuzume, A. A. Permyakova, Y. Paratcha, P. Broekmann and T. J. Schmidt, *Chimia (Aarau)*, 2015, **69**, 769-776.
56. R. Winkler-Goldstein and A. Rastetter, *Green*, 2013, **3**, 69-78.
57. M. Jentsch, T. Trost and M. Sterner, *Energy Procedia*, 2014, **46**, 254-261.
58. Z. W. Seh, J. Kibsgaard, C. F. Dickens, I. Chorkendorff, J. K. Norskov and T. F. Jaramillo, *Science*, 2017, **355**.
59. W. Leitner, *Angewandte Chemie International Edition in English*, 1995, **34**, 2207-2221.
60. E. E. Benson, C. P. Kubiak, A. J. Sathrum and J. M. Smieja, *Chemical Society Reviews*, 2009, **38**, 89-99.
61. D. D. Zhu, J. L. Liu and S. Z. Qiao, *Advanced materials*, 2016, **28**, 3423-3452.
62. S. Liang, N. Altaf, L. Huang, Y. Gao and Q. Wang, *Journal of CO2 Utilization*, 2020, **35**, 90-105.
63. S. Hernández, M. A. Farkhondehfal, F. Sastre, M. Makkee, G. Saracco and N. Russo, *Green Chemistry*, 2017, **19**, 2326-2346.
64. R. M. Heck, R. J. Farrauto and S. T. Gulati, *Catalytic air pollution control: commercial technology*, John Wiley & Sons, 2016.
65. D. T. Whipple and P. J. Kenis, *The Journal of Physical Chemistry Letters*, 2010, **1**, 3451-3458.
66. B. A. Rosen, A. Salehi-Khojin, M. R. Thorson, W. Zhu, D. T. Whipple, P. J. Kenis and R. I. Masel, *Science*, 2011, **334**, 643-644.
67. Y. Peng, T. Wu, L. Sun, J. M. V. Nsanzimana, A. C. Fisher and X. Wang, *ACS Appl Mater Interfaces*, 2017, **9**, 32782-32789.
68. N. Nilius, H. Fedderwitz, B. Gross, C. Noguera and J. Goniakowski, *Phys Chem Chem Phys*, 2016, **18**, 6729-6733.
69. Y. Fu, Y. Li, X. Zhang, Y. Liu, J. Qiao, J. Zhang and D. P. Wilkinson, *Applied Energy*, 2016, **175**, 536-544.
70. W. Zhang, Y. Hu, L. Ma, G. Zhu, Y. Wang, X. Xue, R. Chen, S. Yang and Z. Jin, *Adv Sci (Weinh)*, 2018, **5**, 1700275.
71. Y. Hori, H. Wakebe, T. Tsukamoto and O. Koga, *Electrochimica Acta*, 1994, **39**, 1833-1839.
72. H. Li and C. Oloman, *Journal of Applied Electrochemistry*, 2006, **36**, 1105.
73. Y. Hori, K. Kikuchi and S. Suzuki, *Chemistry Letters*, 1985, **14**, 1695-1698.

74. S. Zhang, P. Kang and T. J. Meyer, *Journal of the American Chemical Society*, 2014, **136**, 1734-1737.
75. C. Zhao and J. Wang, *Chemical Engineering Journal*, 2016, **293**, 161-170.
76. Z. Xia, M. Freeman, D. Zhang, B. Yang, L. Lei, Z. Li and Y. Hou, *ChemElectroChem*, 2018, **5**, 253-259.
77. D. D. Zhu, J. L. Liu and S. Z. Qiao, *Adv Mater*, 2016, **28**, 3423-3452.
78. H. Noda, S. Ikeda, Y. Oda, K. Imai, M. Maeda and K. Ito, *Bulletin of the Chemical Society of Japan*, 1990, **63**, 2459-2462.
79. C. Chen, B. Zhang, J. Zhong and Z. Cheng, *Journal of Materials Chemistry A*, 2017, **5**, 21955-21964.
80. S. IKEDA, A. HATTORI, M. MAEDA, K. ITO and H. NODA, *Electrochemistry*, 2000, **68**, 257-261.
81. S. IKEDA, A. HATTORI, K. ITO and H. NODA, *Electrochemistry*, 1999, **67**, 27-33.
82. J. Rosen, G. S. Hutchings, Q. Lu, R. V. Forest, A. Moore and F. Jiao, *Acs Catalysis*, 2015, **5**, 4586-4591.
83. J. Lee and Y. Tak, *Electrochimica acta*, 2001, **46**, 3015-3022.
84. S. P. Liu, M. Zhao, W. Gao and Q. Jiang, *ChemSusChem*, 2017, **10**, 387-393.
85. W. Tang, A. A. Peterson, A. S. Varela, Z. P. Jovanov, L. Bech, W. J. Durand, S. Dahl, J. K. Nørskov and I. Chorkendorff, *Physical Chemistry Chemical Physics*, 2012, **14**, 76-81.
86. J. H. Montoya, C. Shi, K. Chan and J. K. Nørskov, *The journal of physical chemistry letters*, 2015, **6**, 2032-2037.
87. T. Hatsukade, K. P. Kuhl, E. R. Cave, D. N. Abram and T. F. Jaramillo, *Physical Chemistry Chemical Physics*, 2014, **16**, 13814-13819.
88. X. Nie, W. Luo, M. J. Janik and A. Asthagiri, *Journal of catalysis*, 2014, **312**, 108-122.
89. Y. Hori, H. Konishi, T. Futamura, A. Murata, O. Koga, H. Sakurai and K. Oguma, *Electrochimica acta*, 2005, **50**, 5354-5369.
90. K. P. Kuhl, E. R. Cave, D. N. Abram and T. F. Jaramillo, *Energy & Environmental Science*, 2012, **5**, 7050-7059.
91. T.-T. Zhuang, Y. Pang, Z.-Q. Liang, Z. Wang, Y. Li, C.-S. Tan, J. Li, C. T. Dinh, P. De Luna, P.-L. Hsieh, T. Burdyny, H.-H. Li, M. Liu, Y. Wang, F. Li, A. Proppe, A. Johnston, D.-H. Nam, Z.-Y. Wu, Y.-R. Zheng, A. H. Ip, H. Tan, L.-J. Chen, S.-H. Yu, S. O. Kelley, D. Sinton and E. H. Sargent, *Nature Catalysis*, 2018, **1**, 946-951.

92. S. Cao, F. F. Tao, Y. Tang, Y. Li and J. Yu, *Chemical Society Reviews*, 2016, **45**, 4747-4765.
93. P. Iyengar, J. Huang, G. L. De Gregorio, C. Gadiyar and R. Buonsanti, *Chemical Communications*, 2019, **55**, 8796-8799.
94. L. Wang, W. Chen, D. Zhang, Y. Du, R. Amal, S. Qiao, J. Wu and Z. Yin, *Chemical Society Reviews*, 2019, **48**, 5310-5349.
95. L. Dai, Q. Qin, P. Wang, X. Zhao, C. Hu, P. Liu, R. Qin, M. Chen, D. Ou and C. Xu, *Science advances*, 2017, **3**, e1701069.
96. M. Ma, K. Djanashvili and W. A. Smith, *Angewandte chemie international edition*, 2016, **55**, 6680-6684.
97. H. Xiang, S. Rasul, B. Hou, J. Portoles, P. Cumpson and E. H. Yu, *ACS applied materials & interfaces*, 2019, **12**, 601-608.
98. X. Sun, L. Lu, Q. Zhu, C. Wu, D. Yang, C. Chen and B. Han, *Angewandte Chemie International Edition*, 2018, **57**, 2427-2431.
99. T. Ma, Q. Fan, X. Li, J. Qiu, T. Wu and Z. Sun, *Journal of CO2 Utilization*, 2019, **30**, 168-182.
100. N. Uemoto, M. Furukawa, I. Tateishi, H. Katsumata and S. Kaneco, *ChemEngineering*, 2019, **3**, 15.
101. P. P. Sharma, J. Wu, R. M. Yadav, M. Liu, C. J. Wright, C. S. Tiwary, B. I. Yakobson, J. Lou, P. M. Ajayan and X. D. Zhou, *Angewandte Chemie*, 2015, **127**, 13905-13909.
102. B. Kumar, M. Asadi, D. Pisasale, S. Sinha-Ray, B. A. Rosen, R. Haasch, J. Abiade, A. L. Yarin and A. Salehi-Khojin, *Nature communications*, 2013, **4**, 1-8.
103. C. Wang, Z. Xie, K. E. deKrafft and W. Lin, *Journal of the American Chemical Society*, 2011, **133**, 13445-13454.
104. X. Kang, B. Wang, K. Hu, K. Lyu, X. Han, B. F. Spencer, M. D. Frogley, F. Tuna, E. J. McInnes and R. A. Dryfe, *Journal of the American Chemical Society*, 2020, **142**, 17384-17392.
105. Y. Wang, P. Hou, Z. Wang and P. Kang, *ChemPhysChem*, 2017, **18**, 3142-3147.
106. Y. Zheng, A. Vasileff, X. Zhou, Y. Jiao, M. Jaroniec and S.-Z. Qiao, *Journal of the American Chemical Society*, 2019, **141**, 7646-7659.
107. Y. Xu, F. Li, A. Xu, J. P. Edwards, S.-F. Hung, C. M. Gabardo, C. P. O'Brien, S. Liu, X. Wang and Y. Li, *Nature Communications*, 2021, **12**, 1-7.
108. F. Li, M. Xue, J. Li, X. Ma, L. Chen, X. Zhang, D. R. MacFarlane and J. Zhang, *Angew Chem Int Ed Engl*, 2017, **56**, 14718-14722.

109. Y. Chen and M. W. Kanan, *J Am Chem Soc*, 2012, **134**, 1986-1989.
110. J. Li, X. Han, X. Zhang, A. M. Sheveleva, Y. Cheng, F. Tuna, E. J. McInnes, L. J. M. McPherson, S. J. Teat and L. L. Daemen, *Nature chemistry*, 2019, **11**, 1085-1090.
111. H. Xiang, S. Rasul, K. Scott, J. Portoles, P. Cumpson and E. H. Yu, *Journal of CO2 Utilization*, 2019, **30**, 214-221.
112. S. Narayanan, B. Haines, J. Soler and T. Valdez, *Journal of The Electrochemical Society*, 2010, **158**, A167.
113. D. M. Weekes, D. A. Salvatore, A. Reyes, A. Huang and C. P. Berlinguette, *Accounts of chemical research*, 2018, **51**, 910-918.
114. Z. Zhan and L. Zhao, *Journal of Power Sources*, 2010, **195**, 7250-7254.
115. E. L. Clark, M. R. Singh, Y. Kwon and A. T. Bell, *Analytical chemistry*, 2015, **87**, 8013-8020.
116. H. B. Yang, S.-F. Hung, S. Liu, K. Yuan, S. Miao, L. Zhang, X. Huang, H.-Y. Wang, W. Cai and R. Chen, *Nature Energy*, 2018, **3**, 140-147.
117. F. Pan, B. Li, W. Deng, Z. Du, Y. Gang, G. Wang and Y. Li, *Applied Catalysis B: Environmental*, 2019, **252**, 240-249.
118. R. Kas, R. Kortlever, A. Milbrat, M. T. Koper, G. Mul and J. Baltrusaitis, *Physical Chemistry Chemical Physics*, 2014, **16**, 12194-12201.
119. Y. Wang, H. Lei, H. Xiang, Y. Fu, C. Xu, Y. Jiang, B. B. Xu, E. H. Yu, C. Gao and T. X. Liu, *Advanced Energy and Sustainability Research*, 2021, 2100083.
120. G. Wang, J. Pan and H. Yang, *Journal of CO2 Utilization*, 2018, **23**, 152-158.
121. S. Ren, D. Joulié, D. Salvatore, K. Torbensen, M. Wang, M. Robert and C. P. Berlinguette, *Science*, 2019, **365**, 367-369.
122. S. Ma, M. Sadakiyo, R. Luo, M. Heima, M. Yamauchi and P. J. Kenis, *Journal of Power Sources*, 2016, **301**, 219-228.
123. L. Yu, J. Wang, X. Hu, Z. Ye, C. Buckley and D. Dong, *Electrochemistry Communications*, 2018, **86**, 72-75.
124. J. Qiao, Y. Liu and J. Zhang, *Electrochemical reduction of carbon dioxide: fundamentals and technologies*, CRC Press, 2016.
125. Y. Hori, K. Kikuchi, A. Murata and S. Suzuki, *Chemistry Letters*, 1986, **15**, 897-898.
126. J. Kim, D. Summers and K. Frese Jr, *Journal of electroanalytical chemistry and interfacial electrochemistry*, 1988, **245**, 223-244.
127. B. Seddon, M. Eddowes, A. Firth, A. Owen and H. Girault, *Electrochimica acta*, 1991, **36**, 763-771.

128. Y. Chen and M. W. Kanan, *Journal of the American Chemical Society*, 2012, **134**, 1986-1989.
129. M. Le, M. Ren, Z. Zhang, P. T. Sprunger, R. L. Kurtz and J. C. Flake, *Journal of The Electrochemical Society*, 2011, **158**.
130. C. Y. Falong Jia, Kejian Deng, and Lizhi Zhang, *J. Phys. Chem.*, 2007, **111**, 8424-8431.
131. C. Chen, B. Zhang, J. Zhong and Z. Cheng, *J. Mater. Chem. A*, 2017, **5**, 21955-21964.
132. K. Ogura, H. Yano and T. Tanaka, *Catalysis Today*, 2004, **98**, 515-521.
133. H. Li and C. Oloman, *Journal of Applied Electrochemistry*, 2005, **35**, 955-965.
134. F. S. H. Yano, M. Nakayama, K. Ogura, *Journal of Electroanalytical Chemistry*, 2001, **519**, 93-100.
135. S. Srinivasan, H. D. Hurwitz and J. O. M. Bockris, *The Journal of Chemical Physics*, 1967, **46**, 3108-3122.
136. Y. Wang and K. S. Chen, *Journal of The Electrochemical Society*, 2011, **158**, B1292-B1299.
137. A. Li, H. Wang, J. Han and L. Liu, *Frontiers of Chemical Science and Engineering*, 2012, **6**, 381-388.
138. D. Higgins, C. Hahn, C. Xiang, T. F. Jaramillo and A. Z. Weber, *ACS Energy Letters*, 2018, **4**, 317-324.
139. T. Burdyny and W. A. Smith, *Energy & Environmental Science*, 2019, DOI: 10.1039/c8ee03134g.
140. F. Bidault, D. J. L. Brett, P. H. Middleton and N. P. Brandon, *Journal of Power Sources*, 2009, **187**, 39-48.
141. S. Park, J. W. Lee and B. N. Popov, *International Journal of Hydrogen Energy*, 2012, **37**, 5850-5865.
142. S. Pérez-Rodríguez, E. Pastor and M. Lázaro, *International Journal of Hydrogen Energy*, 2018, **43**, 7911-7922.
143. S. Kusama, T. Saito, H. Hashiba, A. Sakai and S. Yotsuhashi, *ACS Catalysis*, 2017, **7**, 8382-8385.
144. Z. Chen, K. Mou, X. Wang and L. Liu, *Angewandte Chemie*, 2018, **130**, 12972-12976.
145. H.-L. Gao, Y.-B. Zhu, L.-B. Mao, F.-C. Wang, X.-S. Luo, Y.-Y. Liu, Y. Lu, Z. Pan, J. Ge, W. Shen, Y.-R. Zheng, L. Xu, L.-J. Wang, W.-H. Xu, H.-A. Wu and S.-H. Yu, *Nature Communications*, 2016, **7**, 12920.
146. H. Hu, Z. Zhao, W. Wan, Y. Gogotsi and J. Qiu, *Advanced Materials*, 2013, **25**, 2219-2223.

147. H. Sun, Z. Xu and C. Gao, *Advanced Materials*, 2013, **25**, 2554-2560.
148. X. Xu, Q. Zhang, Y. Yu, W. Chen, H. Hu and H. Li, *Advanced Materials*, 2016, **28**, 9223-9230.
149. C. Li, L. Qiu, B. Zhang, D. Li and C.-Y. Liu, *Advanced Materials*, 2016, **28**, 1510-1516.
150. X. Liu, J. Xi, B. B. Xu, B. Fang, Y. Wang, M. Bayati, K. Scott and C. Gao, *Small Methods*, 2018, **2**, 1800138.
151. X. Liu, J. Xi, B. B. Xu, B. Fang, Y. Wang, M. Bayati, K. Scott and C. Gao, *Small Methods*, 2018, **2**, 1800138.
152. H.-L. Gao, Y.-B. Zhu, L.-B. Mao, F.-C. Wang, X.-S. Luo, Y.-Y. Liu, Y. Lu, Z. Pan, J. Ge and W. Shen, *Nature communications*, 2016, **7**, 1-8.
153. C. Li, L. Qiu, B. Zhang, D. Li and C. Y. Liu, *Advanced Materials*, 2016, **28**, 1510-1516.
154. H. U. Technology, Sonocatalysis – Ultrasonically Assisted Catalysis, https://www.hielscher.com/sonocatalysis_catalysis.htm).
155. M. Technology, What is Freeze Drying?, https://www.millrocktech.com/lyosight/lyobrary/what-is-freeze-drying/#:~:text=Freeze%20drying%20is%20a%20water,in%20the%20material%20to%20sublimate.).
156. Y. Bai, T. Yang, Q. Gu, G. Cheng and R. Zheng, *powder technology*, 2012, **227**, 35-42.
157. K. Eid, H. Wang and L. Wang, in *Supra-Materials Nanoarchitectonics*, Elsevier, 2017, pp. 135-171.
158. M. B. Lim, M. Hu, S. Manandhar, A. Sakshaug, A. Strong, L. Riley and P. J. Pauzauskie, *Carbon*, 2015, **95**, 616-624.
159. R. Kohli and K. L. Mittal, *Developments in Surface Contamination and Cleaning, Vol. 1: Fundamentals and Applied Aspects*, William Andrew, 2015.
160. P. Atkins and J. De Paula, *Elements of physical chemistry*, Oxford University Press, USA, 2013.
161. B. Cullity, *Inc., CA, USA*, 1978, **197**, 356.
162. L. V. Azaroff and M. J. Buerger, *McGrow-Hill Book Company, New York*, 1958.
163. D. Brandon and W. D. Kaplan, *Microstructural characterization of materials*, John Wiley & Sons, 2013.
164. S. Nasrazadani and S. Hassani, in *Handbook of Materials Failure Analysis with Case Studies from the Oil and Gas Industry*, Elsevier, 2016, pp. 39-54.
165. M. Hoorfar and A. Neumann, *Advances in colloid and interface science*, 2006, **121**, 25-49.

166. D. L. Pavia, G. S. Kriz, G. M. Lampman and R. G. Engel, *A small scale approach to organic laboratory techniques*, Nelson Education, 2015.
167. J. Hong, W. Zhang, J. Ren and R. Xu, *Analytical methods*, 2013, **5**, 1086-1097.
168. Y. Tomita, S. Teruya, O. Koga and Y. Hori, *Journal of The Electrochemical Society*, 2000, **147**, 4164.
169. D. Turner, Gas Chromatography – How a Gas Chromatography Machine Works, How To Read a Chromatograph and GCxGC, https://www.technologynetworks.com/analysis/articles/gas-chromatography-how-a-gas-chromatography-machine-works-how-to-read-a-chromatograph-and-gcxgc-335168).
170. Shimadzu, BID, https://www.shimadzu.com/research_and_development/technology_branding/nexis_technologies/bid.html).
171. SeQuant, A Practical Guide to Ion Chromatography - An Introduction and Troubleshoooting Manual, https://www.nestgrp.com/pdf/Zp1/Sp1/ION_Manual.pdf).
172. A. J. Bard and L. R. Faulkner, *Electrochemical Methods*, 2001, **2**, 580-632.
173. X. Chang, T. Wang, Z. J. Zhao, P. Yang, J. Greeley, R. Mu, G. Zhang, Z. Gong, Z. Luo, J. Chen, Y. Cui, G. A. Ozin and J. Gong, *Angew Chem Int Ed Engl*, 2018, **57**, 15415-15419.
174. A. Engelbrecht, C. Uhlig, O. Stark, M. Hämmerle, G. Schmid, E. Magori, K. Wiesner-Fleischer, M. Fleischer and R. Moos, *Journal of The Electrochemical Society*, 2018, **165**, J3059-J3068.
175. S. Kaneco, K. Iiba, H. Katsumata, T. Suzuki and K. Ohta, *Electrochimica Acta*, 2006, **51**, 4880-4885.
176. S. Park, J.-W. Lee and B. N. Popov, *International Journal of Hydrogen Energy*, 2012, **37**, 5850-5865.
177. D. Kopljar, A. Inan, P. Vindayer, N. Wagner and E. Klemm, *Journal of Applied Electrochemistry*, 2014, **44**, 1107-1116.
178. J. Song, H. Song, B. Kim and J. Oh, *Catalysts*, 2019, **9**, 224.
179. T. Burdyny and W. A. Smith, *Energy & Environmental Science*, 2019, **12**, 1442-1453.
180. Formlabs, Material data sheet Standard, https://archive-media.formlabs.com/upload/Clear-DataSheet.pdf).
181. Proto3000, Objet30 Series, https://proto3000.com/product/objet30-series/).

182. Stratasys, Vero, https://www.stratasys.com/materials/search/vero?utm_source=data-sheet&utm_medium=pdf&utm_content=vero-data-sheet-link-1-vero).
183. J. Low, J. Yu and W. Ho, *The journal of physical chemistry letters*, 2015, **6**, 4244-4251.
184. J. Yang, W. Ma, D. Chen, A. Holmen and B. H. Davis, *Applied Catalysis A: General*, 2014, **470**, 250-260.
185. H. Jahangiri, J. Bennett, P. Mahjoubi, K. Wilson and S. Gu, *Catalysis Science & Technology*, 2014, **4**, 2210-2229.
186. S. Back, M. S. Yeom and Y. Jung, *Acs Catalysis*, 2015, **5**, 5089-5096.
187. Y. S. Ham, S. Choe, M. J. Kim, T. Lim, S.-K. Kim and J. J. Kim, *Applied Catalysis B: Environmental*, 2017, **208**, 35-43.
188. D. Gao, H. Zhou, F. Cai, J. Wang, G. Wang and X. Bao, *Acs Catalysis*, 2018, **8**, 1510-1519.
189. C. W. Li and M. W. Kanan, *Journal of the American Chemical Society*, 2012, **134**, 7231-7234.
190. M. Le, M. Ren, Z. Zhang, P. T. Sprunger, R. L. Kurtz and J. C. Flake, *Journal of the Electrochemical Society*, 2011, **158**, E45.
191. C. Azina, 2017.
192. J. Long, J. Dong, X. Wang, Z. Ding, Z. Zhang, L. Wu, Z. Li and X. Fu, *Journal of colloid and interface science*, 2009, **333**, 791-799.
193. Q. He, Y. Tian, Y. Wu, J. Liu, G. Li, P. Deng and D. Chen, *Biomolecules*, 2019, **9**, 176.
194. N. Gupta, M. Gattrell and B. MacDougall, *Journal of applied electrochemistry*, 2006, **36**, 161-172.
195. K. M. Yam, N. Guo, Z. Jiang, S. Li and C. Zhang, *Catalysts*, 2020, **10**, 53.
196. D. H. Kweon, M. S. Okyay, S.-J. Kim, J.-P. Jeon, H.-J. Noh, N. Park, J. Mahmood and J.-B. Baek, *Nature communications*, 2020, **11**, 1-10.
197. S. Gao, Y. Lin, X. Jiao, Y. Sun, Q. Luo, W. Zhang, D. Li, J. Yang and Y. Xie, *Nature*, 2016, **529**, 68-71.
198. J. Chang, L. Feng, C. Liu, W. Xing and X. Hu, *Energy & Environmental Science*, 2014, **7**, 1628-1632.
199. S. Kapusta and N. Hackerman, *Journal of the Electrochemical Society*, 1983, **130**, 607.
200. J. L. White and A. B. Bocarsly, *Journal of The Electrochemical Society*, 2016, **163**, H410.
201. F. Li, M. Xue, J. Li, X. Ma, L. Chen, X. Zhang, D. R. MacFarlane and J. Zhang, *Angewandte Chemie*, 2017, **129**, 14910-14914.

202. E. González-Arribas, T. Bobrowski, C. Di Bari, K. Sliozberg, R. Ludwig, M. D. Toscano, A. L. De Lacey, M. Pita, W. Schuhmann and S. Shleev, *Biosensors and Bioelectronics*, 2017, **97**, 46-52.
203. K. S. Yoo, S. H. Park and J. H. Kang, *Sensors and Actuators B: Chemical*, 2005, **108**, 159-164.
204. I. Jiménez-Morales, S. Cavaliere, M. Dupont, D. Jones and J. Rozière, *Sustainable Energy & Fuels*, 2019, **3**, 1526-1535.
205. D. J. You, K. Kwon, C. Pak and H. Chang, *Catalysis Today*, 2009, **146**, 15-19.
206. S. Chaemchuen, N. A. Kabir, K. Zhou and F. Verpoort, *Chemical Society Reviews*, 2013, **42**, 9304-9332.
207. X. Fang, B. Zong and S. Mao, *Nano-Micro Letters*, 2018, **10**, 64.
208. S. Lee, S. Hong and J. Lee, *Catalysis Today*, 2017, **288**, 11-17.
209. C.-T. Dinh, T. Burdyny, M. G. Kibria, A. Seifitokaldani, C. M. Gabardo, F. P. G. De Arquer, A. Kiani, J. P. Edwards, P. De Luna and O. S. Bushuyev, *Science*, 2018, **360**, 783-787.
210. V. Subramani, A. Basile and T. N. Veziroglu, *Compendium of Hydrogen Energy: Hydrogen Production and Purification*, Woodhead Publishing, 2015.
211. H. Atallah, M. E. Mahmoud, A. Jelle, A. Lough and M. Hmadeh, *Dalton Transactions*, 2018, **47**, 799-806.
212. X. Zhang, Z. Sui, B. Xu, S. Yue, Y. Luo, W. Zhan and B. Liu, *Journal of Materials Chemistry*, 2011, **21**, 6494-6497.
213. C. K. Ho and S. W. Webb, *Gas transport in porous media*, Springer, 2006.
214. J. H. Montoya, C. Shi, K. Chan and J. K. Norskov, *J Phys Chem Lett*, 2015, **6**, 2032-2037.
215. J. Resasco, L. D. Chen, E. Clark, C. Tsai, C. Hahn, T. F. Jaramillo, K. Chan and A. T. Bell, *J Am Chem Soc*, 2017, **139**, 11277-11287.

Appendix

Appendix 1 FE calculation

The calculate steps for calculating FE from CV plot and GC, IC results shown as following:

Data from GC：

A customized standard mixed gas (BOC) with the components of H_2 (1.000%), CO (1.000%), CH_4 (0.500%), CO_2 (96.000%), C_2H_4 (0.500%), C_2H_6 (0.500%), and C_3H_6 (0.500%) was used as the reference standard for the GC to analyse gas. Area normalization method was used to calculate the concentration of each component in the sample gas.

Step 1: Calculation of m%

To calculate mole mass percentage of each component m%,

$$\mathrm{m} = f \times \mathrm{A}$$

where m is the concentration of the component X in mix gas, *f* is correction factor, and A is the peak area of X.

Hypothesize f_H=1, thus

$$m_H = f_H \cdot A_H$$

Where A_H is the peak aera obtained from GC result of standard mixed gas sample.

For one certain component *i*:

$$m_i = f_i \cdot A_i$$

Then

$$\frac{m_H}{m_i} = \frac{f_H \cdot A_H}{f_i \cdot A_i}$$

$$f_i = \frac{m_i \cdot f_H \cdot A_H}{m_H \cdot A_i}$$

In standard mix gas: C(H_2)=1%, C(CO)=1%, C(CH_4)=0.5%, C(CO_2)=96%, C(C_2H_4)=0.5%, C(C_2H_6)=0.5%,

$$f_i = \frac{i\%}{1\%} \cdot \frac{A_H}{A_i}$$

where *i*% is the concentration percentage of component *i*.

Then mole concentration is:

$$\boldsymbol{m_i\%} = \frac{\boldsymbol{f_i \cdot A_i}}{\sum \boldsymbol{f_i \cdot A_i}} \cdot \mathbf{100\%} \qquad \text{Eq. S1.1}$$

Step 2: Combine FE equation and ideal gas equation of states:

FE equation:

$$\mathrm{FE} = \frac{\alpha \cdot \mathrm{n} \cdot \mathrm{F}}{\mathrm{I} \cdot \mathrm{t}}$$

where α is number of transferred electrons, *n* is mol mass, F is Faraday number, I is the average current of CA test and t is reaction time.

Ideal gas equation:

$$\mathrm{PV} = \mathrm{nRT},$$

$$\text{For standard gas under } 25\ ^{\mathrm{O}}\mathrm{C},$$

$$\frac{V}{n} = \frac{RT}{P} = \frac{8.314 \times 298.15}{101325/1000} = 24.464\mathrm{L/mol} \qquad \text{Eq. S1.2}$$

where P is pressure, V is gas volume, n is mol mass, R is constant value 8.314 and T is Kalvin temperature.

Then set CO_2 flow rate is *x* ml/min, therefore the total volume of collected gas is:

$$\frac{x \cdot t}{60} \qquad \text{Eq. S1.3}$$

Combine the Equation S1.2 and Equation S1.3, the mole of component (n_i)is

$$n_i = (\frac{x \cdot t}{60} \times m_i\%)/24.464 \qquad \text{Eq. S1.4}$$

Therefore, the FE can be calculated:

$$\therefore \boldsymbol{FE} = \frac{\boldsymbol{a \cdot n \cdot F}}{\boldsymbol{I \cdot t}} = \frac{\boldsymbol{a} \cdot (\frac{\boldsymbol{x \cdot t}}{\mathbf{60}} \cdot \boldsymbol{m}\%/\mathbf{24.464}) \cdot \boldsymbol{F}}{\boldsymbol{I \cdot t}} = \frac{\boldsymbol{a} \cdot (\frac{\boldsymbol{x}}{\mathbf{60}} \cdot \boldsymbol{m}\%/\mathbf{24.464}) \cdot \boldsymbol{F}}{\boldsymbol{I}}$$

Data from IC：

Firstly, several formate solutions were prepared with a gradient concentration. Secondly, the standard samples were tested in IC and the peaks of formate (A_f) were obtained. Thirdly, a Concentration-Peak aera plot was made. Finally, the concentration of tested samples can be calculated by the concentration-Peak aera plot.

$$\mathbf{FE} = \frac{\boldsymbol{a \cdot n \cdot F}}{\boldsymbol{I \cdot t}} = \frac{\boldsymbol{n \cdot C \cdot V \cdot F}}{\boldsymbol{I \cdot t}}$$

Where α is number of transferred electrons, n is mol mass, C is the concentration of tested samples, V is the volume of tested sample, F is Faraday constant, I is the average current of CA and T is the reaction time.

Appendix 2 Supplementary Information of dendritic Cu, commercial Cu_2O and synthesized Cu_2O in Chapter 4

*All potential presents in this chapter vs. Ag/AgCl

**Error in brackets, sample standard deviation

2.1 Data of Electrochemical Evaluation in H-cell

Table S2.1 Dendritic Cu Faradaic efficiency data in H-cell, 0.5 M $KHCO_3$

Faradaic efficiency	-1.2 V	-1.4 V	-1.6 V	-1.8 V	-2.0 V
H_2	100.00% (0.00%)	99.05% (0.04%)	98.50% (0.05%)	98.20% (0.03%)	97.51% (0.06%)
CO	0.00% (0.00%)	0.95% (0.04%)	1.50% (0.05%)	1.80% (0.03%)	2.49% (0.06%)
HCOOH	0.00% (0.00%)	0.00% (0.00%)	0.00% (0.00%)	0.00% (0.00%)	0.00% (0.00%)

Table S2.2 Commercial Cu_2O Faradaic efficiency data in H-cell, 0.5 M $KHCO_3$

Faradaic efficiency	-1.2 V	-1.4 V	-1.6 V	-1.8 V	-2.0 V
H_2	96.10% (0.06%)	92.35% (0.11%)	90.93% (0.19%)	86.65% (0.79%)	84.96% (1.71%)
CO	3.90% (0.06%)	7.65% (0.11%)	8.56% (0.17%)	12.48% (0.73%)	13.90% (1.62%)
HCOOH	0.00% (0.00%)	0.00% (0.00%)	0.51% (0.04%)	0.87% (0.07%)	1.14% (0.09%)

Table S2.3 Synthesized Cu_2O Faradaic efficiency data in H-cell, 0.5 M $KHCO_3$

Faradaic efficiency	-1.2 V	-1.4 V	-1.6 V	-1.8 V	-2.0 V
H_2	96.01% (0.15%)	96.32% (0.15%)	91.23% (0.97%)	83.56% (0.51%)	84.63% (0.92%)
CO	3.99% (0.15%)	3.17% (0.14%)	7.88% (1.05%)	15.14% (0.65%)	14.16% (0.75%)
HCOOH	0.00% (0.00%)	0.51% (0.05%)	0.89% (0.09%)	1.30% (0.16%)	1.21% (0.17%)

Table S2.4 Total Current density data in H-cell, 0.5 M $KHCO_3$

Current density*	-1.2 V	-1.4 V	-1.6 V	-1.8 V	-2.0 V
Dendritic Cu	42.2 (1.5)	61.8 (3.2)	85.5 (4.9)	101.7 (8.0)	120 (8.9)
Comm.Cu_2O	5.1 (0.6)	11.2 (1.0)	19.5 (0.7)	28.4 (1.5)	38.8 (2.1)
Syn.Cu_2O	10.5 (0.3)	30.2 (2.3)	49.8 (3.2)	69.3 (4.0)	75.2 (3.7)

Unit: $mA \cdot cm^{-2}$

Table S2.5 Current density of CO data in H-cell, 0.5 M $KHCO_3$

Current density*	-1.2 V	-1.4 V	-1.6 V	-1.8 V	-2.0 V
Dendritic Cu	0.00	0.59	1.28	1.83	2.99
Comm.Cu_2O	0.20	0.86	1.67	3.54	5.39
Syn.Cu_2O	0.42	0.96	3.92	10.49	10.65

Unit: $mA \cdot cm^{-2}$

Table S2.6 Current density of formate data in H-cell, 0.5 M $KHCO_3$

Current density*	-1.2 V	-1.4 V	-1.6 V	-1.8 V	-2.0 V
Dendritic Cu	0.00	0.00	0.00	0.00	0.00
Comm.Cu_2O	0.00	0.00	0.10	0.25	0.44
Syn.Cu_2O	0.00	0.15	0.44	0.90	0.91

Unit: $mA \cdot cm^{-2}$

Table S2.7 Synthesized Cu_2O Faradaic efficiency data in H-cell, 1 M $KHCO_3$

Faradaic efficiency	-1.2 V	-1.4 V	-1.6 V	-1.8 V	-2.0 V
H_2	98.20% (0.05%)	97.51% (0.16%)	94.94% (0.39%)	89.20% (1.30%)	85.62% (1.36%)
CO	1.80% (0.05%)	1.97% (0.21%)	4.76% (0.40%)	9.83% (1.25%)	13.07% (1.32%)
HCOOH	0.00% (0.00%)	0.52% (0.09%)	0.30% (0.01%)	0.97% (0.09%)	1.31% (0.06%)

Table S2.8 Current density data of synthesized Cu_2O in H-cell, 1 M $KHCO_3$

Current density*	-1.2 V	-1.4 V	-1.6 V	-1.8 V	-2.0 V
Total	13.2 (0.3)	40.1 (1.1)	57.3 (1.1)	83.7 (4.3)	90.1 (5.5)
CO	0.24	0.79	2.73	8.23	11.78
Formate	0.00	0.21	0.17	0.81	1.18

Unit: $mA \cdot cm^{-2}$

2.2 Data of Electrochemical Evaluation in CP-cell

Table S2.9 Dendritic Cu Faradaic efficiency data in CP-cell, 0.5 M $KHCO_3$

Faradaic efficiency	-1.2 V	-1.4 V	-1.6 V	-1.8 V	-2.0 V
H_2	81.44% (1.65%)	79.20% (2.76%)	73.79% (0.44%)	71.63% (0.91%)	72.92% (1.86%)
CO	2.56% (0.51%)	2.64% (0.56%)	5.60% (0.36%)	8.16% (0.35%)	7.98% (0.35%)
HCOOH	16.00% (1.40%)	18.16% (2.31%)	20.61% (0.61%)	20.21% (0.68%)	19.10% (1.55%)

Table S2.10 Commercial Cu_2O Faradaic efficiency data in CP-cell, 0.5 M $KHCO_3$

Faradaic efficiency	-1.2 V	-1.4 V	-1.6 V	-1.8 V	-2.0 V
H_2	58.40% (2.61%)	52.16% (1.81%)	36.83% (1.38%)	32.65% (0.61%)	39.64% (1.39%)
CO	26.61% (1.06%)	34.46% (1.56%)	46.80% (1.74%)	48.27% (0.41%)	45.52% (0.90%)
HCOOH	14.99% (1.55%)	13.38% (0.48%)	16.37% (0.37%)	19.08% (0.29%)	14.84% (0.73%)

Table S2.11 Synthesized Cu_2O Faradaic efficiency data in CP-cell, 0.5 M $KHCO_3$

Faradaic efficiency	-1.2 V	-1.4 V	-1.6 V	-1.8 V	-2.0 V
H_2	59.26% (0.53%)	44.98% (1.52%)	42.23% (1.29%)	38.16% (1.69%)	36.96% (1.28%)
CO	35.08% (0.26%)	49.10% (1.20%)	50.89% (0.97%)	54.80% (1.48%)	55.42% (1.25%)
HCOOH	5.66% (0.28%)	5.92% (0.43%)	6.88% (0.65%)	7.04% (0.26%)	7.62% (0.37%)

Table S2.12 Total current density data in CP-cell, 0.5 M $KHCO_3$

Current density*	-1.2 V	-1.4 V	-1.6 V	-1.8 V	-2.0 V
Dendritic Cu	30.1 (1.2)	48.2 (2.4)	60.1 (2.2)	70.7 (3.5)	90.0 (4.6)
Comm.Cu_2O	9.9 (1.0)	17.5 (0.8)	30.5 (0.6)	53.6 (2.4)	61.3 (2.5)
Syn.Cu_2O	13.5 (0.3)	29.6 (0.7)	61.2 (1.3)	98.2 (2.4)	120.0 (3.3)

Unit: $mA \cdot cm^{-2}$

Table S2.13 Current density of CO data in CP-cell, 0.5 M $KHCO_3$

Current density*	-1.2 V	-1.4 V	-1.6 V	-1.8 V	-2.0 V
Dendritic Cu	0.77	1.27	3.37	5.77	7.18
Comm.Cu_2O	2.63	6.03	14.27	25.87	27.90
Syn.Cu_2O	4.74	14.53	31.14	53.81	66.50

Unit: $mA \cdot cm^{-2}$

Table S2.14 Current density of formate data in CP-cell, 0.5 M $KHCO_3$

Current density*	-1.2 V	-1.4 V	-1.6 V	-1.8 V	-2.0 V
Dendritic Cu	4.82	8.75	12.39	14.29	17.19
Comm.Cu_2O	1.48	2.34	4.99	10.23	9.10
Syn.Cu_2O	0.76	1.75	4.21	6.91	9.14

Unit: $mA \cdot cm^{-2}$

Table S2.15 Synthesized Cu_2O Faradaic efficiency data in CP-cell, 1 M $KHCO_3$

Faradaic efficiency	-1.2 V	-1.4 V	-1.6 V	-1.8 V	-2.0 V
H_2	53.51% (2.39%)	43.53% (1.00%)	37.78% (1.08%)	36.05% (0.16%)	30.82% (1.70%)
CO	41.07% (2.11%)	50.98% (0.70%)	55.80% (1.14%)	57.85% (0.38%)	61.31% (1.46%)
HCOOH	5.42% (0.29%)	5.49% (0.32%)	6.42% (0.07%)	6.10% (0.39%)	7.87% (0.33%)

Table S2.16 Current density data of synthesized Cu_2O in CP-cell, 1 M $KHCO_3$

Current density*	-1.2 V	-1.4 V	-1.6 V	-1.8 V	-2.0 V
Total	21.0 (0.8)	32.6 (1.1)	68.7 (1.2)	112.6 (1.9)	140.2 (7.2)
CO	8.62	16.62	38.33	65.14	85.96
Formate	1.14	1.79	4.41	6.87	11.03

Unit: $mA \cdot cm^{-2}$

Appendix 3 Supplementary Information of Cu_xO_y/Graphene in Chapter 4

*All potential presents in this chapter vs. Ag/AgCl

**Error in brackets, sample standard deviation

3.1 CA test in H-cell

Table S3.1 Current density data of Cu_xO_y/Graphene catalysts in H-cell, 1 M $KHCO_3$

Current density*	-1.2 V	-1.4 V	-1.6 V	-1.8 V	-2.0 V
n-Cu_xO_y/Graphene	0.4 (0.0)	1.5 (0.1)	6.0 (0.0)	12.1 (0.2)	23.4 (0.1)
b-Cu_xO_y/Graphene	1.2 (0.0)	4.8 (0.1)	13.7 (0.4)	24.8 (0.6)	45.5 (1.0)
m-Cu_xO_y/Graphene	1.0 (0.1)	2.3 (0.1)	8.0 (0.5)	13.7 (1.2)	28.3 (1.0)
f-Cu_xO_y/Graphene	1.2 (0.1)	4.3 (0.3)	15.0 (0.7)	26.1 (0.5)	51.7 (1.2)

Unit: $mA \cdot cm^{-2}$

3.2 CA test in CP-cell

Table S3.2 n-Cu_xO_y/Graphene Faradaic efficiency data in CP-cell, 0.5 M $KHCO_3$

Faradaic efficiency	-1.2 V	-1.4 V	-1.6 V	-1.8 V	-2.0 V
H_2	96.34% (0.09%)	90.92% (0.46%)	91.07% (0.48%)	90.57% (0.60%)	92.78% (0.44%)
CO	2.66% (0.14%)	8.27% (0.48%)	7.73% (0.52%)	8.53% (0.51%)	5.31% (0.41%)
HCOOH	1.00% (0.05%)	0.81% (0.04%)	1.20% (0.13%)	0.90% (0.10%)	1.91% (0.12%)

Table S3.3 b-Cu_xO_y/Graphene Faradaic efficiency data in CP-cell, 0.5 M $KHCO_3$

Faradaic efficiency	-1.2 V	-1.4 V	-1.6 V	-1.8 V	-2.0 V
H_2	95.65% (0.22%)	92.76% (0.23%)	89.57% (0.22%)	75.36% (0.52%)	84.55% (0.62%)
CO	3.35% (0.30%)	6.23% (0.18%)	9.09% (0.12%)	22.47% (0.36%)	14.18% (0.66%)
HCOOH	1.00% (0.12%)	1.01% (0.06%)	1.34% (0.10%)	2.17% (0.20%)	1.27% (0.04%)

Table S3.4 m-Cu_xO_y/Graphene Faradaic efficiency data in CP-cell, 0.5 M $KHCO_3$

Faradaic efficiency	-1.2 V	-1.4 V	-1.6 V	-1.8 V	-2.0 V
H_2	97.45% (0.10%)	89.55% (0.45%)	89.20% (0.83%)	90.45% (0.73%)	94.01% (0.48%)
CO	2.55% (0.10%)	8.96% (0.49%)	9.38% (0.90%)	8.45% (0.62%)	5.12% (0.53%)
HCOOH	0.00% (0.00%)	1.49% (0.05%)	1.42% (0.07%)	1.10% (0.14%)	0.87% (0.06%)

Table S3.5 f-Cu_xO_y/Graphene Faradaic efficiency data in CP-cell, 0.5 M $KHCO_3$

Faradaic efficiency	-1.2 V	-1.4 V	-1.6 V	-1.8 V	-2.0 V
H_2	92.64% (0.46%)	88.73% (0.16%)	81.92% (0.77%)	72.28% (0.95%)	87.11% (0.87%)
CO	5.43% (0.38%)	9.84% (0.30%)	15.26% (0.77%)	25.42% (0.56%)	10.94% (0.89%)
HCOOH	1.93% (0.25%)	1.43% (0.18%)	2.82% (0.16%)	2.30% (0.40%)	1.95% (0.17%)

Table S3.6 Total current density data of Cu_xO_y/Graphene in CP-cell, 0.5 M $KHCO_3$

Current density*	-1.2 V	-1.4 V	-1.6 V	-1.8 V	-2.0 V
n-Cu/G	4.9 (0.4)	6.8 (0.6)	11.6 (1.2)	23.1 (2.2)	31.5 (1.7)
b-Cu/G	10.1 (0.7)	16.6 (1.2)	27.9 (1.8)	39.1 (2.5)	70.3 (3.0)
m-Cu/G	8.1 (0.5)	10.5 (1.0)	16.5 (1.4)	36.6 (2.1)	46.9 (2.4)
f-Cu/G	10.0 (1.0)	18.3 (1.0)	26.8 (1.6)	48.0 (2.1)	85.1 (3.2)

Unit: $mA \cdot cm^{-2}$

Table S3.7 CO current density data of Cu_xO_y/Graphene in CP-cell, 0.5 M $KHCO_3$

Current density*	-1.2 V	-1.4 V	-1.6 V	-1.8 V	-2.0 V
n- Cu_xO_y/Graphene	0.13	0.56	0.90	1.97	1.67
b- Cu_xO_y/Graphene	0.34	1.03	2.54	8.79	9.97
m- Cu_xO_y/Graphene	0.21	0.94	1.55	3.09	2.40
f- Cu_xO_y/Graphene	0.54	1.80	4.09	12.20	9.31

Unit: $mA \cdot cm^{-2}$

Table S3.8 Formate current density data of Cu_xO_y/Graphene in CP-cell, 0.5 M $KHCO_3$

Current density*	-1.2 V	-1.4 V	-1.6 V	-1.8 V	-2.0 V
n- Cu_xO_y/Graphene	0.05	0.06	0.14	0.21	0.60
b- Cu_xO_y/Graphene	0.10	0.17	0.37	0.85	0.89
m- Cu_xO_y/Graphene	0.00	0.16	0.23	0.40	0.41
f- Cu_xO_y/Graphene	0.19	0.26	0.76	1.10	1.66

Unit: $mA \cdot cm^{-2}$

Appendix 4 Supplementary Information of Chapter 5

*All potential presents in this chapter vs. RHE

**Error in brackets, sample standard deviation

4.1 Experimental data of ATO

Table S4.1 ATO Faradaic efficiency data in H-cell, 0.5 M $KHCO_3$

Faradaic efficiency	-0.4 V	-0.6 V	-0.8 V	-1.0 V	-1.2 V
H_2	98.26% (0.07%)	95.59% (0.38%)	95.42% (0.45%)	95.16% (0.16%)	94.74% (0.21%)
CO	0.00% (0.00%)	1.90% (0.35%)	1.58% (0.28%)	2.03% (0.11%)	2.09% (0.08%)
HCOOH	1.74% (0.07%)	2.51% (0.28%)	3.00% (0.17%)	2.81% (0.07%)	3.17% (0.15%)

Table S4.2 ATO Faradaic efficiency data in CP-cell, 0.5 M $KHCO_3$

Faradaic efficiency	-0.4 V	-0.6 V	-0.8 V	-1.0 V	-1.2 V
H_2	62.69% (0.61%)	46.24% (1.45%)	43.33% (1.98%)	38.55% (1.09%)	34.78% (1.27%)
CO	2.21% (0.20%)	5.77% (0.19%)	5.56% (0.21%)	8.47% (0.39%)	8.46% (0.30%)
HCOOH	35.10% (0.63%)	47.99% (1.29%)	51.11% (1.81%)	52.98% (0.83%)	56.76% (1.14%)

Table S4.3 Total current density data of ATO in H-cell and CP-cell, 0.5 M $KHCO_3$

Current density*	-0.4 V	-0.6 V	-0.8 V	-1.0 V	-1.2 V
H-cell	35.6 (1.7)	65.5 (2.9)	128.6 (2.5)	163.2 (10.2)	199.9 (13.0)
CP-cell	20.2 (0.4)	35.1 (0.4)	42.1 (0.6)	65.6 (2.1)	90.1 (2.0)

Unit: $mA \cdot cm^{-2}$

Table S4.4 Formate current density data of ATO in H-cell and CP-cell, 0.5 M $KHCO_3$

Current density*	-0.4 V	-0.6 V	-0.8 V	-1.0 V	-1.2 V
H-cell	0.9	5.4	9.9	13.9	10.6
CP-cell	7.1	16.8	21.5	34.8	51.1

Unit: $mA \cdot cm^{-2}$

4.2 Experimental data of ITO

Table S4.5 ITO Faradaic efficiency data (Formate) in 1 M $KHCO_3$ and 1 M KOH electrolytes

Faradaic efficiency	-0.4 V	-0.6 V	-0.8 V	-1.0 V	-1.2 V
1 M $KHCO_3$	9.53% (0.05%)	57.32% (0.31%)	64.54% (0.46%)	56.02% (1.04%)	67.54% (0.89%)
1 M KOH	18.70% (0.35%)	57.77% (0.21%)	63.74% (0.66%)	67.26% (0.98%)	74.24% (1.64%)

Table S4.6 Total current density data (Formate) of ITO in 1 M $KHCO_3$ and 1 M KOH electrolytes

Current density*	-0.4 V	-0.6 V	-0.8 V	-1.0 V	-1.2 V
1 M $KHCO_3$	2.8 (0.1)	8.5 (0.8)	20.7 (1.0)	38.8 (1.8)	49.8 (2.6)
1 M KOH	10.4 (0.1)	23.3 (0.2)	49.5 (1.1)	53.9 (1.0)	91.6 (2.4)

Unit: $mA \cdot cm^{-2}$

Table S4.7 Formate current density data of ITO in 1 M $KHCO_3$ and 1 M KOH electrolytes

Current density*	-0.4 V	-0.6 V	-0.8 V	-1.0 V	-1.2 V
1 M $KHCO_3$	0.26	4.85	13.33	21.72	33.64
1 M KOH	1.94	13.46	31.58	36.27	68.04

Unit: $mA \cdot cm^{-2}$

4.3 Experimental data of In-MOF

Table S4.8 In-MOF Faradaic efficiency data in CP-cell

Faradaic efficiency	-0.4 V	-0.6 V	-0.8 V	-1.0 V	-1.2 V
0.1 M $KHCO_3$	13.17% (0.05%)	17.65% (0.10%)	31.55% (0.14%)	41.41% (0.12%)	44.90% (0.20%)
0.5 M $KHCO_3$	20.64% (0.13%)	57.57% (0.23%)	50.81% (0.21%)	64.84% (0.24%)	53.99% (0.31%)
1 M $KHCO_3$	20.48% (0.09%)	58.51% (0.45%)	60.67% (0.63%)	81.45% (1.09%)	72.46% (1.34%)
2 M $KHCO_3$	39.08% (0.42%)	61.77% (0.78%)	64.97% (1.15%)	58.07% (1.01%)	63.59% (1.84%)
0.1 M KOH	11.07% (0.83%)	14.35% (1.02%)	28.57% (1.10%)	38.67% (1.36%)	36.02% (1.32%)

Table S4.9 In-MOF total current density data in CP-cell

Current density*	-0.4 V	-0.6 V	-0.8 V	-1.0 V	-1.2 V
0.1 M $KHCO_3$	4.6 (0.1)	4.6 (0.1)	8.9 (0.2)	13.5 (0.3)	16.0 (0.2)
0.5 M $KHCO_3$	3.1 (0.1)	13.0 (0.2)	27.1 (0.2)	48.9 (0.5)	62.0 (0.8)
1 M $KHCO_3$	4.2 (0.1)	6.8 (0.4)	35.0 (0.7)	54.2 (1.4)	140.4 (2.6)
2 M $KHCO_3$	6.6 (0.5)	17.9 (0.8)	38.8 (1.0)	82.9 (1.1)	157.0 (2.5)
0.1 M KOH	2.3 (0.2)	4.1 (0.3)	6.0 (1.0)	10.7 (1.2)	16.0 (1.6)

Unit: $mA \cdot cm^{-2}$

Table S4.10 In-MOF current density of formate data in CP-cell

Current density*	-0.4 V	-0.6 V	-0.8 V	-1.0 V	-1.2 V
0.1 M $KHCO_3$	0.6	0.8	2.8	5.6	7.2
0.5 M $KHCO_3$	0.6	7.5	13.8	31.7	33.5
1 M $KHCO_3$	0.9	4.0	21.2	44.1	101.7
2 M $KHCO_3$	2.6	11.1	25.2	48.1	99.8
0.1 M KOH	0.3	0.6	1.7	4.1	5.8

Unit: $mA \cdot cm^{-2}$

Table S4.11 In-MOF durability test data in CP-cell

Time	0-1 h	1-2 h	2-3 h	3-4 h
FE	82.41% (1.07%)	83.02% (1.18%)	79.40% (2.29%)	76.76% (2.91%)
Total Current density	53.1 (1.5)	57.0 (1.4)	58.1 (2.1)	60.1 (2.3)
Current density of formate	43.7	47.4	46.6	46.1

Unit: $mA \cdot cm^{-2}$

Appendix 5 Supplementary Information of Chapter 7

5.1 COMSOL Simulation Parameters

Table S5.1 Physical model parameters

Model	Value	Unit
CP width	18	mm
CP height	21	mm
CP depth	0.25	mm
GA width	18	mm
GA height	21	mm
GA depth	4	mm
Gas input radius	3	mm
Gas output radius	3	mm

Table S5.2 Parameter for physical properties, second current density and transfer of concentration spices

Simulation calculation parameters	**Value**	**Unit**
electrolyte conductivity	1	S/M
CP conductivity	125	S/M
GA conductivity	153	S/M
CP porosity	0.3	
GA porosity	0.8	
T	293.15	K
$E_{eq,ref}(T)$	0.197	V
C_R	0.005	
C_O	1	
$i_{0,ref}(T)$	0.005	A/M^2
α_a	0.5	
α_v	$1e^6$	1/m
electrolyte potential	-0.18	V
electric potential	0	V
PA	1	Pa
$M_{\omega CO2}$	0.044	kg/mol
$M_{\omega HCOOH}$	0.046	kg/mol
u	10	m/s

diffusivity	$1e-5$	m^2/s

$E_{eq,ref}(T)$ is reference equilibrium potential, C_R is reduced species expression, C_O is oxidised species expression, $i_{0,ref}(T)$ is reference exchange current density, $M_{\omega CO2}$ is CO_2 molar mass, $M_{\omega HCOOH}$ is HCOOH molar mass, u is gas inlet velocity. All physical modelling parameters are presented in Table S5.1. Secondary Current Distribution (SCD) module was used to calculate overpotential change, and molality was simulated by Transfer of Concentrated Species (TOCS) module. Parameters in Table S5.2 are used to calculate the simulation model. Diffusivity is a function of gas composition, in the simulation, CO_2 and products follow Maxwell-Stefan diffusion. The value used is a default value from COMSOL.

The potential change is calculated based on Nernst equation

$$E_{eq} = E_{eq,ref}(T) - \frac{RT}{nF} ln \frac{C_R}{C_O}$$

At the same time, the Butler-Volmer dynamic expression was used to express the local current distribution, and this expression was also calculated based on The Nernst equation

$$i_{loc} = i_0(\exp\left(\frac{\alpha_a F \eta}{RT}\right) - \exp\left(\frac{-\alpha_c F \eta}{RT}\right))$$

$$= i_{0,ref}(T)(C_R \exp\left(\frac{\alpha_a F \eta_{ref}}{RT}\right) - \exp\left(\frac{-\alpha_c F \eta_{ref}}{RT}\right)$$

Where $i_0 = i_{0,ref}(T) C_R^{\frac{\alpha_c}{n}} C_O^{\frac{\alpha_a}{n}}$, $\alpha_c = n - \alpha_a$ and $\eta_{ref} = E_{ct} - E_{eq,ref}(T)$

The distribution of the amount of matter in the porous electrode under the influence of the Nester Equation follows the following function

$$R_j = \frac{v_j i_v}{nF}$$

Where v_j is stoichiometric coefficient and i_v is coupled reaction from the porous electrode reaction in the previous step.

5.2 Experimental data

*All potential presents in this section vs. RHE

Experimental data of eCO_2RR by using Cu_2O as catalyst:

(Error in brackets, sample standard deviation)

Table S5.3 Cu_2O Faradaic efficiency in CP-cell

Faradaic efficiency	-0.4 V	-0.6 V	-0.8 V	-1.0 V	-1.2 V
H_2	41.92% (1.57%)	31.47% (1.50%)	37.38% (2.14%)	34.23% (3.68%)	38.88% (0.20%)
CO	55.13% (1.63%)	65.71% (1.54%)	60.19% (2.72%)	64.23% (3.33%)	58.93% (0.22%)
HCOOH	2.95% (0.40%)	2.83% (0.31%)	2.42% (0.74%)	1.54% (0.50%)	2.19% (0.27%)

Table S5.4 Cu_2O Faradaic efficiency in GA-cell

Faradaic efficiency	-0.4 V	-0.6 V	-0.8 V	-1.0 V	-1.2 V
H_2	70.03% (2.12%)	87.65% (1.49%)	86.04% (1.70%)	89.97% (1.96%)	95.56% (1.11%)
CO	29.67% (2.12%)	12.34% (1.49%)	13.62% (1.85%)	9.86% (1.96%)	4.17% (1.10%)
HCOOH	0.00% (0.00%)	0.01% (0.00%)	0.34% (0.20%)	0.17% (0.05%)	0.27% (0.04%)

Table S5.5 Cu_2O Faradaic efficiency in GACP-cell

Faradaic efficiency	-0.4 V	-0.6 V	-0.8 V	-1.0 V	-1.2 V
H_2	11.95% (1.64%)	9.86% (0.77%)	5.99% (0.26%)	5.11% (0.38%)	7.36% (0.29%)
CO	79.58% (2.13%)	80.41% (1.07%)	84.20% (0.33%)	83.54% (0.47%)	81.91% (1.10%)
HCOOH	8.47% (0.50%)	9.73% (0.39%)	9.81% (0.53%)	11.35% (0.14%)	10.73% (1.11%)

Table S5.6 Cu_2O Faradaic efficiency data in H-cell

Faradaic efficiency	-0.4 V	-0.6 V	-0.8 V	-1.0 V	-1.2 V
H_2	98.58% (0.69%)	87.07% (0.90%)	83.83% (0.53%)	84.57% (1.55%)	86.50% (2.43%)
CO	0.00% (0.00%)	11.45% (0.91%)	14.76% (0.71%)	14.33% (1.34%)	12.63% (2.46%)
HCOOH	1.42% (0.69%)	1.49% (0.02%)	1.42% (0.20%)	1.10% (0.22%)	0.87% (0.08%)

Table S5.7 Total current density of Cu_2O based eCO_2RR

Current density*	-0.4 V	-0.6 V	-0.8 V	-1.0 V	-1.2 V
H-cell	34.5 (2.5)	55 (7.0)	92.5 (4.5)	150 (8.0)	210 (7.5)
CP-cell	17.5 (2.0)	44 (3.5)	58.5 (4.0)	123 (5.5)	142.5 (2.5)
GA-cell	19 (3.0)	52 (4.5)	82.5 (2.5)	125 (6.0)	170 (10.5)
GACP-cell	37.5 (1.5)	65.5 (2.0)	99 (3.0)	125 (2.5)	151 (1.5)

Unit: $mA \cdot cm^{-2}$

Table S5.8 CO current density of Cu_2O based eCO_2RR

Current density*	-0.4 V	-0.6 V	-0.8 V	-1.0 V	-1.2 V
H-cell	0.0	6.3	13.6	21.5	26.5
CP-cell	9.6	28.9	35.2	79.0	84.0
GA-cell	5.7	6.4	11.2	12.3	7.1
GACP-cell	29.8	52.7	83.4	104.4	123.7

Unit: $mA \cdot cm^{-2}$

Table S5.9 Faradaic efficiency of durability test using CP-cell and GACP-cell

Faradaic efficiency	CP-cell 4 h	CP-cell 8 h	GACP-cell 4 h	GACP-cell 8 h
H_2	34.92% (2.60%)	75.53% (2.73%)	5.74% (0.80%)	12.50% (1.69%)
CO	63.28% (2.94%)	22.93% (2.57%)	83.36% (1.66%)	79.27% (2.02%)
HCOOH	1.80% (0.40%)	1.54% (0.15%)	10.90% (0.86%)	8.23% (0.34%)

Experimental data of eCO_2RR by using ATO:

(Error in brackets, sample standard deviation)

Table S5.10 ATO Faradaic efficiency in H-cell

Faradaic efficiency	-0.4 V	-0.6 V	-0.8 V	-1.0 V	-1.2V
H_2	98.44% (0.09%)	97.65% (0.12%)	97.36% (0.15%)	96.59% (0.25%)	96.45% (0.26%)
CO	0.53% (0.05%)	1.02% (0.07%)	0.76% (0.06%)	1.25% (0.11%)	1.05% (0.02%)
HCOOH	1.03% (0.04%)	1.33% (0.13%)	1.88% (0.13%)	2.16% (0.13%)	2.50% (0.26%)

Table S5.11 ATO Faradaic efficiency in CP-cell

Faradaic efficiency	-0.4 V	-0.6 V	-0.8 V	-1.0 V	-1.2 V
H_2	46.47% (1.80%)	32.86% (0.99%)	33.76% (0.31%)	28.88% (1.85%)	41.85% (0.85%)
CO	7.55% (0.52%)	13.48% (0.47%)	10.33% (0.59%)	11.41% (1.56%)	8.79% (0.71%)
HCOOH	45.98% (1.42%)	53.66% (0.56%)	55.91% (0.47%)	59.71% (0.62%)	49.36% (0.62%)

Table S5.12 ATO Faradaic efficiency in GA-cell

Faradaic efficiency	-0.4 V	-0.6 V	-0.8 V	-1.0 V	-1.2 V
H_2	80.04% (0.61%)	73.18% (1.45%)	65.92% (1.60%)	68.86% (1.95%)	68.71% (1.30%)
CO	1.42% (0.11%)	2.21% (0.25%)	4.28% (0.40%)	5.35% (0.30%)	4.64% (0.65%)
HCOOH	18.54% (0.52%)	24.61% (1.34%)	29.80% (1.20%)	25.79% (1.65%)	26.65% (1.51%)

Table S5.13 ATO Faradaic efficiency in GACP-cell

Faradaic efficiency	-0.4 V	-0.6 V	-0.8 V	-1.0 V	-1.2 V
H_2	23.38% (1.52%)	12.99% (1.51%)	9.68% (0.55%)	5.59% (0.29%)	5.95% (0.44%)
CO	6.52% (0.29%)	10.10% (1.25%)	12.21% (0.71%)	11.43% (0.70%)	9.51% (1.49%)
HCOOH	70.10% (1.35%)	76.91% (0.55%)	78.11% (1.17%)	82.98% (0.47%)	84.54% (1.37%)

Table S5.14 Total current density of ATO based eCO_2RR

Current density*	-0.4 V	-0.6 V	-0.8 V	-1.0 V	-1.2 V
H-cell	32 (2.0)	125.5 (6.0)	200 (9.0)	235 (13.5)	315 (15.0)
CP-cell	15 (2.0)	33.5 (2.0)	55 (3.5)	80.5 (4.5)	102.5 (2.5)
GA-cell	17 (1.0)	42.5 (1.0)	71 (2.0)	94 (2.0)	105 (4.0)
GACP-cell	22.5 (1.5)	35 (0.5)	64 (2.0)	96 (3.0)	115 (3.0)

Unit: $mA \cdot cm^{-2}$

Table S5.15 Formic current density of ATO based eCO_2RR

Current density*	-0.4 V	-0.6 V	-0.8 V	-1.0 V	-1.2 V
H-cell	0.3	1.7	3.8	5.1	7.9
CP-cell	6.9	18.0	30.8	48.1	50.6
GA-cell	3.2	10.5	21.2	24.2	28.0
GACP-cell	15.8	26.9	50.0	79.7	97.2

Unit: $mA \cdot cm^{-2}$